CGE

Centre of Geodetic Earth System Research

GOCE geoid, mean dynamic ocean topography and geostrophic velocities

Alberta Albertella and Reiner Rummel

CGE Report 6
2014

Imprint

Centre of Geodetic Earth System Research (CGE), a collaboration between

Institute of Astronomical and Physical Geodesy (IAPG)
Technische Universität München
Arcisstraße 21, D-80333 München

Research Facility Satellite Geodesy (FESG)
Technische Universität München
Arcisstraße 21, D-80333 München

Commission for Geodesy and Glaciology (KEG), Geodesy Section
Bavarian Academy of Sciences and Humanities
Alfons-Goppel-Str. 11, D-80539 München

German Geodetic Research Institute (DGFI)
Alfons-Goppel-Str. 11, D-80539 München

This work is published as Number 6 in the *CGE Reports* series. An electronic version is available from http://www.cge-munich.de.

Impressum

Centrum für Geodätische Erdsystemforschung (CGE), eine Kooperation zwischen

Institut für Astronomische und Physikalische Geodäsie (IAPG)
Technische Universität München
Arcisstraße 21, D-80333 München

Forschungseinrichtung Satellitengeodäsie (FESG)
Technische Universität München
Arcisstraße 21, D-80333 München

Kommission für Erdmessung und Glaziologie (KEG), Abteilung Erdmessung
Bayerische Akademie der Wissenschaften
Alfons-Goppel-Str. 11, D-80539 München

Deutsches Geodätisches Forschungsinstitut (DGFI)
Alfons-Goppel-Str. 11, D-80539 München

Diese Arbeit wird als Nummer 6 der Schriftenreihe „CGE Reports“ veröffentlicht. Eine elektronische Version ist unter http://www.cge-munich.de erhältlich.

E-mail: info@cge-munich.de
Homepage: http://www.cge-munich.de

München, 2014

ISSN 2195-7126
ISBN 978-3-934205-37-6

Centre of Geodetic Earth System Research

GOCE geoid, mean dynamic ocean topography and geostrophic velocities

IAPG contribution to GEOTOP project

Alberta Albertella and Reiner Rummel

CGE Report 6
2014

Contents

Acknowledgements

We thank our project partners Jens Schröter (Alfred-Wegener Institut für Polar und Meeresforschung, Bremerhaven), Tjiana Janjić (Alfred-Wegener Institut für Polar und Meeresforschung, Bremerhaven, now: Meteorologisches Institut, LMU München), Wolfgang Bosch (Deutsches Geodätisches Forschungsinstitut, München) and Roman Savcenko (former scientist Deutsches Geodätisches Forschungsinstitut, München) for valuable discussions. Special thanks go to Christian Gerlach (Bayerische Akademie der Wissenschaften, München) and Weiyong Yi (Institut für Astronomische und Physikalische Geodäsie, Technische Universität München) for their great contribution to the material developed in this manuscript.

Furthermore we wish to thank Ole Baltazar Andersen (National Space Institute, Technical University of Denmark) for providing us the mean sea surface DTU10, Frank Siegismund (Institute of Oceanography, Universität Hamburg) for providing a corrected dataset of the drifter measurements and Dmitry Sidorenko (Alfred-Wegener Institut für Polar und Meeresforschung, Bremerhaven) for his contribution to the software for comparing the drifter observations and the geodetic geostrophic velocities.

This work has been funded under DFG Priority Research Programme SPP 1257 “Mass Transport and Mass Distribution in the Earth System”. The data and the products described in the paper can be requested from the authors.

Chapter 1

Introduction

GEOTOP is one of the projects of the Priority Research Program SPP 1257 "Mass Transport and Mass Distribution in the Earth System" of the German Research Foundation (DFG). Its detailed title is Sea Surface Topography and Mass Transport of the Antarctic Circumpolar Current. It has been supported by DFG in its three phases, each lasting two years.
Project partners are:

- Institut für Astronomische und Physikalische Geodäsie (IAPG) - Technische Universität München,
- Deutsches Geodätisches Forschungsinstitut (DGFI) - München,
- Alfred-Wegener-Institut für Polar und Meeresforschung (AWI) - Bremerhaven,
- Institut für Planetare Geodäsie (IPG-TUD) - Technische Universität Dresden.

The general objective of GEOTOP is the determination of the absolute, temporally changing ocean circulation flow field and its mass and heat transport by assimilating geodetic estimates of the dynamic sea surface topography (SST) and oceanographic in-situ data. Focus area is the Atlantic section of the Antarctic Circumpolar Current (ACC) including the Weddell Gyre, one of the tipping points of the global climate system. Challenges are the inclusion of GOCE data, extended altimetry, spectral consistency of altimetry and geoid model, rigorous error propagation and estimation and the treatment of sea ice covered ocean areas.
The results of the satellite gravity gradiometry mission GOCE (in combination with the results from GRACE) lead to much more accurate and detailed models of the geoid and gravity anomaly field. These results can now be combined with re-processed models of the mean sea surface based on almost twenty years of satellite radar altimetry.

The most important experiences of the past two years of GEOTOP are as follows:

- The combination and consistent filtering of geodetic data in particular in coastal regions is difficult: the geoid is represented in global spherical harmonics, while altimetry data are given along profiles.

- There exist significant discrepancies between satellite based geoid models and geoid models based on surface data in the area of the ACC.
- Ocean altimetry in the Antarctic Ocean is limited to the sea-ice free seasons. This causes problems in the determination of mean dynamic ocean topography (MDT) and of time series of the ocean surface.
- Geodetic MDT could be successfully assimilated into the ocean model employing the Kalman Filtering approach. Exceptions are the Weddell Sea area and coastal areas.

Problems remain in the representation of deep ocean temperature and salinity, which may require assimilation of temperature and salinity data. Finally, only now high resolution GOCE geoid models become available.

In the present report we document the details of our processing for the purpose of later use or re-assessment. The report does not cover the complete work performed in the context of GEOTOP. It is confined to the geodetic MDT and geostrophic velocities and therefore essentially to the work packages of IAPG.

Chapter 2

Progress in gravity field determination

2.1 New GOCE and GOCE-GRACE geoid

After a considerable delay, the GOCE satellite was successfully launched on March 17, 2009. It is the first mission of the Living Planet programme of ESA, (European Space Agency, 1999). The acronym stands for Gravity and steady-state Ocean Circulation Explorer. This already indicates the high relevance of this mission for oceanography.

The objectives of the mission are the determination of the geoid accurate to 1 to 2 cm and of gravity anomalies with an accuracy of 1 mGal. Thereby the spatial resolution should be about 100 km half-wavelength corresponding to a spherical harmonic expansion complete up to degree and order 200 (d/o = 200). These goals are based on a set of science objectives. The most important one is the determination of global dynamic ocean topography with the same accuracy and spatial resolution for the purpose of ocean circulation and ocean mass and heat transport studies.

The core instrument of GOCE is a three axis gravitational gradiometer based on the principle of differential accelerometry, compare e.g. Rummel & Gruber (2010) or Rummel *et al.* (2011). It is for the first time that an instrument of this kind is flown on-board of a satellite. The long wavelength part of the gravitational field is derived from the orbit, i.e. from orbit tracking by GPS. The satellite is orbiting at an altitude of only 260 km and it is kept drag-free in along track direction. All sensors of GOCE are performing according to their specifications (with a slight degradation of the vertical gradiometer component, which cannot yet be explained). In summer 2012 about twelve months of mission data have been processed and a series of spherical harmonic models has been constructed.

In parallel a reprocessing of all mission data, acquired so far takes place. Its main elements are a joint processing of all three star trackers, improved attitude and angular rate reconstruction and linear interpolation of calibration parameters in between calibration, see Stummer *et al.* (2012). The reprocessing leads to an improved determination of spherical harmonic coefficients, in particular at low degrees and orders. First gravity models based on the reprocessed data have been released in spring 2013.

In this study we consider three satellite gravity models:

1. the GOCE-only satellite model TUMGOCE (Yi, 2012),
2. the GRACE-only satellite model ITG2010 (Mayer-Gürr *et al.*, 2010b),
3. the GRACE-GOCE satellite model GOCO2s[1] (Pail *et al.*, 2010).

The satellite gravity model TUMGOCE is a GOCE-only solution based on measurements from November 2009 to April 2011 of GOCE orbits and gravity gradients V_{xx}, V_{yy}, V_{zz} and V_{xz}. It uses kinematic orbits and the integral equation approach for the determination of the spherical harmonic coefficients up to d/o 150. The gravity gradients in the Gradiometer Reference Frame are band pass filtered between 5 and 100 mHz employing an infinite impulse response filter. In the polar areas, where no GOCE data are available, geoid heights from EGM2008 up to d/o 200 on a $1^\circ \times 1^\circ$ grid with an assumed std. dev. of 20 cm are introduced for stabilization, see Yi (2012). The model is available up to degree/order 224.

The joint US/German Gravity Recovery And Climate Experiment (GRACE) mission uses low-low satellite-to-satellite (SST) tracking by a precise, dual-frequency microwave ranging system. In the low to middle part of the wavelength spectrum the low-low SST concept of GRACE determines the gravity field better than GOCE. The model ITG-Grace2010s (ITG2010 in the following) (Mayer-Gürr *et al.*, 2010a) is a long-term mean gravity field model covering the time span 2002-08 to 2009-08 calculated from GRACE data up to degree and order 180.

The gravity model GOCO2s (Goiginger *et al.*, 2011; Pail *et al.*, 2010) combines the information from the mission GOCE with the normal equations of GRACE model ITG2010. In particular it uses:

- 7 years of GRACE data,
- 12 months of GOCE satellite-to-satellite tracking (SST) data,
- 8 months of GOCE satellite gravity gradiometry (SGG) data,
- 8 years of CHAMP and
- 5 years of SLR observation.

The model is complete up to degree and order 250.

In the low-to-middle part of the spectrum the low-low SST concept of GRACE is superior to GOCE; GOCE starts to become superior at degree 120. In Fig. 2.1 the error degree variances of TUMGOCE, ITG2010 and GOCO2s are shown compared with the signal power density (dotted line). In the combined model the GRACE information is dominant up to degree and order 70, while the GOCE data starts to prevail at degree and order 120.

In Fig. 2.2 the cumulative geoid errors for the three gravity models are shown as function of the maximum spherical harmonic degree, see also Table 2.1.

---

[1] Only in the chapter 7 the gravity model GOCO03s has been considered (Mayer-Gürr *et al.*, 2012), using its variance-covariance matrices.

L_{max}	**GRACE**	**GOCO**	**GOCE**
140	1.3	0.7	1.1
160	4.8	1.5	1.6
180	18.7	3.1	2.6
200	–	5.5	4.5
220	–	9.7	8.0
240	–	14.5	–

Table 2.1: Cumulative formal geoid errors for ITG2010, GOCO2s and TUMGOCE gravity models. Units are centimeters.

The geoid height N can be expressed in a point $P = (\vartheta_P, \lambda_P)$ as a series of spherical harmonics:

$$N(\vartheta_P, \lambda_P) = R \sum_{\ell=2}^{L} \sum_{m=0}^{\ell} \left(\bar{C}_{\ell m} \cos m\lambda_P + \bar{S}_{\ell m} \sin m\lambda_P\right) \bar{P}_{\ell m} \cos(\vartheta_P) \tag{2.1}$$

where $\bar{P}_{\ell m} \cos(\vartheta_P)$ are fully normalized associated Legendre functions of degree ℓ and order m; $\bar{C}_{\ell m}, \bar{S}_{\ell m}$ are the dimensionless normalized potential coefficients; L is the maximum degree of the expansion.

The geoid undulations in the region of the Antarctic Circumpolar Current (ACC) $(-90° < \varphi < -30°, 0° < \lambda < -360°)$ have variations of 110 m, Fig. 2.3. The minimum ($\cong -60$ m) is in the region of the Ross Sea. The maximum ($\cong 40$ m) is in the ocean south of the African continent $(30° < \lambda < 60°)$.

In Table 2.2 the RMS of the global and local differences between different geoid models are shown. In the ACC area, the differences between the geoid TUMGOCE and the ITG2010 reach even 2 m, see right panel of Fig. 2.4. In all cases the differences are larger close to the South Pole. This is probably due to the missing GOCE data above latitude 83.3° and the regularization applied there to the GOCE models.

	global	**local**
TUMGOCE - GOCO2s (up d/o 160)	6.46	8.95
TUMGOCE - GOCO2s (up d/o 180)	9.37	12.37
TUMGOCE - GOCO2s (up d/o 200)	17.48	23.31
TUMGOCE - ITG2010 (up d/o 180)	25.02	30.01
GOCO2s - ITG2010 (up d/o 180)	23.33	27.03

Table 2.2: RMS of the global and local differences between different geoids. The local statistics are evaluated in the region of the ACC $(-90° < \varphi < -30°, 0° < \lambda < -360°)$. Units are centimeters.

2.2 Error analysis

The gravity models (TUMGOCE, GOCO2s and ITG2010) are available together with their full error variance covariance matrix, see (Mayer-Gürr *et al.*, 2010a; Yi, 2012; Pail *et al.*, 2011). This means that we are able to perform the full error propagation from the spherical harmonic coefficients to the geoid undulation, deriving not only the formal error in each point on earth, but also all the covariances.

In first approximation we do not consider the correlations between the harmonic coefficients, but only their variances. In this case the error in the geoid heights does not depend on the longitude, as it is shown in Fig. 2.5. In Fig. 2.6 the geoid errors up d/o 180 of the three gravity models in the ACC are shown. In the first and second case the errors close to the South Pole increase because they are dominated by the effect of the polar gap. The inclination of the orbit of the GRACE satellites is $I \approx 89°$, while for GOCE it is $I = 96.70°$. For ITG2010 the cumulative geoid error up d/o 180 is 24 cm, for TUMGOCE it is 5 cm and for GOCO2s it is 2.4 cm.

Considering the full variance-covariance matrix, the full error propagation is possible.

In the following we consider the gravity model GOCO2s up to degree and order 250. The covariance propagation was computed for a test area: $-50° < \varphi < -70°$ in latitude and $-30° < \lambda < -10°$ in longitude, with an equi-angular spacing of 0.25°.

In Fig. 2.7 the covariances for the point ($\varphi = -60°, \lambda = -20°$) are shown. The variance (value in the point: $\varphi = -60°, \lambda = -20°$) is 0.027 m^2, which corresponds to a std. dev. error of 16.36 cm. As we can see in the Fig. 2.8 and Fig. 2.9, the covariances are almost isotropic.

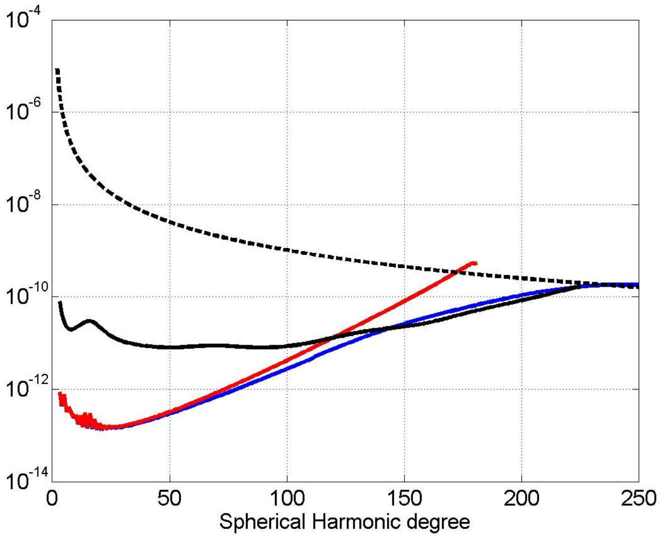

Figure 2.1: RMS of the errors per degree for the geopotential models TUMGOCE (black line), GOCO2s (blue line) and ITG2010 (red line). The signal RMS per degree is shown as dotted line.

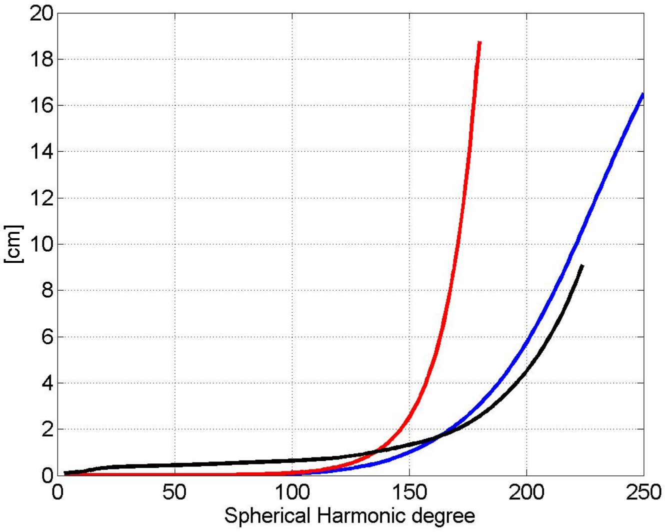

Figure 2.2: Cumulative geoid height error as function of the spherical harmonic degree. GOCO2s (blue), TUMGOCE (black line) and ITG2010 (red line). Units are centimeters.

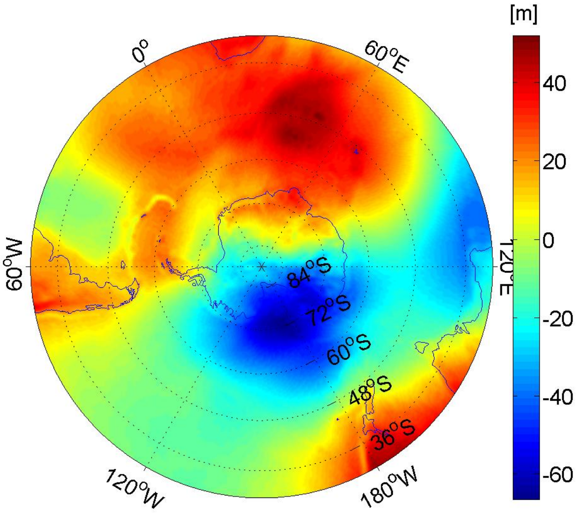

Figure 2.3: Values of the geoid undulations from TUMGOCE gravity model up d/o 224 in the region of the ACC current. The grid is $30' \times 30'$.

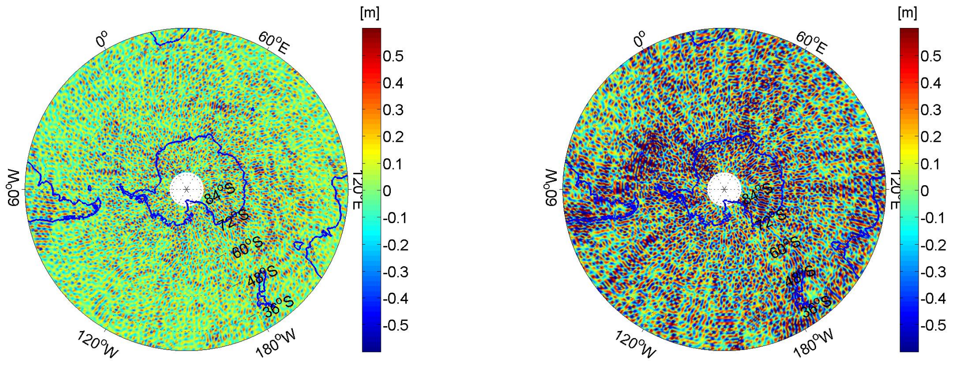

Figure 2.4: Differences between geoid from TUMGOCE and geoid from GOCO2s (left panel) and geoid from ITG2010 (right panel).

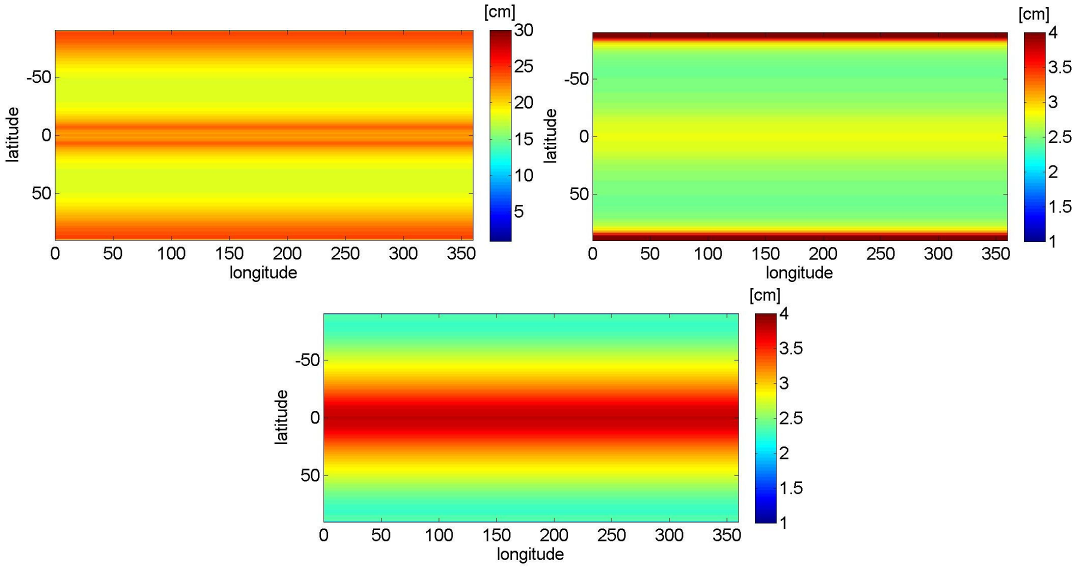

Figure 2.5: Geographical distribution of the cumulative (up d/o 180) geoid errors for different gravity models. Upper left = ITG2010, upper right = TUMGOCE, lower panel = GOCO2s.

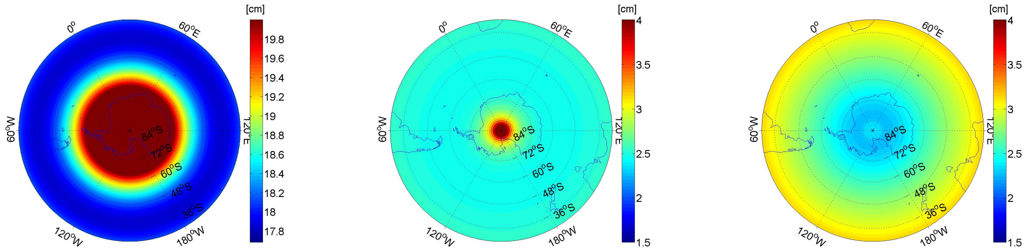

Figure 2.6: Cumulative (up d/o 180) geoid error in the ACC area. Left panel = ITG2010, middle panel = TUMGOCE, right panel = GOCO2s.

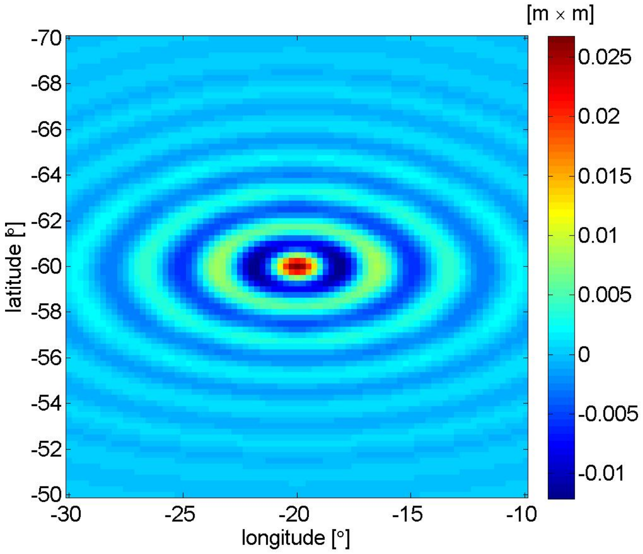

Figure 2.7: Covariance of the geoid heights at the point ($\varphi = -60°, \lambda = -20°$). Gravity model GOCO2s up to degree and order 250 is considered. Units are m^2

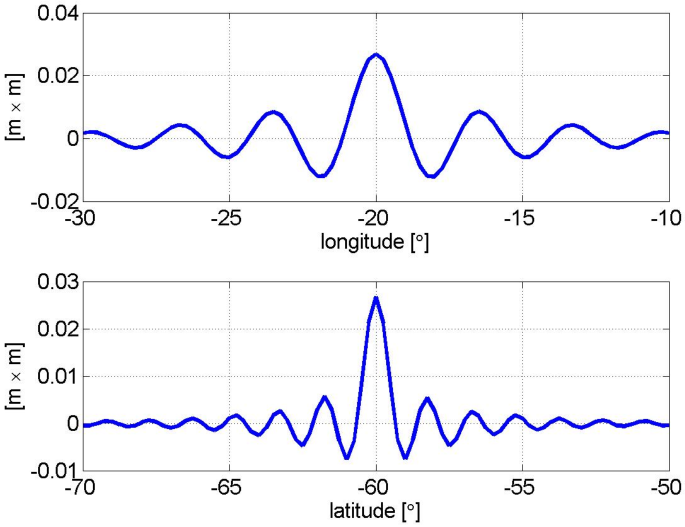

Figure 2.8: Covariance of the geoid heights at the point ($\varphi = -60°, \lambda = -20°$) as function of longitude (upper panel) and of latitude (lower panel). Gravity model GOCO2s up to degree and order 250 is considered. Units are m^2.

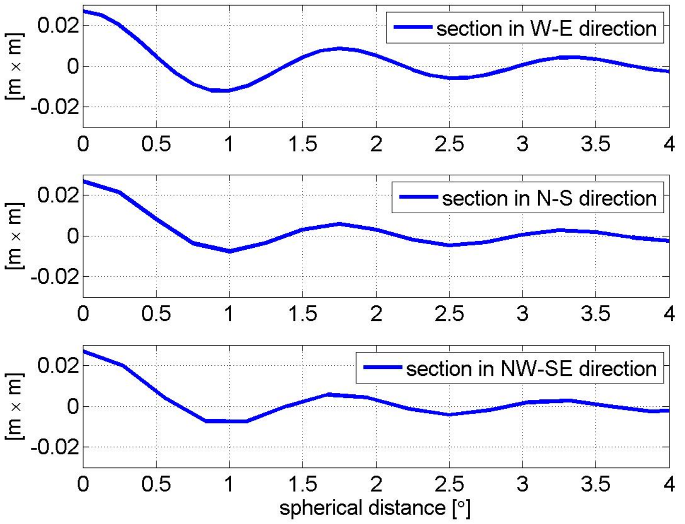

Figure 2.9: Sections of the covariance of the geoid heights at the point ($\varphi = -60°, \lambda = -20°$) as function of the spherical distance. Gravity model GOCO2s up to degree and order 250 is considered. Units are m^2.

Chapter 3

Altimetric Mean Sea Surface (MSS)

Altimeter satellites provide precise, repeated, and quasi-global measurements of sea surface heights. A MSS is a temporal average of these sea surface heights over a chosen period of time. As the present investigation aims at the determination of a quasi-stationary MDT, the MSS should represent a reliable long-term mean.

In this study two mean sea surfaces models are considered: the DGFI10 and the DTU10.

The MSS DGFI10 has been generated, averaging the measurements of altimeter missions with exact repeat periods (ERS- 1/2, ENVISAT, TOPEX/Poseidon, Jason-1 and Jason-2), acquired within the period from 1992 October to 2010 April (Bosch & Savcenko, 2012). The period 1992-2010 exhibits a rather homogeneous data distribution and ensures that the MSS is hardly affected by seasonal variations or inter-annual variability like the 1997/1998 El Nino. The MSS heights are computed at the nodes of a regular $30' \times 30'$ geographical grid. The DGFI10 MSS is constructed by a careful pre-processing of the altimeter measurements followed by a remove-gridding-restore method. The pre-processing includes:

- (i) Application of the most recent orbits and mission specific correction models (e.g. for the sea state bias), see Chambers *et al.* (2003); Iijima *et al.* (1999); Scharroo & Smith (2010); Scharroo & Visser (1998); Schrama *et al.* (2000).
- (ii) Harmonization by applying identical geophysical reduction models as far as possible (e.g. for ocean tides), see Mayer-Gürr *et al.* (2011).
- (iii) Cross-calibration to estimate radial errors and range biases for each of the altimeter missions (for details see Dettmering & Bosch (2010b,a).

The ultimate goal of the pre-processing is to generate homogeneous and consistent multimission data which can be readily merged for the MSS computation. The interpolation of the pre-processed altimeter data to the $30' \times 30'$ grid was performed with instantaneous sea surface heights reduced by a reference surface, here the CLS01 MSS (Hernandez & Schaeffer, 2000). Compared to sea surface heights ($\simeq 100m$), the instantaneous sea surface heights (< 1 m) have significantly reduced gradients and are therefore much easier to interpolate. The along-track instantaneous heights were then averaged to fixed points along the nominal ground track and in a second step all mean instantaneous sea surface heights within the grid cells were averaged to a multimission mean anomaly. Finally, the CLS01 sea surface heights within the $30' \times 30'$ grid cells (themselves sampled with $2'$ spacing) were averaged and added back to the multimission mean anomaly. In this way the DGFI10 MSS represents a MSS for the period 1992-2010 with heights (averaged over $30' \times 30'$) defined on the nodes of a $30' \times 30'$ grid.

The DTU10 is a MSS available on a very dense grid. It has been computed by the Danish National Space Center, (Andersen, 2010). The DTU10 has a spatial resolution of 1 minute by 1 minute covering all marine regions of the world including the Arctic Ocean up to the North Pole (`http://www.space.dtu.dk/English/Research/Scientific_data_and_models/Global_Mean_sea_surface.aspx`).

Chapter 4

Filtering

The Mean Dynamic ocean Topography (MDT) is the deviation of the actual mean ocean surface (MSS) from the geoid. Since the geoid is the hypothetical surface of the ocean at rest it is the deviation of the actual ocean from its equilibrium. The MSS data represent local sea level averaged and interpolated onto nodes of a regular grid. The original data are altimetric measurements densely available along satellite tracks; these measurements contain information with spatial resolution much higher than is included in the geoid model. These short scale features must be removed by filtering, to make sure that the computed MDT is consistent with the spatial resolution of the geoid field, (Bingham, 2010), (Losch *et al.*, 2002). The problem of the spectral consistency will be discussed in detail in chapter 5. In this chapter we will discuss the problem of filtering.

4.1 Isotropic spherical harmonic spectral windows

We consider a function F expressed as a series of spherical harmonic functions:

$$F(P) = \sum_{\ell=0}^{L} \sum_{m=-\ell}^{\ell} f_{\ell m} Y_{\ell m}(P) \tag{4.1}$$

where $Y_{\ell m}$ are the spherical harmonic functions of degree ℓ and order m, $f_{\ell m}$ are the spherical harmonic coefficients and L is the maximum degree of the expansion. For reasons of compactness we choose here the complex form of spherical harmonic expansion, different from Eq. (2.1).

The filtering in the space domain is carried out by a convolution of F with the filter function $W(\psi)$:

$$\tilde{F}(P) = \frac{1}{4\pi} \iint W(\psi) F(Q) d\sigma_Q \tag{4.2}$$

where $W(\psi)$ is an isotropic weighting function that is only dependent on the spherical distance ψ between the points P and Q:

$$W(\psi) = \sum_{\ell=0}^{\infty} (2\ell+1) W_\ell P_\ell(\cos\psi) \ . \tag{4.3}$$

We recall the orthogonality of spherical harmonics:

$$\frac{1}{4\pi}\iint Y_{\ell m}(P)Y_{\ell' m'}(P)d\sigma = \delta_{\ell\ell'}\delta_{mm'} \ , \tag{4.4}$$

and the addition theorem of spherical harmonics:

$$P_\ell(\cos\psi_{PQ}) = \frac{1}{2\ell+1}\sum_{m=-\ell}^{\ell} Y_{\ell m}(P)Y_{\ell m}(Q) \ . \tag{4.5}$$

Inserting Eq. (4.1) and Eq. (4.3) in Eq. (4.2):

$$\tilde{F}(P) = \frac{1}{4\pi}\iint\left(\sum_{\ell'}(2\ell'+1)W_{\ell'}P_{\ell'}(\cos\psi)\right)\left(\sum_{\ell}\sum_{m} f_{\ell m}Y_{\ell m}(Q)\right)d\sigma_Q \ , \tag{4.6}$$

using (4.5), Eq. (4.6) becomes:

$$\begin{aligned}\tilde{F}(P) &= \frac{1}{4\pi}\iint\left(\sum_{\ell'}(2\ell'+1)W_{\ell'}\frac{1}{2\ell'+1}\sum_{m'}Y_{\ell'm'}(P)Y_{\ell'm'}(Q)\right)\left(\sum_{\ell}\sum_{m} f_{\ell m}Y_{\ell m}(Q)\right)d\sigma_Q = \\ &= \sum_{\ell'}\sum_{m'}\sum_{\ell}\sum_{m}(2\ell'+1)W_{\ell'}\frac{1}{2\ell'+1}f_{\ell m}Y_{\ell'm'}(P)\cdot\frac{1}{4\pi}\iint Y_{\ell'm'}(Q)Y_{\ell m}(Q)d\sigma_Q \ . \end{aligned} \tag{4.7}$$

Finally, using Eq. (4.4), we obtain the expression of the filtering in the spectral domain:

$$\tilde{F}(P) = \sum_{\ell}\sum_{m} W_\ell f_{\ell m}Y_{\ell m}(P) \ . \tag{4.8}$$

The convolution on the sphere corresponds to a simple multiplication with the filtering coefficients W_ℓ in the spherical harmonic spectral domain.

The inverse formula of Eq. (4.3) is:

$$W_\ell = \frac{1}{2}\int_0^\pi W(\psi)P_\ell(\cos\psi)\sin\psi d\psi \ . \tag{4.9}$$

It can easily obtained inserting $W(\psi)$ of Eq. (4.3) in (4.9) and recalling the orthogonality of the Legendre polynomials:

$$\frac{1}{2}\int_0^\pi P_n(\cos\psi)P_\ell(\cos\psi)\sin\psi d\psi = \frac{1}{2n+1}\delta_{n\ell} \ . \tag{4.10}$$

To filter the high frequencies (from k_0+1 to L) of the function F there are various alternatives. In this chapter we compare three filters.

Direct cut-off filter
The direct cut-off filter up to k_0, or ideal low pass filter, consists in choosing as maximum degree

$L = k_0$ in (4.1). An ideal low-pass filter completely eliminates all spectral content above the cut-off degree. The coefficients below will pass unchanged. The spectral weights are:

$$W_\ell = \begin{cases} 1 & \ell \leq k_0 \\ 0 & \ell > k_0 \end{cases} \tag{4.11}$$

The filter response in the spatial domain is a `sinc` function:

$$W(\psi) = \frac{\sin(\pi\psi)}{\pi\psi} \tag{4.12}$$

Unfortunately this type of filtering leads to an unnatural oscillation (Gibbs or ringing effects) in the spatial domain. The truncation artifacts appear as spurious ringing around the topography of the filtered surface.

Gauss filter

The Gauss filter corresponds to a Gaussian function in both the space and spectral domain. The formula for the weighting function W_ℓ for the Gauss filter is given in Jekeli (1981) and has been modified by Wahr *et al.* (1998). It can be computed by recursive formulas:

$$\begin{aligned} W_0 &= 1 \\ W_1 &= \left[\frac{1+e^{-2b}}{1-e^{-2b}} - \frac{1}{b}\right] \\ W_\ell &= -\frac{2\ell-1}{b} W_{\ell-1} + W_{\ell-2} \end{aligned}$$

where

$$b = \frac{\log 2}{1-\cos\alpha} \ . \tag{4.13}$$

The weighting function in the space domain for the Gauss filter is

$$W(\psi) = \frac{b}{2\pi} \frac{e^{-b(1-\cos\psi)}}{1-e^{-2b}} \tag{4.14}$$

As described in Zenner (2006), the half-weight radius r [in km] of the filter is related to the harmonic degree L of the spectrum by the empirical relation

$$r \approx \frac{1.45 \cdot 10^4}{L} [\mathrm{km}] \ . \tag{4.15}$$

The positive property of the Gauss filter is that it exhibits side lobes neither in the spectral nor in the spatial domain. However it significantly dampens the field at the highest spherical harmonic degrees and orders. The strength of the GOCE mission is its high spatial resolution. Thus, it must be tried to maintain its high degree and order coefficients as much as possible, filtering only the short scale features of the mean sea surface.

A "compromise": the Butterworth filter

The best solution for our problem would be to avoid the ringing effects and, at the same time, to preserve as much as possible the short scale information. A compromise could be considering an ideal low pass filter with smooth transition from 1 to 0. The Butterworth filter fulfills these needs. It has an extremely flat frequency response in the portion of the frequency spectrum that is transmitted (passband), see Fig. 4.1. The Butterworth filter is specified by two parameters, the filter order k and the cutoff frequency. The sharpness of the transition from the passband to the stopband is dictated by the filter order, as is shown in Fig. 4.2. Cutoff frequency for the ideal low-pass filters is determined as a frequency up to which the signals pass well and the signals beyond it are rejected. Due to the transition band in the no-ideal filters (as the Butterworth filter), the definition of cutoff frequency is unclear. By definition, it is determined as a frequency at which the power gain is $1/2$ of the power gain at the passband frequencies. Since the power of the signal is proportional to the squared magnitude response, the cutoff frequency of the Butterworth filter is that frequency where the magnitude response of the filter is $\sqrt{1/2}$. The ringing effect, in its transform in the spatial domain, is not eliminated, but it is strongly reduced compared with the ideal low pass filter, as described by Devaraju & Sneeuw (2012).

The three spectral weights corresponding to the three filters are shown in Fig. 4.3. The threshold frequency is $L = 180$ for the cutoff and the Gauss filter. The two parameters of the Butterworth filter are chosen empirically as function of the threshold frequency L. For $L = 180$ the order is chosen $k = 5$. If $k < 5$ the filter is stronger and we loose a larger part of the signal. If $k > 5$ the component of transmitted signal does not change significantly (the variations are less than 0.01 %). The cutoff frequency is chosen such that the passband is comparable with the passband of the Gauss filter and the ringing effect is sufficiently small. For $L = 180$ the cutoff frequency is chosen equal to 140.

Considering the ratio of the areas under the three curves of the Fig. 4.3 between 0 and 180, we observe that the Butterworth filter looses a moderate part of the signal during filtering 20.0% compared with the loss of the Gauss filter of 38.6%.

4.2 The filtering

We consider a MDT (see chapter 5 for more details) computed using the gravity model TUMGOCE up d/o 224 and extended up d/o 360 using the EGM2008 gravity model (TUMGOCEext), (Pavlis *et al.*, 2012). The MDT is extended to the land areas and defined on a geographical grid $30' \times 30'$. The surface is completely described by a set of spherical harmonic coefficients up d/o 360, see Fig. 4.4.

The spherical harmonic coefficients of its representation are weighted with the three functions of Fig. 4.3. The results in spatial and in spectral domains are shown in Fig. 4.5.

Considering the three filtered (up d/o 180) surfaces in a limited area (Agulhas current), see Fig. 4.6 and Fig. 4.7, we can observe the effect of the filters. As expected the cutoff filter causes a lot of ribbles (Gibbs effect). The Gauss filter produces a smoothed image, without ribbles, but also with less details. The Butterworth filter produces some roughness, but the image seems to be well defined. In particular, where the signal is stronger ($20° < \lambda < 30°, -40° < \varphi < -30°$) the representation is clearer.

A section along the parallel $\varphi = -40°$ of the three filtered surfaces is presented in Fig. 4.8. Butterworth (red line) and cutoff (green line) are almost the same where the signal is stronger ($10° < \lambda < 50°$). On the other hand, the Gauss filtered surface (blue line) is weaker; for example there is a 10 centimeter difference at $\lambda = 25°$. In the interval $(65° < \lambda < 85°)$ the ringing effect of the cutoff filter is particularly evident. In the same interval the signals of the Gauss and Butterworth filtered version show similar oscillations. The Gauss filter always generates a smoother surface compared with the two other filters.

Looking at the differences between the three filters, we observe that the Gauss filtered MDT is quite different from both cutoff (Fig. 4.9) and Butterworth (Fig. 4.10), particularly close to the strongest currents (Agulhas and Drake Passage currents). Cutoff and Butterworth (Fig. 4.11) show smaller differences, which appear more uniformly distributed.

Finally we compare the filtered MDT with an independent dataset. In Fig. 4.12, Fig. 4.13 and Fig. 4.14 the level curves of the MDT (gray lines) are compared with the Subantarctic and Polar Fronts[1] of the ACC current (red lines). Even in this case, even if there is no perfect matching, the best result occurs when Butterworth filtering is used.

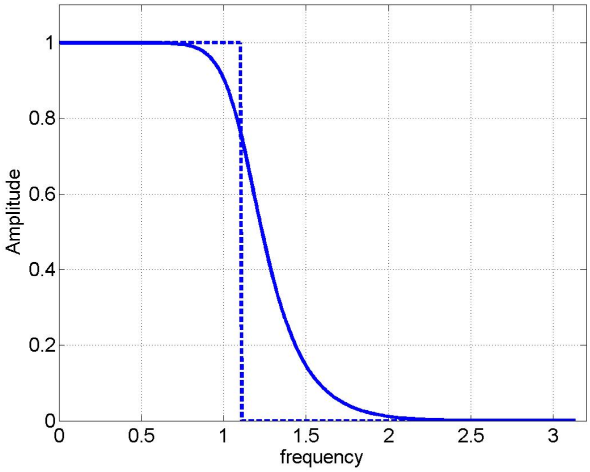

Figure 4.1: Butterworth filter of order $k = 5$ with normalized cutoff frequency equal to 0.35 (for details see Wade (1994)). The dotted line is the corresponding ideal boxcar filter.

---

[1] These fronts characterize the Antarctic Circumpolar Current (ACC), (Orsi *et al.*, 1995)

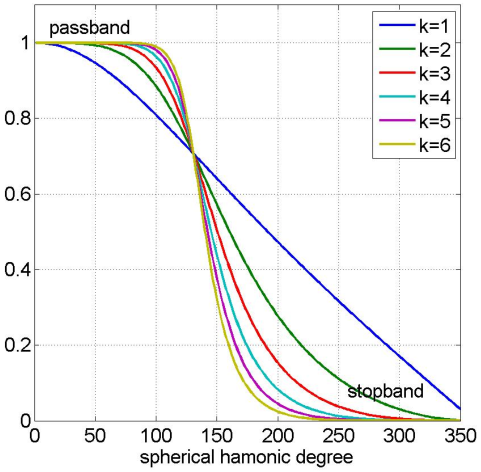

Figure 4.2: Frequency response of Butterworth filters with different orders k and with normalized cutoff frequency corresponding to $L = 180$.

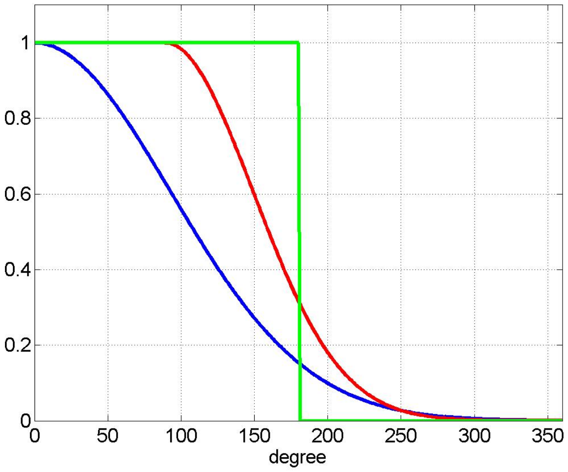

Figure 4.3: The cutoff filter up d/o 180 (green line) compared with the Gauss filter (blue line) and the Butterworth (red line) referring to the same threshold.

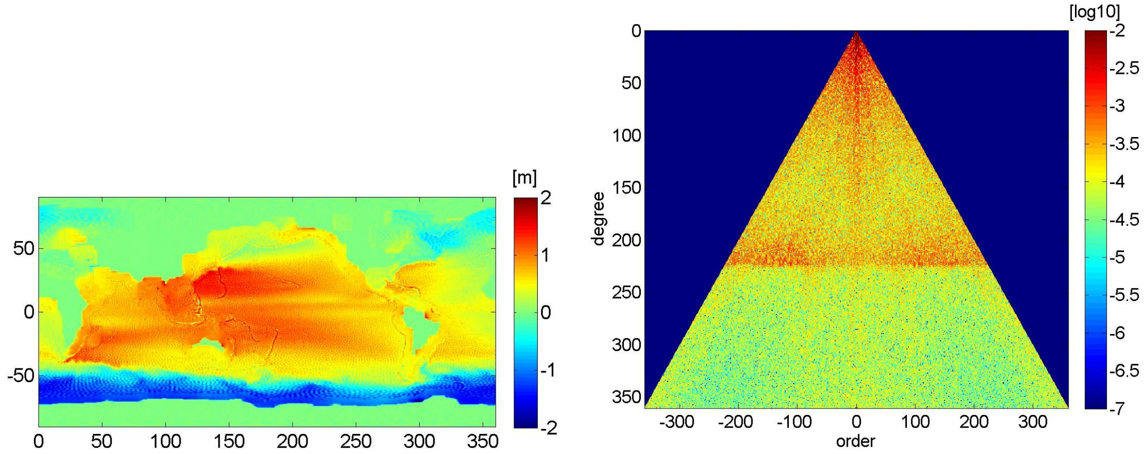

Figure 4.4: Extended MDT in spatial (left panel) and in spectral domain (right panel).

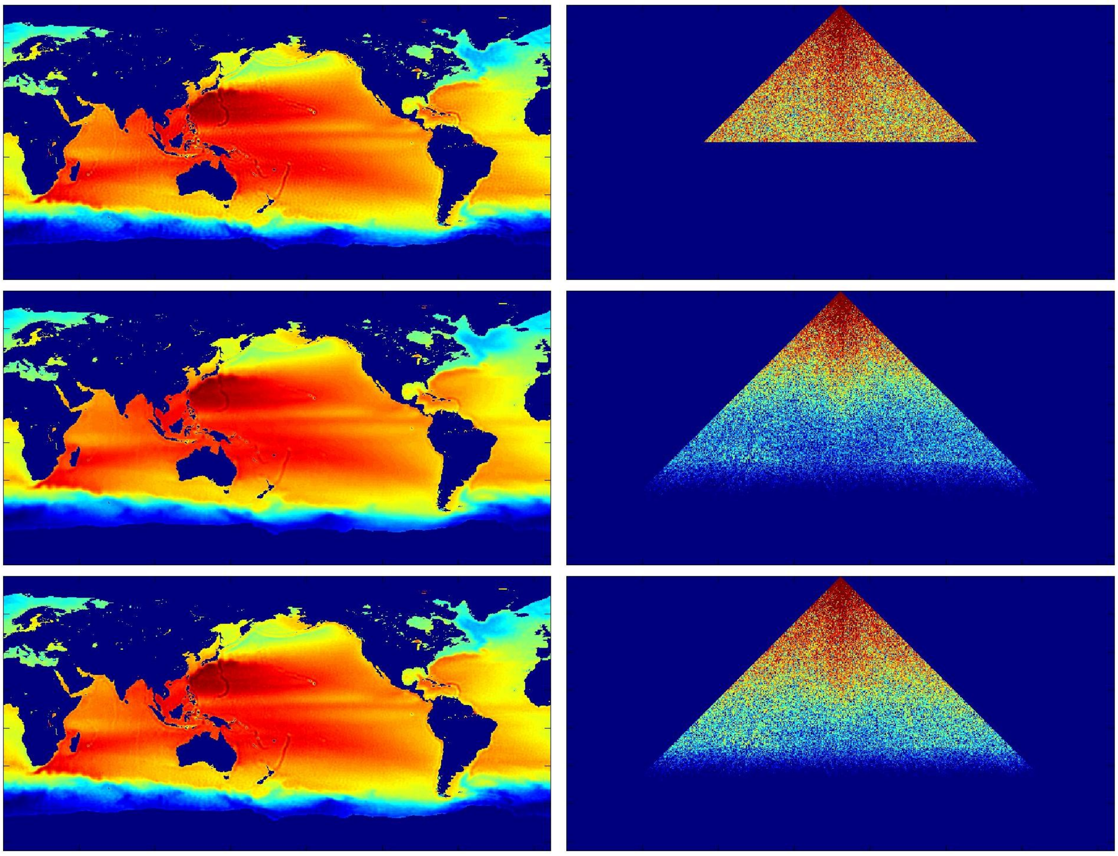

Figure 4.5: The filtered MDT up d/o 180 in spatial and spectral domain. Top panel = cut-off filter, middle panel = Gauss filter and bottom panel = Butterworth filter. The color scales are the same of Fig. 4.4

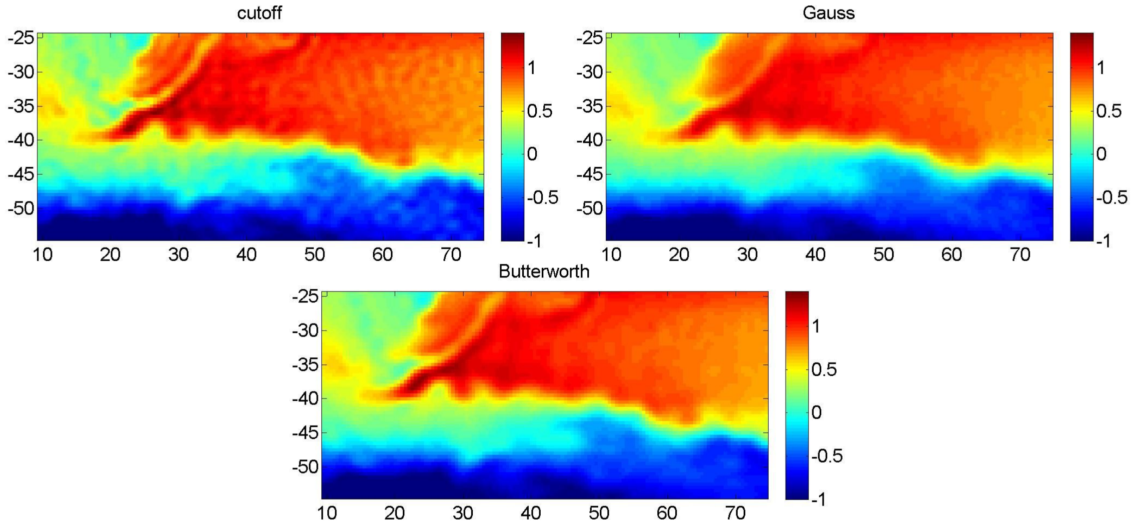

Figure 4.6: The filtered MDTs up d/o 180 in the Agulhas current area.

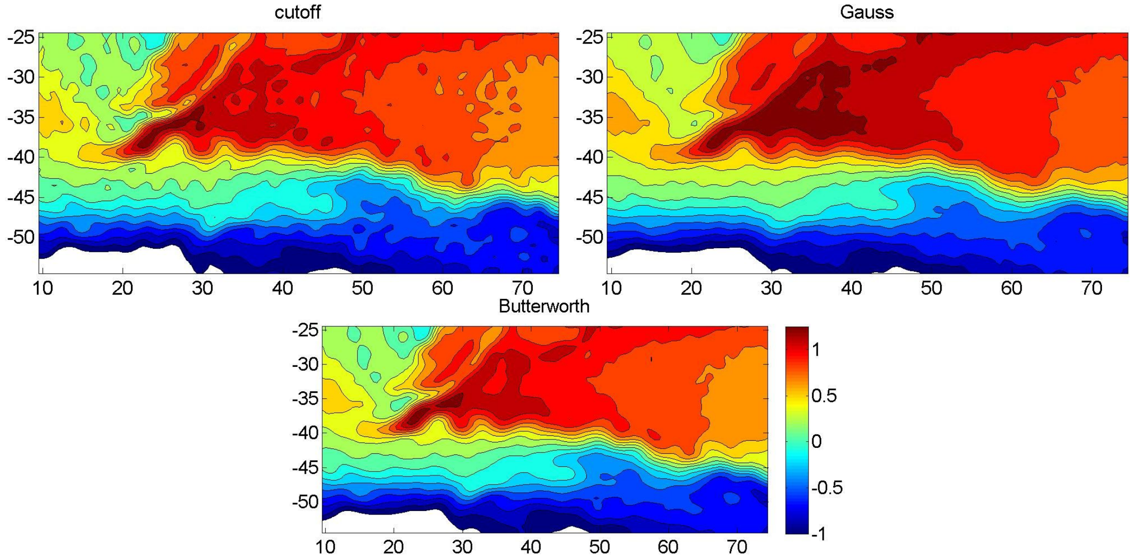

Figure 4.7: The filtered MDTs up d/o 180 in the Agulhas current area (contour plot).

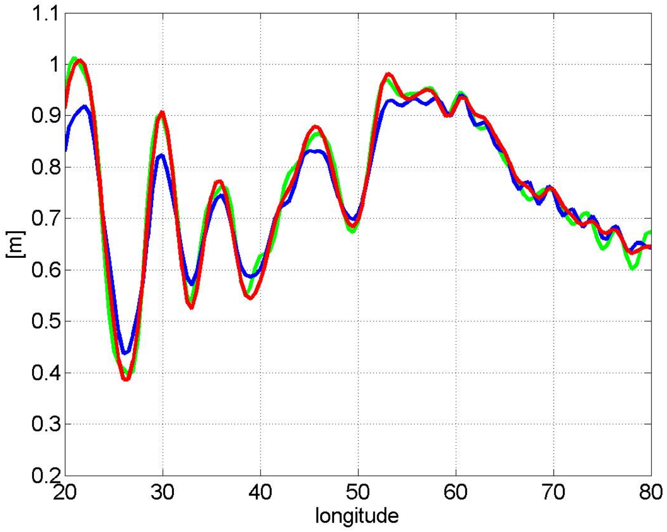

Figure 4.8: Sections along $\varphi = -40°$ of Gauss filtered MDT (blue line), cutoff filtered MDT (green line) and Butterworth filtered MDT (red line). The filters are applied up d/o 180.

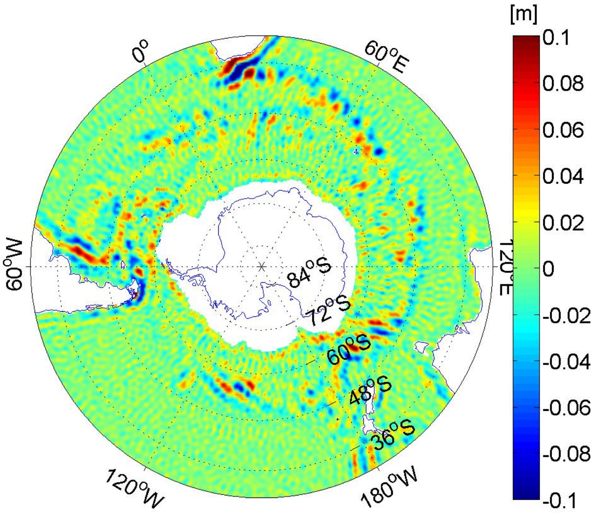

Figure 4.9: Differences between Gauss and Butterworth filtered MDT in the ACC area. The filters are applied up d/o 180. The RMS of the differences is 1.76 cm in the ACC area (1.60 cm globally).

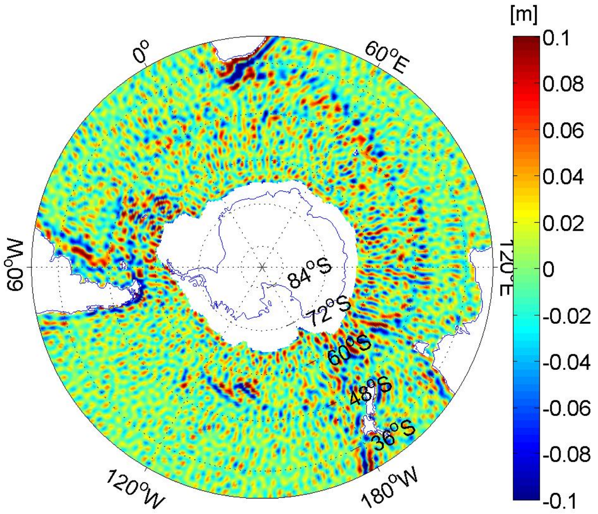

Figure 4.10: Differences between Gauss and cutoff filtered MDT in the ACC area. The filters are applied up d/o 180. The RMS of the differences is 3.18 cm in the ACC area (3.12 cm globally).

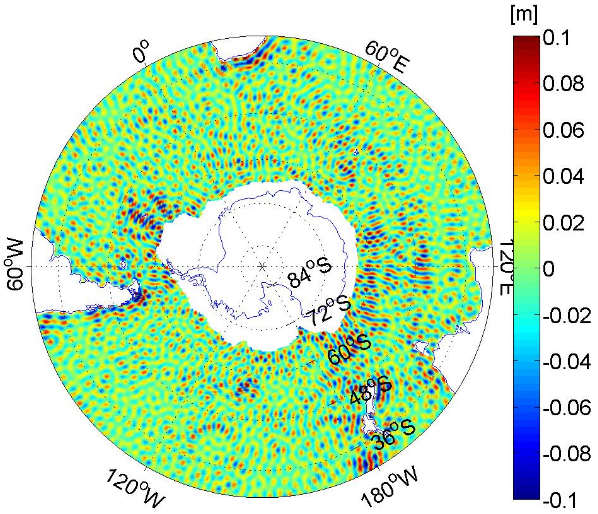

Figure 4.11: Differences between Butterworth and cutoff filtered MDT in the ACC area. The filters are applied up d/o 180. The RMS of the differences is 2.44 cm in the ACC area (2.42 cm globally).

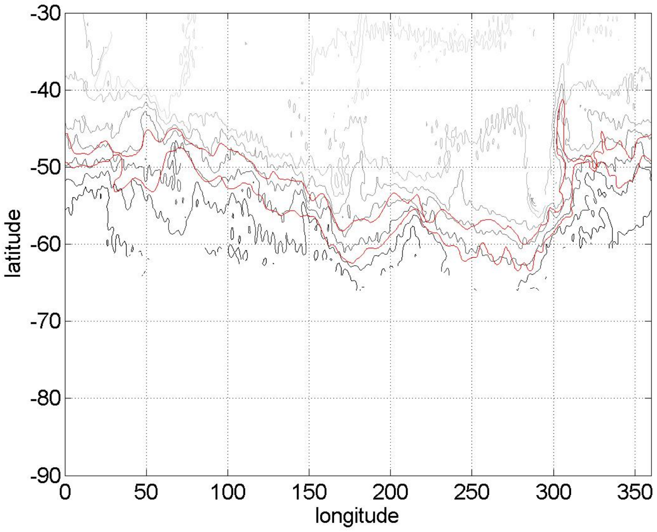

Figure 4.12: Level curves of the cutoff filtered up d/o 180 MDT and fronts of the ACC current (red lines).

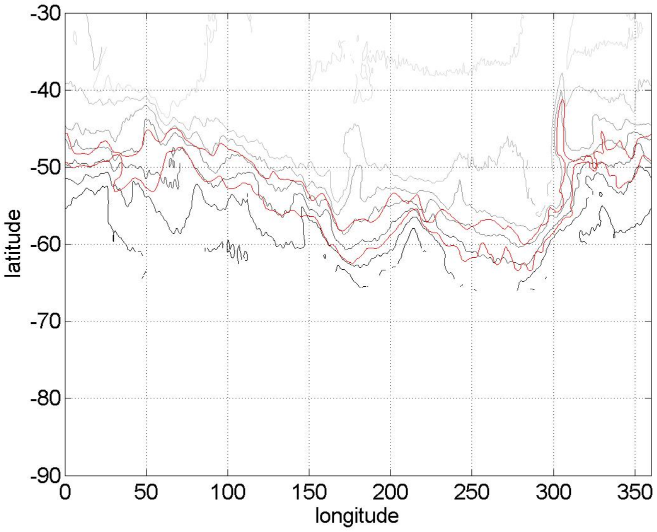

Figure 4.13: Level curves of the Gauss filtered up d/o 180 MDT and fronts of the ACC current (red lines).

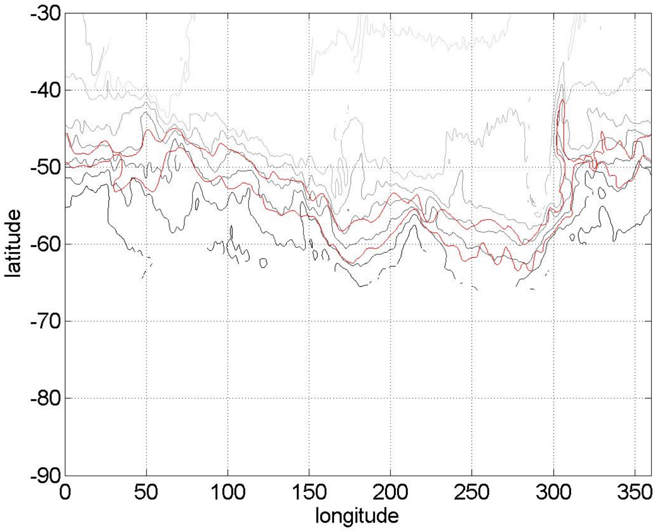

Figure 4.14: Level curves of the Butterworth filtered up d/o 180 MDT and fronts of the ACC current (red lines).

Chapter 5

Mean dynamic ocean topography (MDT)

The apparently simple geodetic approach for estimating the MDT by subtracting geoid heights N from the mean sea surface (MSS) heights h:

$$\mathrm{MDT} = H = h - N \tag{5.1}$$

is not as straightforward as it may seem. It requires special attention because data with fundamentally different characteristics, defined on different domains and with different spatial resolutions are to be combined.

Geoid and sea surface heights have to be consistent in terms of

- one common geodetic reference system,
- the same tide system, and
- their spectral content.

5.1 Geometrical consistency between geoid and MSS

5.1.1 Reference system

The mean sea surface h and the geoid heights N refer to an ellipsoidal reference system identified by four constants (gravitational constant times mass of the earth GM, equatorial radius a, angular velocity ω and flattening f).

Before subtracting the two quantities they have to be scaled to the same reference ellipsoid. If the dimensions of the reference ellipsoids (REF1 and REF2) differ, the change of the ellipsoidal heights (Heiskanen & Moritz, 1967, p. 207), is given by:

$$h_{REF2} = h_{REF1} - (a_{REF1} - a_{REF2}) + a_{REF1} \sin^2 \varphi (f_{REF1} - f_{REF2}). \tag{5.2}$$

where φ is the spherical geocentric latitude.

An analogous transformation holds for the transformation of the spherical harmonic coefficients

$$\left\{ \begin{array}{c} C_{\ell m}^{REF1} \\ S_{\ell m}^{REF1} \end{array} \right\} = \left(\frac{GM_{REF2}}{GM_{REF1}} \right) \cdot \left(\frac{a_{REF2}}{a_{REF1}} \right)^{\ell} \cdot \left\{ \begin{array}{c} C_{\ell m}^{REF2} \\ S_{\ell m}^{REF2} \end{array} \right\} \tag{5.3}$$

The DGFI10 MSS is referred to the TOPEX/POSEIDON earth ellipsoid:

- $GM_T = 3986004.415 \cdot 10^8 \text{ m}^3/s^2$,
- $a_T = 6378136.3$ m,
- $\omega = 7.922114 \cdot 10^{-5}$,
- $\frac{1}{f_T} = 298.257$.

The flattening and the equatorial radius are different for the reference ellipsoid of the gravity field ITG2010, which adopts the Geodetic Reference System 1980 (GRS80):

- $a_G = 6378137$ m,
- $\frac{1}{f_G} = 298.257222101$.

The GOCE-only gravity field TUMGOCE and the GOCO2 models consider an equatorial radius equal to $a = 6378136.3$ m.

In Fig. 5.1 the geometrical correction from the Topex ellipsoid to the GRS80 is shown[1]. In the following all the quantities are always referred to the Topex ellipsoid.

5.1.2 Tide system

The definition of the geoid is affected by the permanent deformation of the earth caused by the presence of the Sun and the Moon, (Hughes & Bingham, 2008). Consideration of these permanent tidal effects has led to the definition of three types of geoids:

- Tide-free (TF): the geoid with all (direct and indirect) effects of the Sun and Moon removed.
- Zero-tide (ZT): the geoid with the permanent direct effects of the Sun and Moon removed, but the indirect effect related to the elastic deformation of the earth retained.
- Mean-tide (MT): no permanent tide effect removed.

Conceptually, analogous definitions exist of an ellipsoid associated with the corresponding type of geoid (tide-free ellipsoid, mean-tide ellipsoid and zero-tide ellipsoid). There will be a different

---

[1] The TOPEX/POSEIDON ellipsoid is a mean-tide ellipsoid; the GRS80 ellipsoid is a tide free ellipsoid. The tide systems are defined in the section 5.1.2.

equatorial radius and flattening associated with each type of ellipsoid. If one considers a reference ellipsoid fixed by a definition of a and f, one will have different geoid undulations depending on the type of geoid undulation (tide free, mean, zero) that is being applied. The equations to convert from one system to another are (Fecher, 2008):

$$\begin{array}{rcl} N_{MT} - N_{ZT} & = & 9.9 - 29.6 \sin^2 \varphi \quad [\mathrm{cm}] \\ N_{ZT} - N_{TF} & = & k(9.9 - 29.6 \sin^2 \varphi) \quad [\mathrm{cm}] \\ N_{MT} - N_{TF} & = & (1+k)(9.9 - 29.6 \sin^2 \varphi) \quad [\mathrm{cm}] \end{array} \tag{5.4}$$

where k is the Love number.

The Love number for the permanent deformation of the earth is not really known, it is a best guess. This makes the TF-system problematic and "conventional". For example $k = 0.3$ is adopted for the EGM96 geopotential model, but not for all the geopotential models this number is taken.

In the case that the geoid undulations are to be used together with satellite altimeter data for the determination of MDT, the undulations must be given in a system consistent with that used for the determination of the sea surface height.

In particular we have:

- ITG2010 is given in the zero-tide system,
- TUMGOCE is given in the tide free system,
- GOCO2s is given in the tide free system,
- the MSSs are defined in the mean-tide system

In Fig. 5.2 the differences $(N_{ZT} - N_{MT})$ (blue line) and $(N_{TF} - N_{MT})$ (red line) are shown. In this case the considered model is GOCO2s up to degree and order 180.

Conversion between different permanent tide systems can also be executed modifying one spherical harmonic coefficient, (Losch & Seufer, 2003). To convert zero-tide coefficients to mean-tide, we can use:

$$\bar{C}_{2,0}^{\text{mean tide}} - \bar{C}_{2,0}^{\text{zero tide}} = \frac{(-0.198\ \mathrm{m}) r^3 g}{a^2 GM \sqrt{5}} \tag{5.5}$$

to convert tide-free coefficients to mean-tide, we can use:

$$\bar{C}_{2,0}^{\text{mean tide}} - \bar{C}_{2,0}^{\text{tide free}} = (1+k) \cdot \frac{(-0.198\ \mathrm{m}) r^3 g}{a^2 GM \sqrt{5}} \tag{5.6}$$

where g is the mean gravity and r is the local ellipsoidal radius[2].

In the following all the computations are done in the mean tide system.

---

[2] An approximation to this radius r is given by Heiskanen & Moritz (1967): $r(\varphi) = a(1 - f \sin^2 \varphi)$.

5.1.3 Coordinate system

The altimetric data are referred to the Topex ellipsoid and are expressed in ellipsoidal or geographic coordinates. The geoid is usually expressed in a spherical harmonic series using spherical coordinates, (see Fig. 5.3). For this reason each ellipsoidal (geographical) latitude ψ will be transformed to the corresponding spherical (geocentric) latitude φ with the formula

$$\tan\varphi = (1 - e^2) \cdot \tan\psi \tag{5.7}$$

where e is the eccentricity of the Topex/Poseidon ellipsoid. The longitudes are the same in the two systems.

5.2 Spectral consistency between geoid and MSS

5.2.1 Problem definition

The geoid heights $N(\vartheta, \lambda)$ as derived by GRACE or GOCE are commonly represented as a series of surface spherical harmonic functions, see Eq. (2.1). The latter are global base functions on the sphere. Since the spatial resolution of the geoid models is limited, the spherical harmonic series is truncated at some maximum harmonic degree L. Thus, there remains an unknown geoid part, represented by the spherical harmonic degrees and orders greater than L up to infinity. This part is denoted geoid omission error.

The altimetric MSS is measured along satellite ground tracks with very high sample rate. Also the spacing between adjacent tracks is rather dense. Disregarding the noise, the MSS heights h represent the sum of geoid and MDT, see Eq. (5.1). The spatial resolution of the MSS is therefore much higher than that of the given geoid heights, but it is not given globally but confined to (most of the) ocean areas.

Schematically the situation is represented in Fig. 5.4. Thus the altimetric MSS contains short scale geoid information that is not contained in the geoid models of GRACE and GOCE. After subtraction of the geoid model from the MSS this short scale geoid features would be misinterpreted as being part of the dynamic ocean topography. From Fig. 5.4 a variety of approaches can be deduced of how to deal with this fundamental problem:

- **Option 1:** Expansion of the solution space of N beyond L by an explicit modeling of the omission part of N, see Becker *et al.* (2012) and SPP1257-project RIFUGIO by Prof. W.-D. Schuh. In this case the missing geoid part will be described as part of the stochastic model.
- **Option 2:** Filtering of h down to L in the geographical domain and confinement of N to the ocean part, see Bosch & Savcenko (2010).
- **Option 3:** Artificial extension of h to land areas (make it a global function) and filtering to L in the spherical harmonic domain, see section 5.2.3.

5.2.2 Spectral consistency

The geoid is represented using the Eq. (2.1). For all degrees (and orders) less or equal to L, the coefficients of the geoid and their error variances (the commission error) are available. The signal for degrees above L is the omitted signal or omission error. The degree L corresponds approximately to a spatial scale of $20000/L$ km. Consequently, even a densely gridded geoid field does not contain spatial scales less than this.

The MSS data represent local sea level. The original data are altimetric measurements available along satellite tracks. This implies that each sample is of high spectral resolution. The short scale altimetric features will contain both dynamic topography and geoid features that need to be taken into account when calculating a consistent MDT. Furthermore Losch *et al.* (2002) shows that the omission error can leak in the commission error of the filtered signal if different base functions are involved for the representation of the geoid and the MSS. In the following section 5.2.3 the gravity model GOCO2s and the MSS DGFI10 are used throughout.

5.2.3 MDT from global approach

The basic idea is to represent both, h and N, in terms of spherical harmonic series. In this way the geoid and the sea surface have the same type of global spectral representation and they can be processed in a compatible form. Furthermore, with a common representation, the two surface functions can be filtered in a consistent way. Consequently, the altimetric sea surface has to be extended to the land areas so as to cover the entire earth's surface. This process requires much care in order to avoid boundary effects at the land/ocean transition.

We define as "land" all the areas where the altimetric data are not available, white areas in Fig. 5.5. Accordingly the land-ocean mask LO is defined as:

$$\mathrm{LO}(\varphi_i, \lambda_j) = \begin{cases} 1 & \text{if } (\varphi_i, \lambda_j) \in \text{ocean} \\ 0 & \text{if } (\varphi_i, \lambda_j) \in \text{land} \end{cases} \tag{5.8}$$

In particular, in the ACC area, the land-ocean transition is far from the boundary of Antarctica because of the inclination of the satellite altimetric missions and sea ice coverage, Fig 5.6.

We are considering a regular grid with $\Delta\varphi = \Delta\lambda = 30'$. In the spherical harmonic representation, the maximum resolvable degree L_{max} depends on the grid spacing in latitude and longitude direction according to

$$\Delta\varphi = \Delta\lambda = \frac{180}{L_{max}} \ . \tag{5.9}$$

This gives for our case $L_{max} = 360$. For this reason, we apply a narrow two-dimensional Gaussian filter to the full resolution MSS. We choose the averaging radius $r = 40.3$ km that corresponds to $L_{max} = 360$, see Eq. (4.15). That filtering corresponds to a light smoothing of the MSS and it makes the MSS more consistent with our grid. The differences after and before the smoothing are shown in Fig. 5.7.

Extending the altimetric sea surface to the land areas (e.g. by using a geoid model there) we introduce a discontinuity along the land-ocean transition. When a signal with a discontinuity is projected into a finite system of base functions, the well known ringing effect, also called Gibbs phenomenon, will happen around the discontinuity. This aspect is discussed in chapter 4.

The distortions along the transition zone from ocean to land cannot be eliminated completely, (Albertella & Rummel, 2009), but they can be strongly reduced using an appropriate reference surface on land, (Bingham *et al.*, 2008; Albertella *et al.*, 2012), and by smoothing the transition as much as possible.

We adopt the following scheme:

1. The first step is to compute the MDT simply by subtracting the geoid heights N from the MSS h, assigning to the land areas the value 0:

$$H = \begin{cases} h - N & \text{on ocean} \\ 0 & \text{on land} \end{cases} \tag{5.10}$$

   Now H can be expressed as a sum of spherical harmonics functions:

$$H(\vartheta, \lambda) = \sum_{\ell=0}^{L} \sum_{m=0}^{\ell} \left(C^H_{\ell m} \cos m\lambda_P + S^H_{\ell m} \sin m\lambda_P \right) \bar{P}_{\ell m} \cos(\vartheta_P) \tag{5.11}$$

   with $C^H_{\ell m}, S^H_{\ell m}$ the spherical harmonic coefficients of the expansion, L the highest degree considered and (ϑ, λ) the spherical latitude and longitude.

2. The second step is the smoothing of the land ocean transition. We tested three techniques.
   - In the first case an iterative remove-extrapolate-restore procedure is applied, as described in Albertella & Rummel (2009). We start considering the un-filtered MDT, Eq. (5.11), with its sharp land-ocean transition. Next we perform a global spherical harmonics analysis to get harmonic coefficients and then perform a synthesis to come back to the MDT. After this process, we get a new "mixed surface" on the globe. We keep the original MDT values on ocean, but fill the land with the derived "mixed surface". Then we repeat this process iteratively. Because this "mixed surface" on land is also affected by data from the ocean part, it will combine the ocean and land data so that the discontinuity between land and ocean will become smaller and smaller. We call this approach GL1.
   - In the second case we want to extend the MDT into the land areas with a surface "close" to the MDT and extremely smoothed. A simple solution is filling the land with mean values deduced from the ocean part (moving averages). The value $H(\varphi_i, \lambda_j)$ in each land point is replaced by a moving 2D box car average of the values of the surrounding grid points:

$$\bar{H}(\varphi_i, \lambda_j) = \frac{1}{(2k+1)^2} \sum_{p,q} H(\varphi_{i+p}, \lambda_{j+q}) \tag{5.12}$$

     where $p = -k, \ldots, k$ and $q = -k, \ldots, k$. The procedure is applied during n iterations, maintaining in each step the original values on sea and considering the new mean values on land. We call this approach GL2.
   - The third technique investigated solves the Laplace equation with the successive over-relaxation (SOR) iterative technique. This method of extending the dynamical ocean

topography is also known as "elastic membrane approach" (EMA). The solution is obtained by first prescribing the boundary conditions as the values of mean dynamical surface at the last observed point before the land gap, (Janjić *et al.*, 2012). After boundary conditions are specified the values in the interior points of the domain are calculated. Namely, let (i, j) be the index of the interior point. Simple discretization of Laplace equation with a second order finite difference scheme will give us

$$H_{ij}^{\tau+1} = \alpha \left[\frac{H_{i-1,j}^{\tau} + H_{i+1,j}^{\tau} - 2H_{i,j}^{\tau}}{\delta x^2} + \frac{H_{i,j-1}^{\tau} + H_{i,j+1}^{\tau} - 2H_{i,j}^{\tau}}{\delta y^2} \right] + H_{i,j}^{\tau} \tag{5.13}$$

where $H_{ij} = H(\varphi_i, \lambda_j)$ and τ is the iteration index; δx and δy are defined as $\delta x = a \cos \varphi \delta \lambda$ and $\delta y = a \delta \varphi$.

SOR method is an iterative technique that repeats evaluation of the above equation to update the value of i, j for the current iteration. The iterative process is continued until convergence is achieved in every interior point of the domain. In our experiments we performed 600 iterations with the relaxation parameter of 0.2.

The calculated solution of Laplace equation has several properties that are important for this application. First, the solution will be smooth, that is it will be differentiable to any degree. Second, the maximum and minimum values of the solution will be at the point of the boundary, and not at any interior point unless the solution is a constant.

The limitation in the EMA approach are boundary conditions, which in case of unfiltered data can be very inaccurate near the coast. One of the simple solutions would be e.g. to extrapolate in the radial directions towards the land interior before applying the EMA. This is not done in the experiments shown here. We call this approach GL3.

3. Finally a filter is applied to the spherical harmonic expansion of the derived global set of H.

In this scheme, we extend the MDT instead of the MSS, as suggested in Bingham *et al.* (2008), but the two procedures are equivalent because: (i) the size of the discontinuity along the land-ocean transition is the same and (ii) the relation between H and h and N is linear.

The three approaches (GL1, GL2 and GL3) are applied to a MDT derived from the MSS DGFI10 and the geoid TUMGOCE up d/o 224, Fig. 5.8.

The results in the ACC area are shown in Fig. 5.9.

The "extended" MDTs can be expressed as series of spherical harmonics functions:

$$\begin{aligned}
\mathrm{MDT}_{\mathrm{GL1}} &\overset{SHA}{\longrightarrow} \left\{C_{\ell m}^{GL1}, S_{\ell m}^{GL1}\right\} \overset{SHS}{\longrightarrow} \widetilde{\mathrm{MDT}}_{\mathrm{GL1}} \\
\mathrm{MDT}_{\mathrm{GL2}} &\overset{SHA}{\longrightarrow} \left\{C_{\ell m}^{GL2}, S_{\ell m}^{GL2}\right\} \overset{SHS}{\longrightarrow} \widetilde{\mathrm{MDT}}_{\mathrm{GL2}} \\
\mathrm{MDT}_{\mathrm{GL3}} &\overset{SHA}{\longrightarrow} \left\{C_{\ell m}^{GL3}, S_{\ell m}^{GL3}\right\} \overset{SHS}{\longrightarrow} \widetilde{\mathrm{MDT}}_{\mathrm{GL3}}
\end{aligned}$$

The differences on the ocean between the original MDT and the "extended" one, $\Delta_i = \mathrm{MDT}_{\mathrm{GLi}} - \widetilde{\mathrm{MDT}}_{\mathrm{GLi}}$, are not exactly equal to zero (see for example Fig. 5.10), but we have:

$$\mathrm{mean}(\Delta_1) = +4 \cdot 10^{-2} \text{ cm}, \ \mathrm{RMS}(\Delta_1) = 2.12 \text{ cm}$$

$$\mathrm{mean}(\Delta_2) = -4 \cdot 10^{-2}\ \mathrm{cm},\ \mathrm{RMS}(\Delta_2) = 2.66\ \mathrm{cm}$$
$$\mathrm{mean}(\Delta_3) = -1 \cdot 10^{-2}\ \mathrm{cm},\ \mathrm{RMS}(\Delta_3) = 2.17\ \mathrm{cm}.$$

This means that some discontinuities, which can be described completely only with an infinite sum of spherical harmonic functions, are still present. Small discontinuities along the land-ocean transition are spread over all the surface by spherical harmonic analysis and synthesis.

Fig. 5.11 shows the differences between the three solutions and the original MDT in the ACC area. The three solutions have more or less the same behavior. Also the spectra of the three surfaces (see Fig. 5.12 and Fig. 5.13) have the same appearances.

However the three approaches show different behavior along the land-ocean transition, see Fig. 5.14. The solution GL1 and GL2 show differences along all the coastlines, while GL1 and GL3 are mainly different along the southern boundary to Antarctica. The approach GL2 seems to deviate more from the other two. In the following we will adopt the GL2 solution.

Two cross sections of the three MDTs show that they can differ by several centimeters close to the land-ocean transition, see Fig. 5.15.

5.3 Mean Dynamic Ocean Topography computation

5.3.1 Different resolutions and an interpolation problem

In Fig. 5.16 is shown the MDT computed as described in section 5.2.3, using the GL2 solution and filtered with a Gauss filter up to degree and order 180. We can observe that the MDT shows some artificial wrinkles in the Pacific Ocean, not visible for example in the MDT computed with the profile approach (Bosch & Savcenko, 2010). Furthermore these wrinkles are still visible when different filters (cut-off, Gauss or Butterworth) are considered. These features correspond to the deepest areas in the bathymetry (Fig. 5.17), where geoid and MSS have an abrupt change.

In our computation we compute the MDT on a grid $30' \times 30'$, while originally the MSS is derived on a denser grid, following the distribution of the altimetric data. If we consider the MSS DGFI10, we observe that it is also available on the nodes of the grid $30' \times 30'$, but these values are the results of an interpolation from the original values along the altimetric tracks. That procedure produces an inconsistency where the gradient of the MSS is strongest. This effect is shown in the following example.

We compute the geoid heights N_{hr} on the nodes of a grid $20' \times 20'$ in the region within $-40° \leq \phi \leq -10°$ and $170° \leq \lambda \leq 195°$ (see left panel of Fig. 5.18). In this region the geoid has a strong variability (it varies from 10 m to 50 m in few kilometers). Then we use the values of N_{hr} to interpolate the geoid heights N_{lr} in the same area but on the nodes of a coarser grid $30' \times 30'$ (see middle panel of Fig. 5.18). Using Eq. (2.1), we compute the geoid heights $\bar{N}_{hr}$ on this second grid. The differences $N_{lr} - \bar{N}_{lr}$ can reach also 50 centimeters (right panel of Fig. 5.18). Of course when the denser grid contains all the points of the second grid $N_{lr} - \bar{N}_{lr} = 0$.

The problem can be solved computing the MDT, by Eq. (5.1), on a finer grid and only subsequently interpolating it on a coarser grid.

At this moment the MSS DGFI10 is available only on the grid $30' \times 30'$ and is therefore not suitable for the MDT computation with the global approach. For this reason in the following the DTU10 MSS is considered.

5.3.2 Summary of the previous results and a possible strategy for the computation of a high resolution MDT

There are different ways to obtain spectral consistency between mean sea surface and geoid height as described in section 5.2.1. We prefer to adopt the so-called global approach, which represents the MDT as a spherical harmonic series, because it permits to quantify the signal content in selected spectral windows. A problem of this approach is the need to complement the altimetric surface of the ocean by a corresponding surface on land (usually a high resolution so-called combined geoid model). Distortions in the spectral representation, in particular along the coastlines, cannot be avoided. In section 5.2.3, we described three methods to reduce the boundary effects at the land/ocean transitions which differ one from another by about 2 centimeters. We prefer to follow the solution GL2, which results in the fastest computation.

The satellite gravity models with highest resolution are derived from GOCE measurements. They are completely described on a grid $30' \times 30'$, because the maximum harmonic degree of their harmonic representation is 250. Anyway, in section 5.3.1 we show that in order to avoid interpolation problems it is necessary to consider a MSS with higher resolution. For this reason, in the following, we will use the MSS DTU10.

In chapter 4 we discussed the problem of the filtering. We found that the best solution is the Butterworth filter, because it strongly reduces the ringing effects and, at the same time, it preserves as much as possible the short scale information. In the following we consider that filter. Empirically we found that the best results are obtained with the order of the Butterworth $k = 5$. Its threshold frequency f can be empirically linked to the maximum harmonic degree L. We found:

$$f = 0.002 \cdot L \; . \tag{5.14}$$

In Fig. 5.19 the Butterworth filter with order $k = 5$ and $f = 0.002 \cdot 180$ is shown. The most recent gravity models from GOCE observations are available up to degree and order $L = 224$, 250 and even 260. The right panel of the Fig. 5.19 shows the frequency response of the Butterworth filter for the highest frequencies (corresponding to the harmonic degree from 200 to 320). Applying the filter to a model truncated at 224, 250 or 260, a sharp transition is inevitably introduced. To avoid this problem we use the gravity model TUMGOCE up to degree and order 224 and extended up to degree and order 720 using the EGM2008 gravity model. Due to the shape of the Butterworth filter, the frequencies recovered by GOCE are passed with very little attenuation and the frequencies from EGM2008 are almost eliminated.

The MDT described is called MDT-GOCE-DTU-xxx, where xxx indicates the size of the filter in terms of maximum harmonic degree. An example of MDT computed following the previous instructions is shown in Fig. 5.20 and Fig. 5.21.

5.3.3 External comparisons

The MDT-GOCE-DTU up to different degrees is compared with an independent MDT model computed by Maximenko *et al.* (2009). The latter, shown in the upper panels of Fig. 5.22 and

	mean	**RMS**
MAX-(MDT-GOCE-DTU-90)	-1.70	5.45
MAX-(MDT-GOCE-DTU-120)	-1.72	5.63
MAX-(MDT-GOCE-DTU-150)	-1.73	5.83
MAX-(MDT-GOCE-DTU-180)	-1.75	6.08
MAX-(MDT-GOCE-DTU-210)	-1.75	6.45

Table 5.1: Statistics of the differences between the Maximenko's MDT and the geodetic ones. Units are cm.

Fig. 5.23, is calculated using jointly data of satellite altimetry (data from 1992 to 2002), near-surface drifters, NCEP wind data and a GRACE gravity model. The data has been obtained from Nikolai Maximenko (International Pacific Research Center, School of Ocean and Earth Science and Technology, University of Hawaii) and Peter Niiler (Scripps Institution of Oceanography, University of California).

The MDT from Maximenko and the MDT-GOCE-DTU (lower panel of Fig. 5.22 and Fig. 5.23) are computed considering different land-ocean masks, as it is shown in Fig. 5.24. In the following if an area is land in one of the two masks it is considered land.

In Fig. 5.25 the differences between the Maximenko's MDT and the geodetic MDT-GOCE-DTU-120 are shown. The stronger differences coincide with the major oceanic currents (Gulf, Kuroshio and ACC), where the Maximenko solution is less intense. The MDT computed by Maximenko has less spatial resolution. Therefore, to obtain a better comparison, the geodetic MDT is filtered with different thresholds. The RMS of the differences, when different filters are applied, are reported in Table 5.1. Globally the RMS of the differences is from 5 to 6 centimeters.

More specifically we are aware that the Maximenko's MDT is smoother than MDT-GOCE-DTU even if the filter is only up to degree and order 120, see from Fig. 5.26 to Fig. 5.30. The RMS of the regional differences for different filters are reported in Table 5.2.

	Gulf		**Agulhas**		**Malvinas**		**Kuroshio**		**ACC**	
	mean	**RMS**	**mean**	**RMS**	**mean**	**RMS**	**mean**	**RMS**	**mean**	**RMS**
MAX-(MDT-GOCE-90)	0.64	5.37	-4.52	6.84	-4.13	6.57	1.07	5.76	-3.73	6.18
MAX-(MDT-GOCE-120)	0.64	5.56	-4.53	7.08	-4.12	6.70	1.04	5.94	-3.74	6.33
MAX-(MDT-GOCE-150)	0.64	5.80	-4.53	7.39	-4.12	7.03	1.02	6.17	-3.75	6.51
MAX-(MDT-GOCE-180)	0.63	6.10	-4.52	7.67	-4.11	7.38	1.01	6.44	-3.76	6.73
MAX-(MDT-GOCE-210)	0.62	6.49	-4.52	8.01	-4.11	7.77	0.99	6.78	-3.77	7.09

Table 5.2: Statistics of the regional differences between the Maximenko's MDT and the geodetic MDT-GOCE-DTU when different thresholds of the filter are considered. Units are cm.

5.4 Bandwidth analysis

The spherical harmonic representation Eq. (5.11) of the MDT allows analyzing the information contained in different spectral bands. The bandwidth analysis target is to show which is the contribution of GOCE in the determination of the highest harmonic components of the MDT. For the comparison a MDT computed using only GRACE data is considered. In the following we consider:

MDT-GRACE-DTU : computed using the gravity model ITG-Grace2010

MDT-GOCE-DTU : computed using the gravity model TUMGOCEext.

The better bandwidth analysis is obtained applying a Gauss filter, because using the Butterworth filter the bandwidths are slightly noisy. Four bandwidths are considered as it is shown in Fig. 5.31.

We know that the spherical harmonic representation of the MDT can only be divided into spectral bands, if they are independent, i.e. if there exist no correlations between the coefficients of the various bands. In reality some (rather small) correlations exist. Their neglect has only a small effect and is disregarded here.

In Fig. 5.32 and Fig. 5.33, different bandwidths of MDT-GOCE-DTU and MDT-GRACE-DTU are shown. In the first band, from spherical harmonic degree 90 up to 120, the spectral content is almost the same. Between 120 and 150 the MDT band based on GRACE begins to become noisy, while typical ocean current features are still clearly discernible even up to degree 180 when TUMGOCE model is used. This demonstrates that (i) such short scales still contain significant oceanographic signal and (ii) this signal can be discerned using a GOCE high resolution gravity model.

The filtering, up to degree $L = 180$, is not able to eliminate the short scale distortions in the GRACE solution and the oceanic signal is partially obscured. In addition, we know that the performance of GRACE models is lower above d/o 120. On the other hand, at the scales corresponding to $L = 180$ (≈ 111 km) the MDT from GOCE data shows more oceanographic details, reflecting the features related to the major ocean currents. This is even clearer in the regional plots (Gulf current in Fig. 5.34 and Fig. 5.35, Kuroshio current in Fig. 5.36 and Fig. 5.37, Agulhas current in Fig. 5.40 and Fig. 5.41, ACC current in Fig. 5.42 and Fig. 5.43).

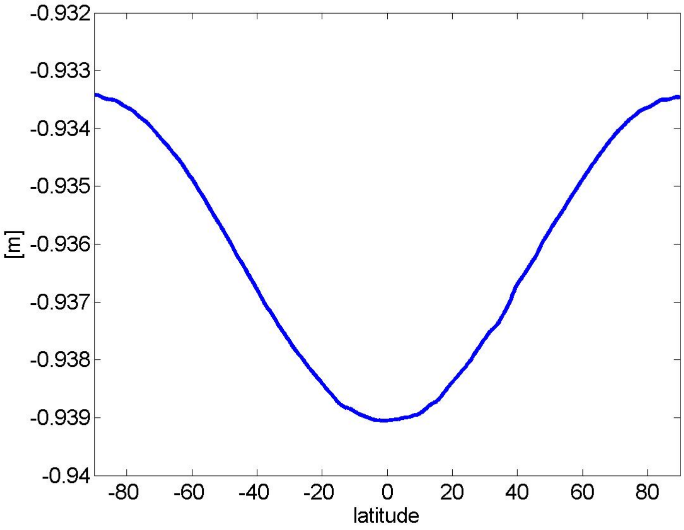

Figure 5.1: Geometrical corrections from REF1 = Topex ellipsoid to REF2 = GRS80.

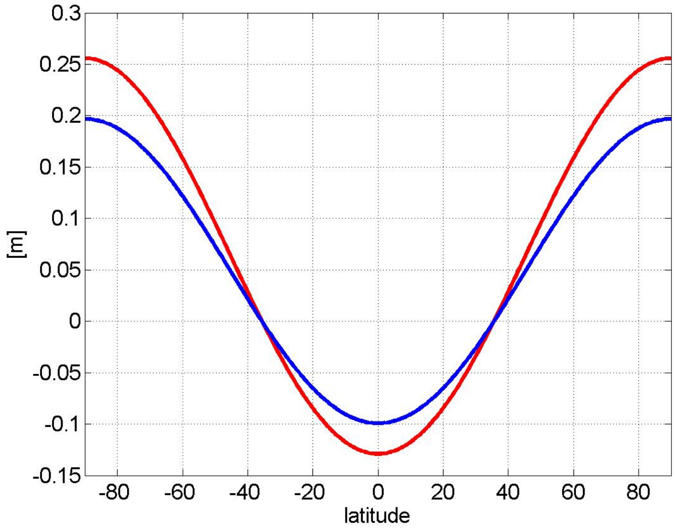

Figure 5.2: Corrections for the transformations between tide-free and zero-tide system (blue line) and tide-free and mean-tide system (red line).

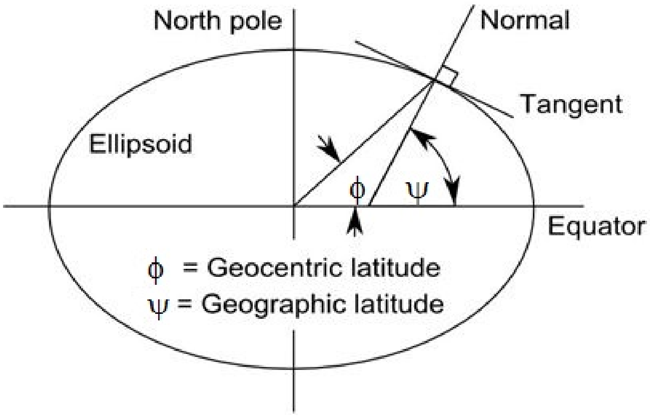

Figure 5.3: Geocentric and geographic latitude.

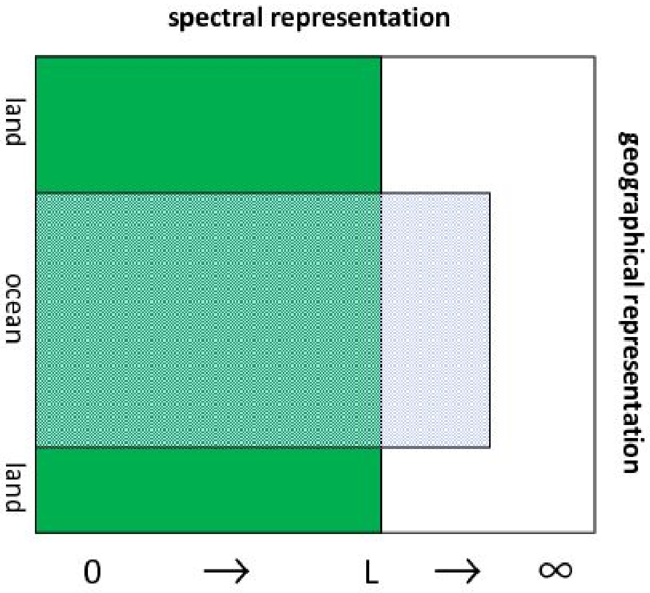

Figure 5.4: Schematic representation of the MSS h confined to oceanic areas (light blue) but with very high spectral resolution, and of N (green) with a global geographical coverage but a spectral resolution up to only L.

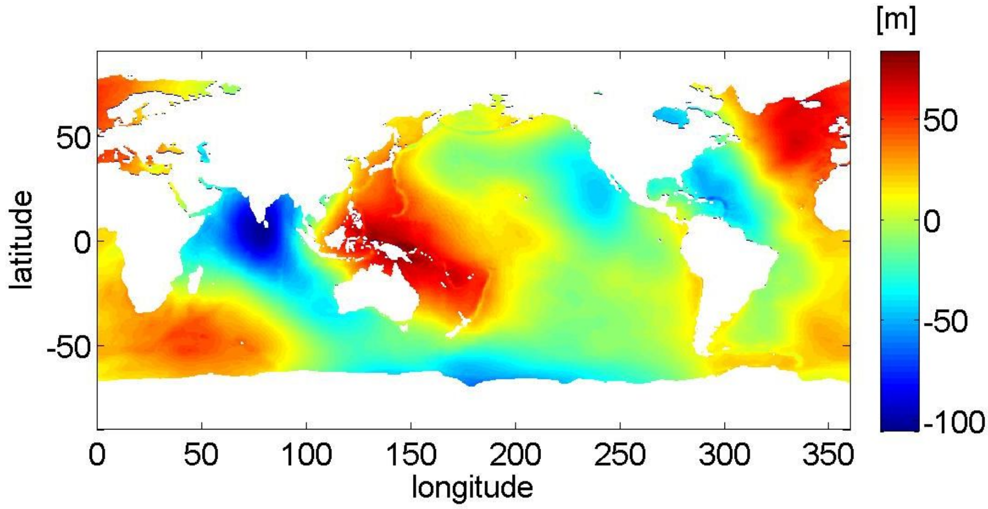

Figure 5.5: The DGFI10 MSS. The areas without altimetric data are shown in white.

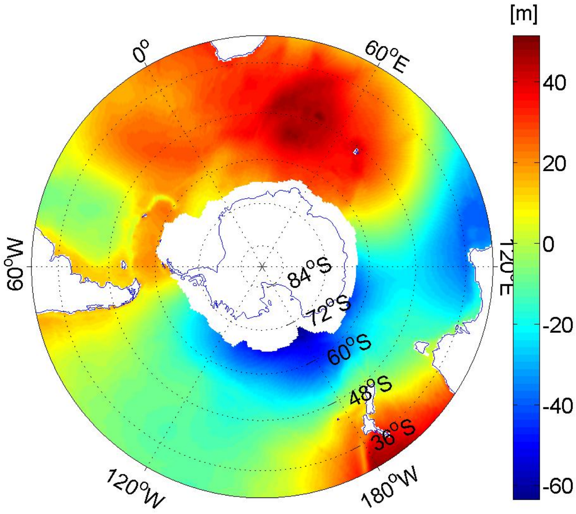

Figure 5.6: The DGFI10 MSS in the ACC area. The areas without altimetric data are shown in white.

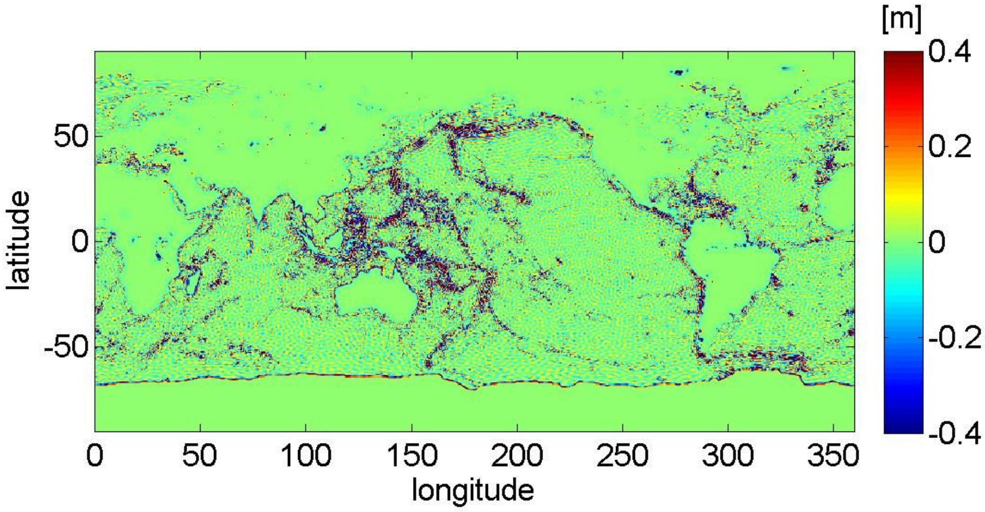

Figure 5.7: Differences between the full resolution MSS and the smoothed one. The RMS of the differences is 11.05 cm.

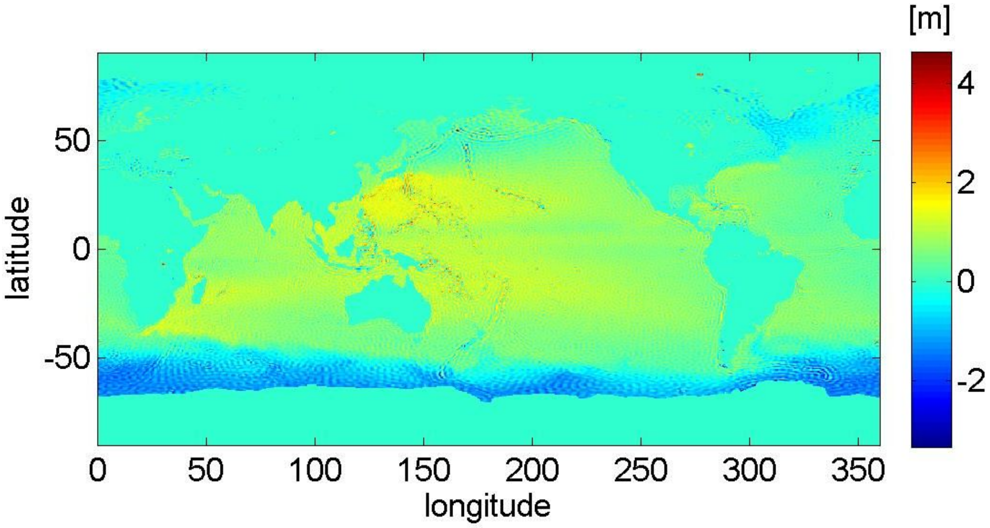

Figure 5.8: Un-filtered MDT from DGFI10 and the TUMGOCE geoid (up d/o 224).

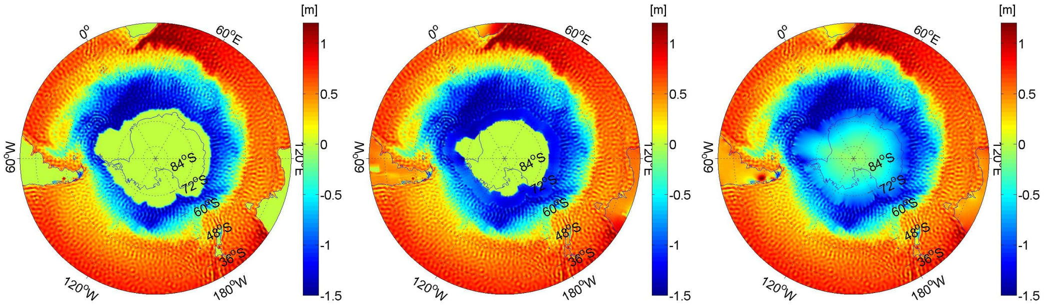

Figure 5.9: The “extended” MDT in the ACC area. The approaches GL1 (left), GL2 (middle) and GL3 (right) are applied.

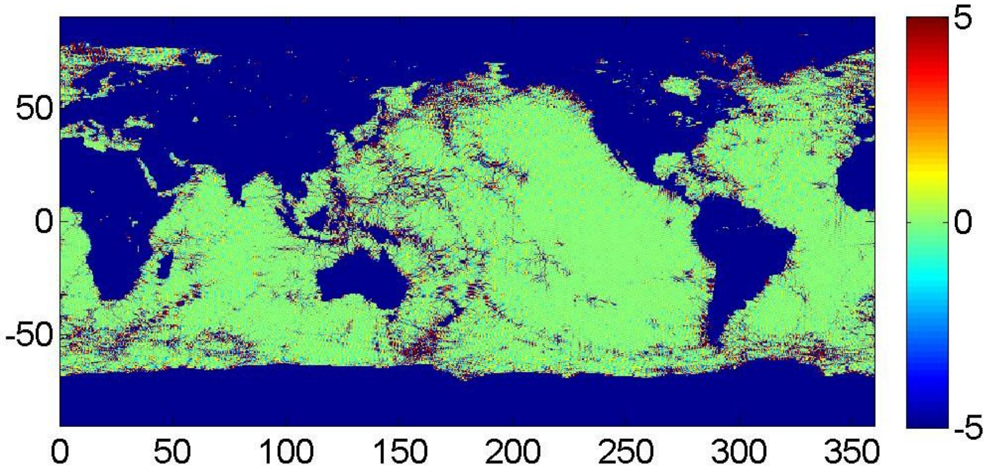

Figure 5.10: Differences Δ_2 on the oceans. Units are cm.

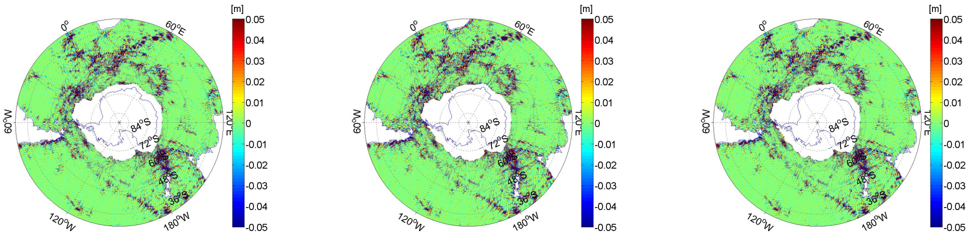

Figure 5.11: Differences between the three global approaches (GL1 on the left panel, GL2 in the middle panel and GL3 in the right one) and the original MDTor. The RMS of the differences in the ACC area are: RMS(GL1-MDTor) = 2.27 cm, RMS(GL2-MDTor) = 2.64 cm and RMS(GL3-MDTor) = 2.28 cm.

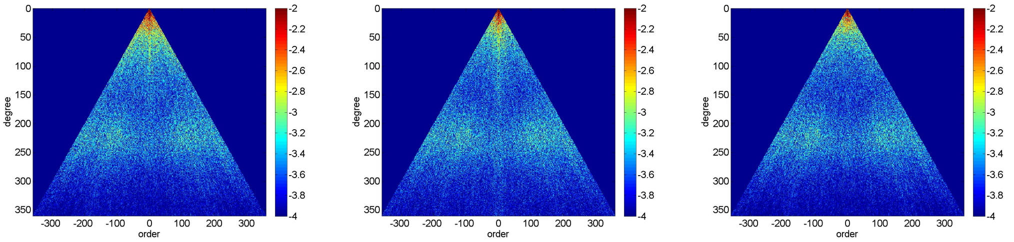

Figure 5.12: The spherical harmonic spectra of the three global approaches (GL1 on the left panel, GL2 in the middle panel and GL3 in the right one). The scale is logarithmic.

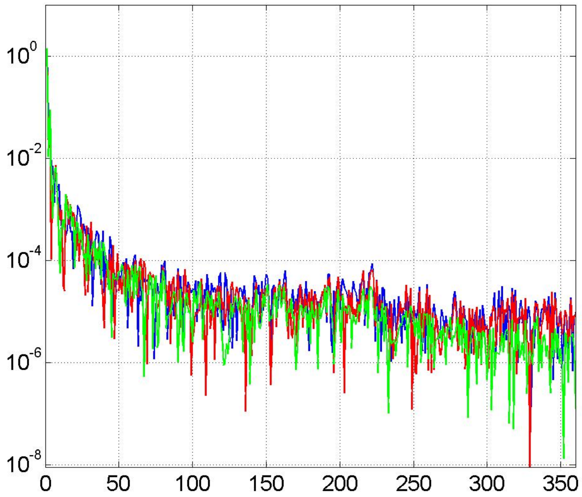

Figure 5.13: Degree variances of the spherical harmonic coefficients for the three global approaches: blue line = GL1, red line = GL2, green line = GL3.

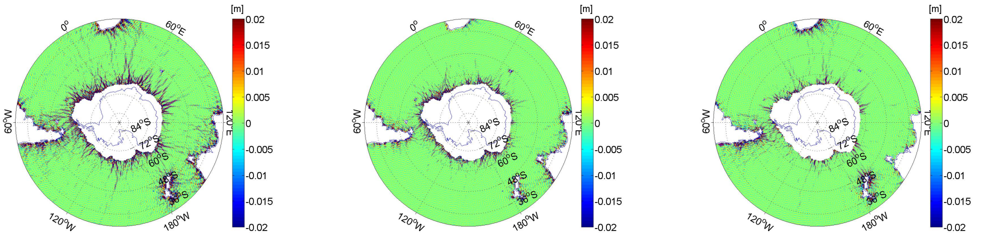

Figure 5.14: MDT differences from $\mathrm{MDT_{GL1}}$ and $\mathrm{MDT_{GL2}}$ (left panel), from $\mathrm{MDT_{GL1}}$ and $\mathrm{MDT_{GL3}}$ (middle panel) and from $\mathrm{MDT_{GL2}}$ and $\mathrm{MDT_{GL3}}$ (right panel). Units are meters.

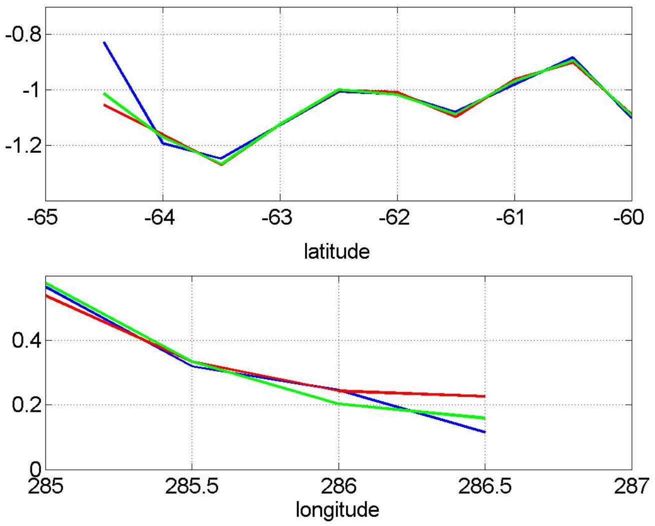

Figure 5.15: Sections of the MDTs along $\lambda = 60°$ (upper panel) and along $\varphi = -45°$ (lower panel). $\mathrm{MDT_{GL1}}$ is represented with the blue line, $\mathrm{MDT_{GL2}}$ with the red line and the $\mathrm{MDT_{GL3}}$ with the green line.

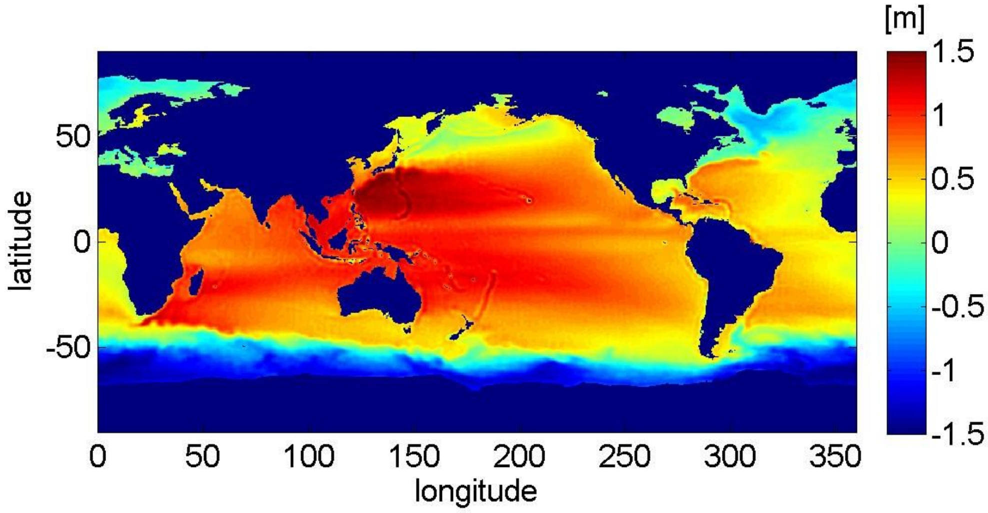

Figure 5.16: The MDT computed on $30' \times 30'$ using the gravity model GOCO2s and the MSS DGFI10. Gauss filter up to degree and order 180 is applied.

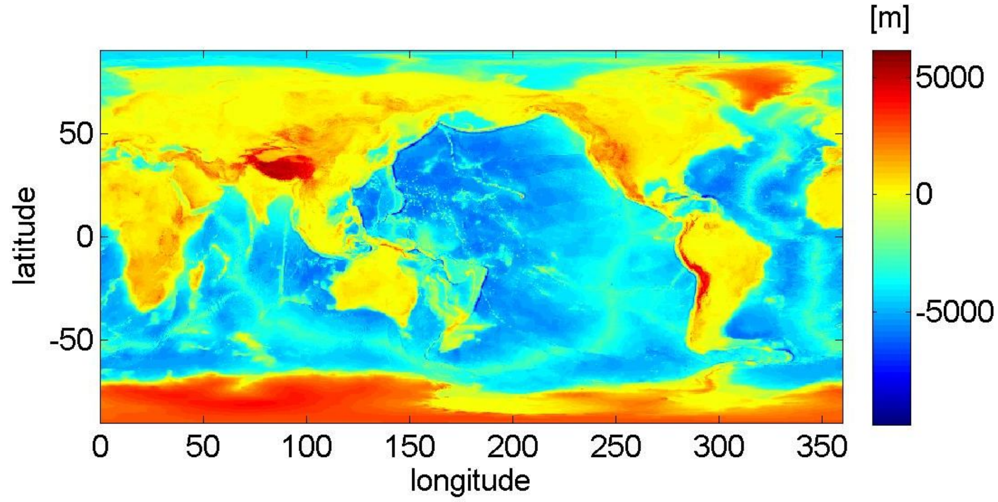

Figure 5.17: The General Bathymetric Chart of the Oceans (GEBCO) on a 5 minute grid ((Monahan, 2008)).

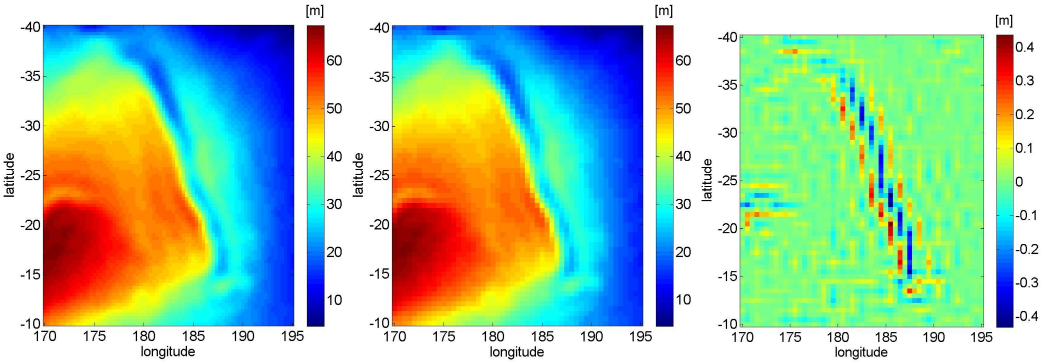

Figure 5.18: Geoid heights with different resolution in the same area and their difference (right panel).

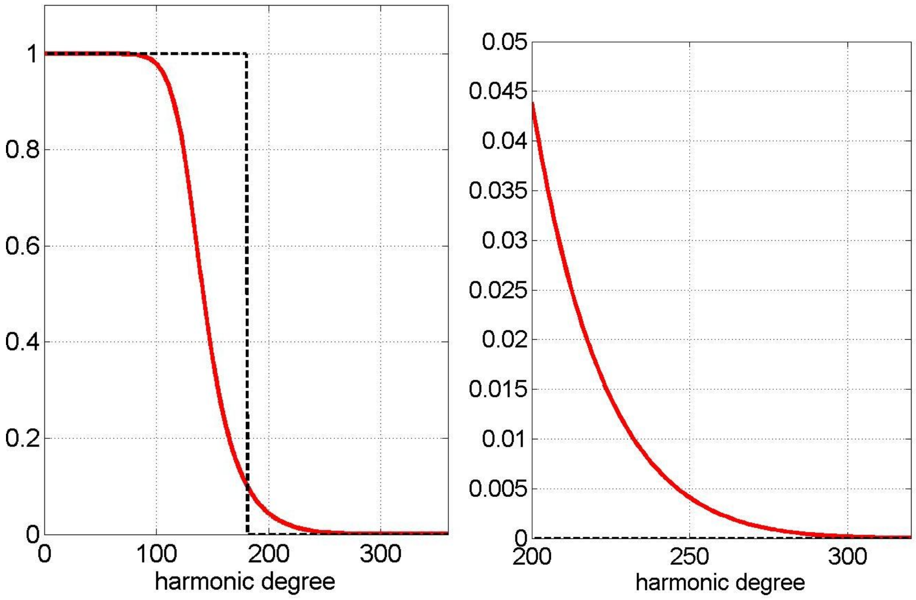

Figure 5.19: Left panel: frequency response of Butterworth filters with order $k = 5$ and frequency $f = 0.036$ as function of the harmonic degree; the dotted black line is the corresponding cutoff filter. Right panel: zoom on the highest frequencies.

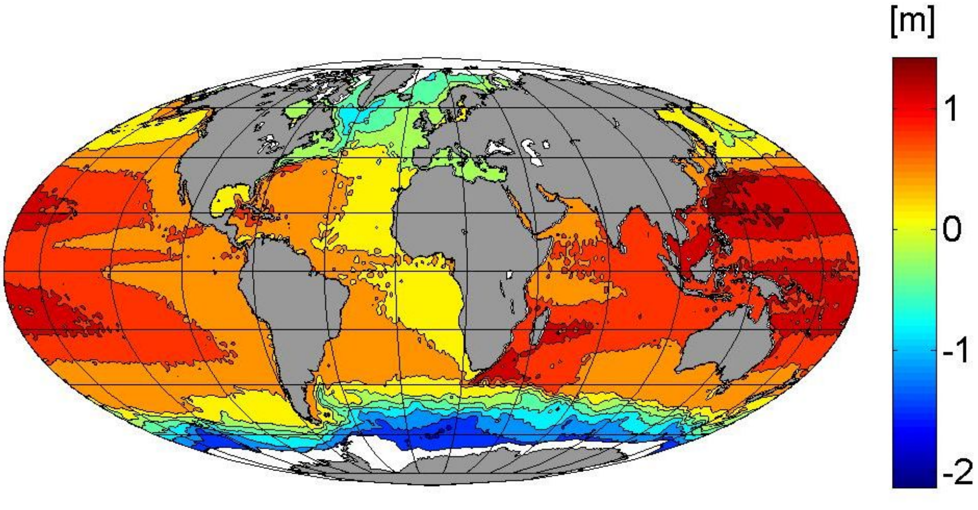

Figure 5.20: The global geodetic MDT-GOCE-DTU-180.

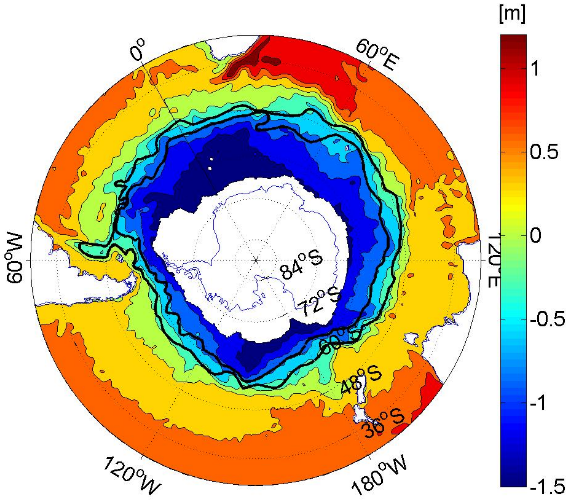

Figure 5.21: The geodetic MDT-GOCE-DTU-180 in the Antarctic Circumpolar Current area. The black lines are the fronts which define different regions of the ACC. These regions are characterized by various water properties, see for details (Orsi *et al.*, 1995).

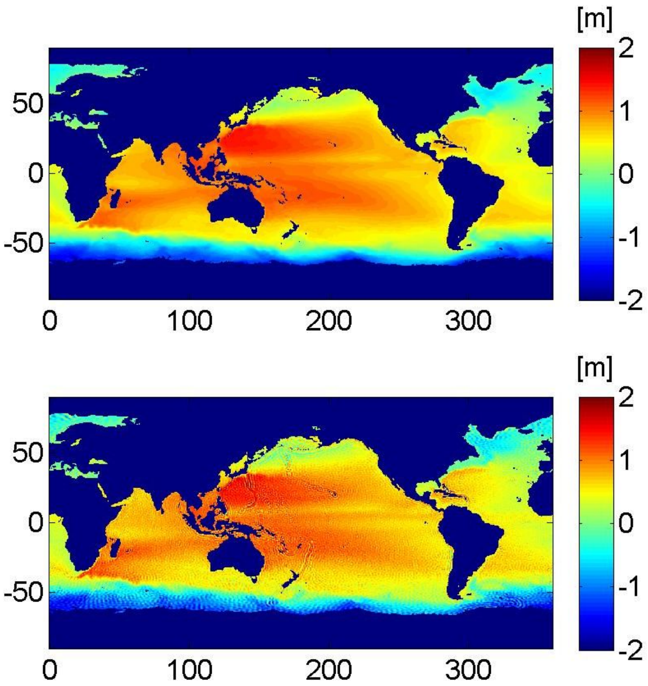

Figure 5.22: Upper panel: MDT described in Maximenko *et al.* (2009). Lower panel: the MDT-GOCE-DTU described in section 5.3.2, no filter is applied.

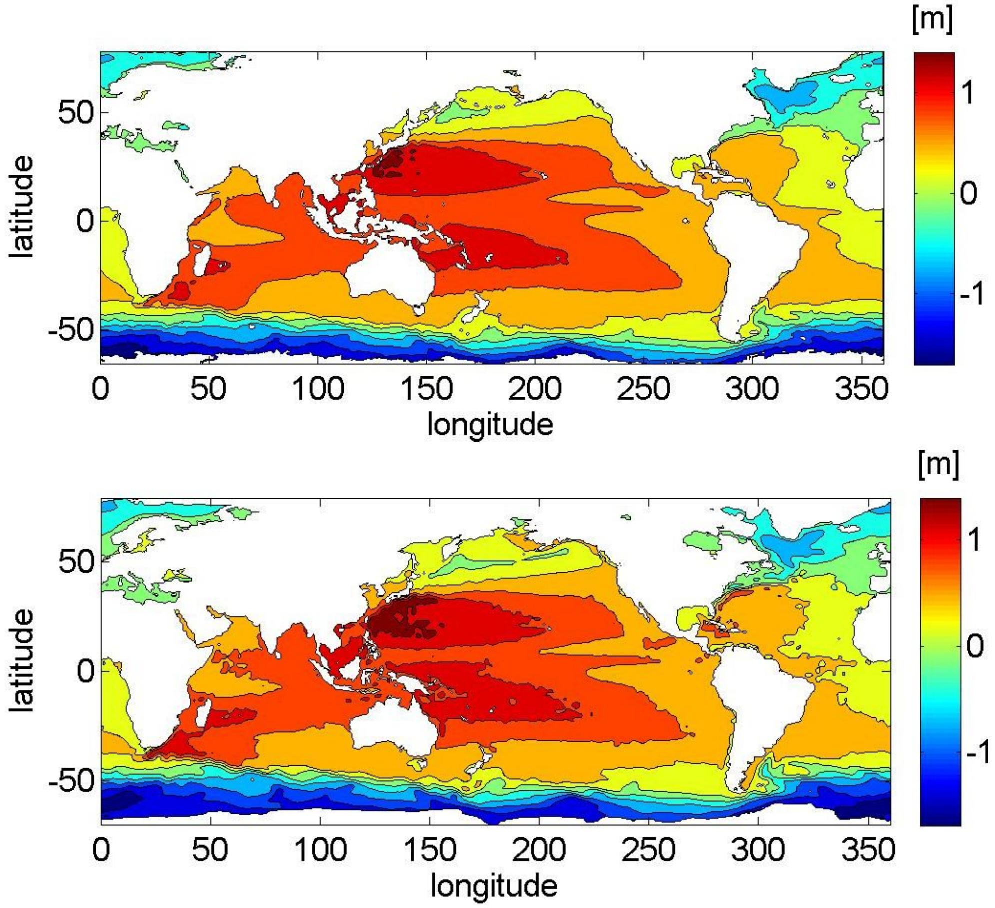

Figure 5.23: Upper panel: MDT described in Maximenko *et al.* (2009). Lower panel: the MDT-GOCE-DTU-120 described in section 5.3.2. Contour plots.

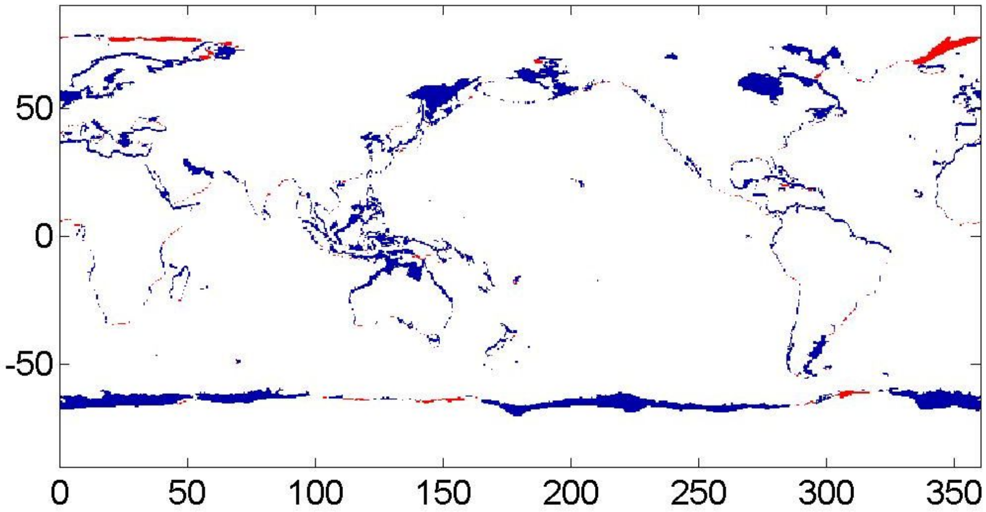

Figure 5.24: Distribution of data for the Maximenko's MDT and for the MDT-GOCE-DTU. In blue the areas considered land in Maximenko and ocean in our computation. In red the areas considered ocean in Maximenko and land in our computation. In the following all these incongruous areas are considered as land.

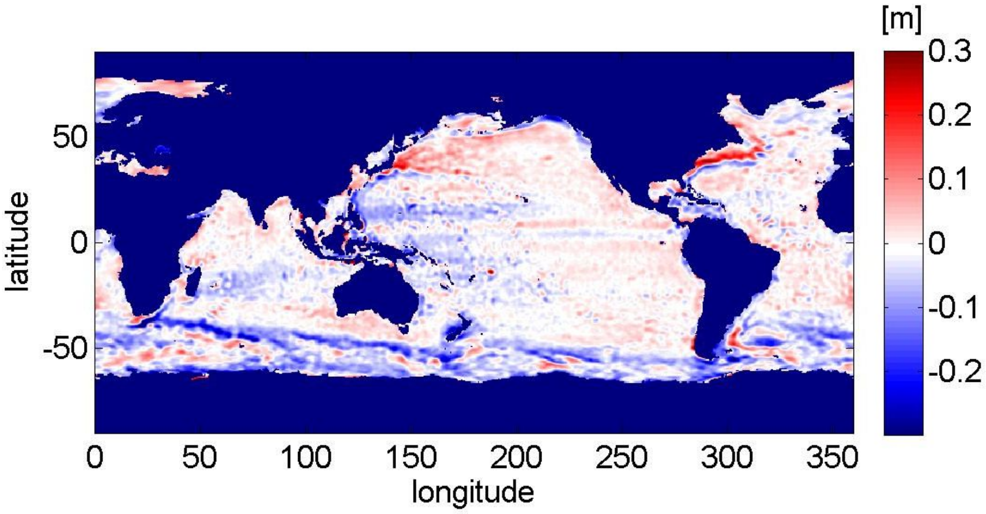

Figure 5.25: Global differences between Maximenko's MDT and the geodetic MDT-GOCE-DTU-120. Units are meters.

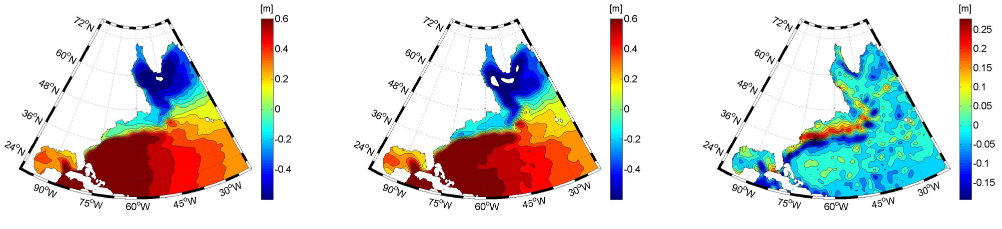

Figure 5.26: The Maximenko's MDT (left panel) and the MDT-GOCE-DTU-120 (middle panel) in the area of the Gulf current. The differences are shown in the right panel.

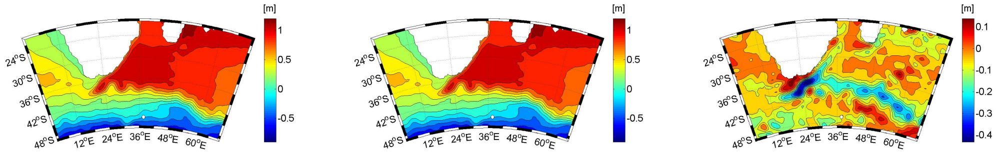

Figure 5.27: The Maximenko's MDT (left panel) and the MDT-GOCE-DTU-120 (middle panel) in the area of the Agulhas current. The differences are shown in the right panel.

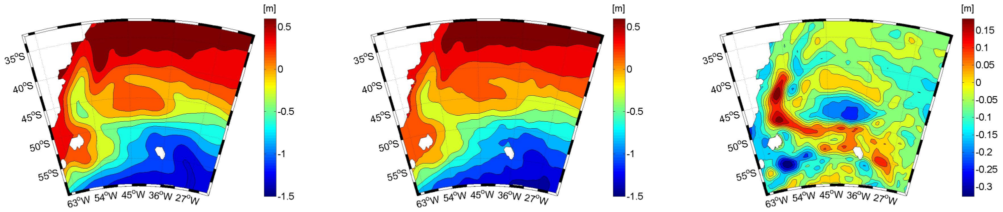

Figure 5.28: The Maximenko's MDT (left panel) and the MDT-GOCE-DTU-120 (middle panel) in the area of the Malvinas current. The differences are shown in the right panel.

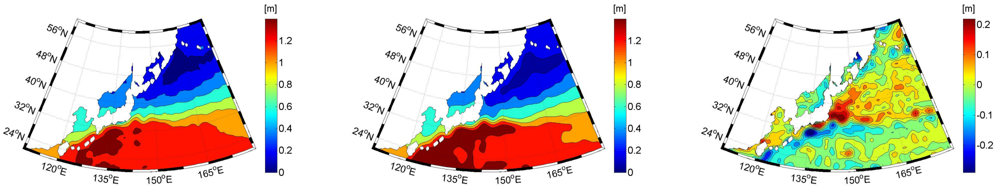

Figure 5.29: The Maximenko's MDT (left panel) and the MDT-GOCE-DTU-120 (middle panel) in the area of the Kuroshio current. The differences are shown in the right panel.

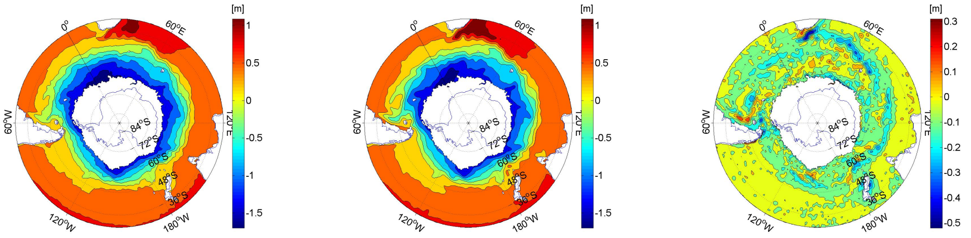

Figure 5.30: The Maximenko's MDT (left panel) and the MDT-GOCE-DTU-120 (middle panel) in the area of the ACC current. The differences are shown in the right panel.

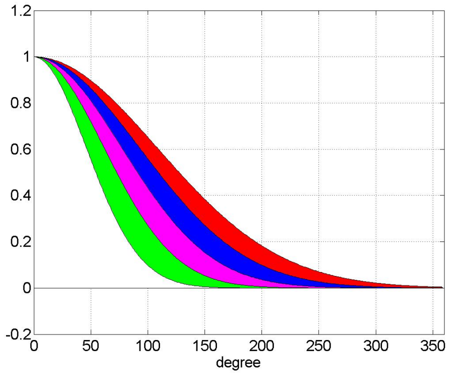

Figure 5.31: Four bandwidths are considered. Green = from $L = 90$ to $L = 120$, magenta = from $L = 120$ to $L = 150$, blue = from $L = 150$ to $L = 180$ and red = from $L = 180$ to $L = 210$.

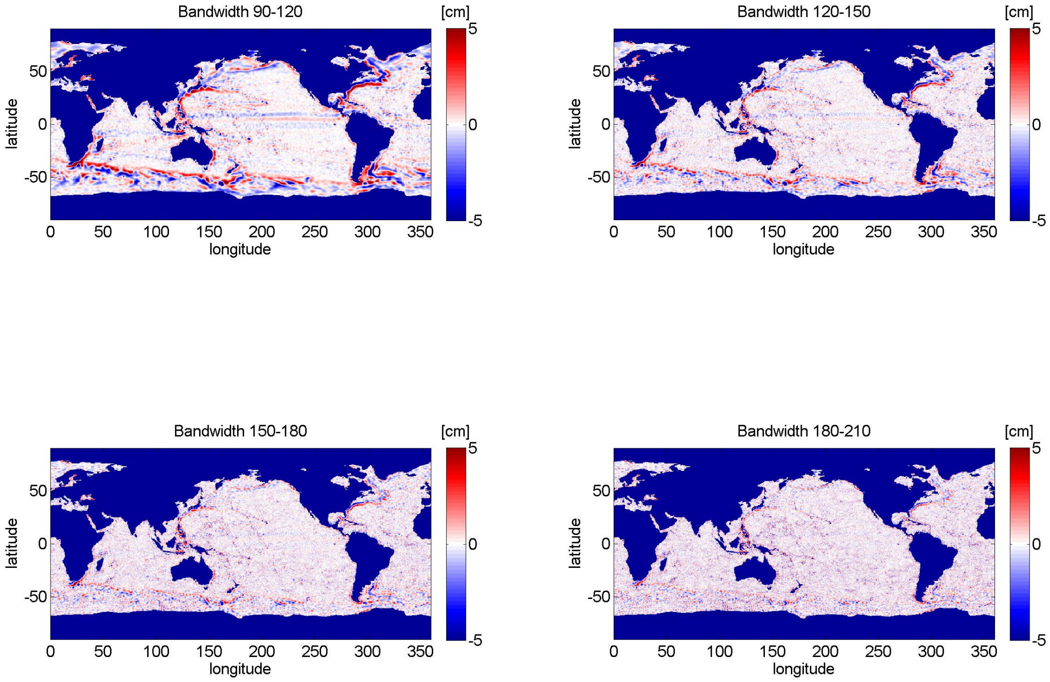

Figure 5.32: Global MDT-GOCE-DTU in different bandwidths. Units are centimeters.

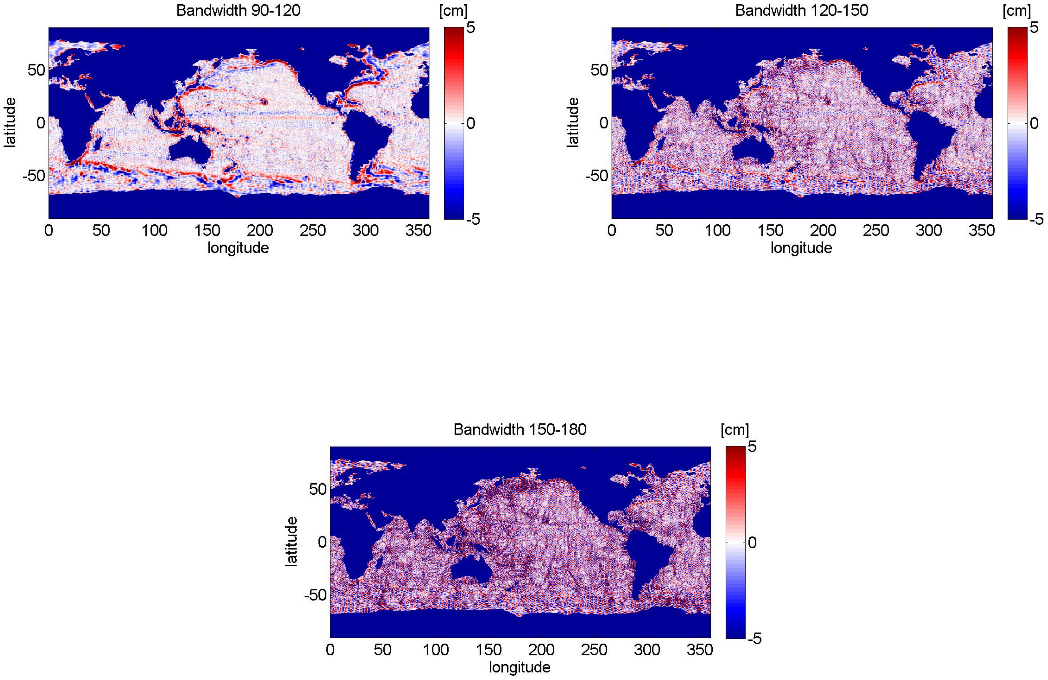

Figure 5.33: Global MDT-GRACE-DTU in different bandwidths. Units are centimeters.

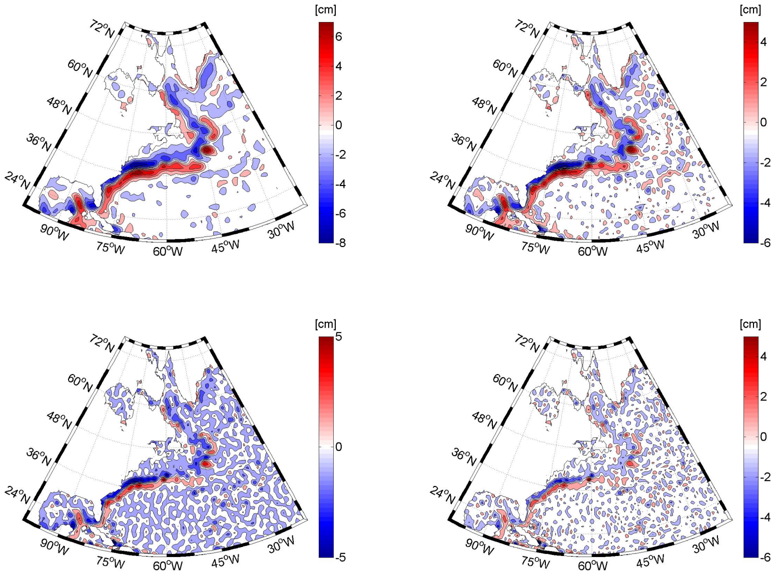

Figure 5.34: MDT-GOCE-DTU in different bandwidths in the Gulf current area. Units are centimeters.

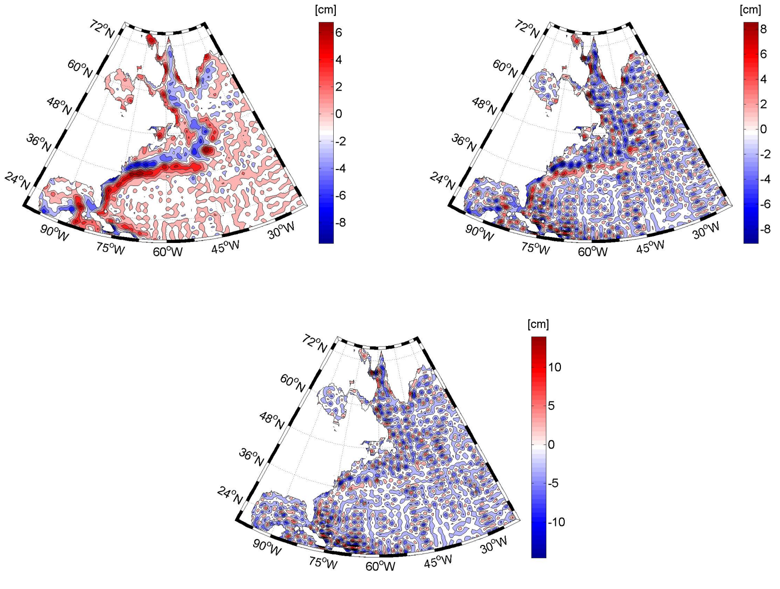

Figure 5.35: MDT-GRACE-DTU in different bandwidths in the Gulf current area. Units are centimeters.

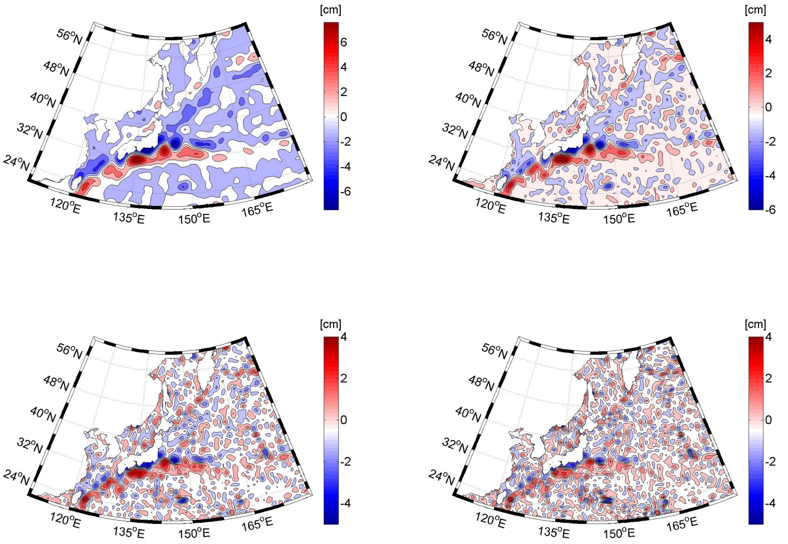

Figure 5.36: MDT-GOCE-DTU in different bandwidths in the Kuroshio current area. Units are centimeters.

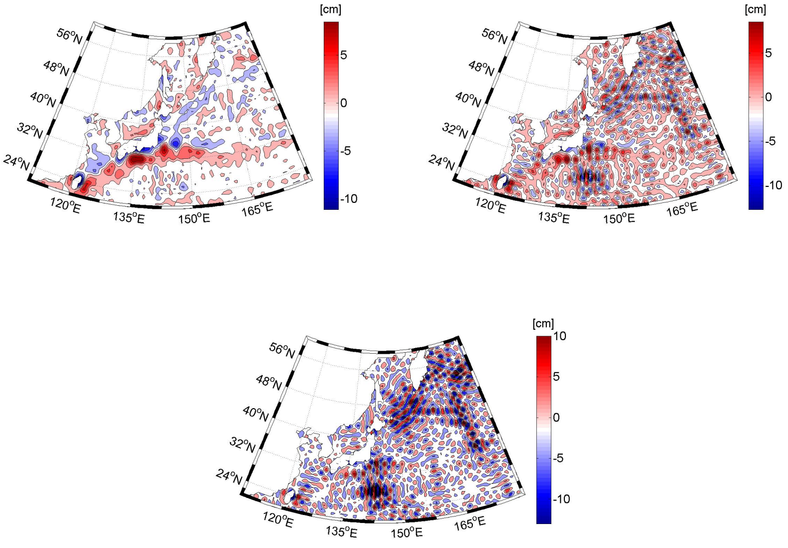

Figure 5.37: MDT-GRACE-DTU in different bandwidths in the Kuroshio current area. Units are centimeters.

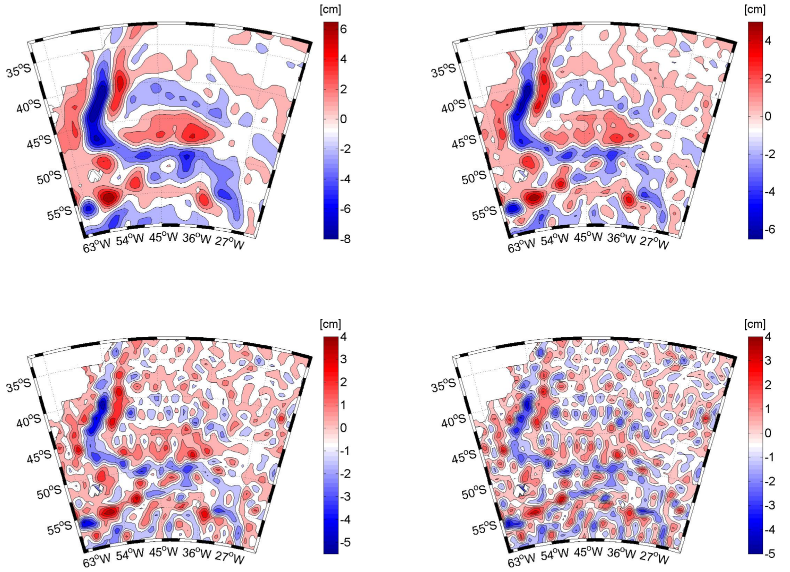

Figure 5.38: MDT-GOCE-DTU in different bandwidths in the Malvinas current area. Units are centimeters.

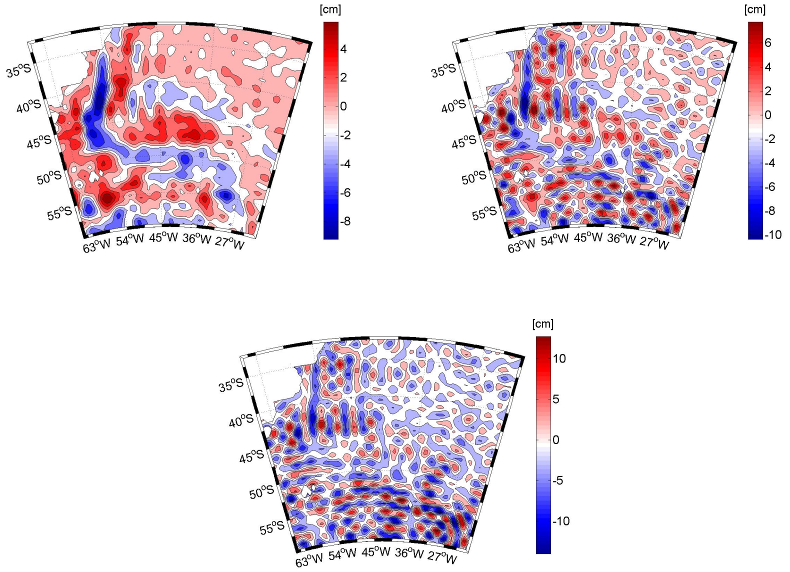

Figure 5.39: MDT-GRACE-DTU in different bandwidths in the Malvinas current area. Units are centimeters.

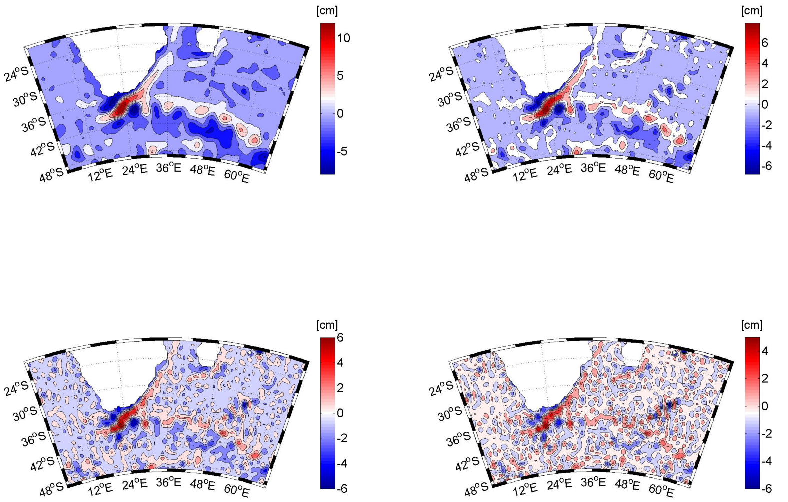

Figure 5.40: MDT-GOCE-DTU in different bandwidths in the Agulhas current area. Units are centimeters.

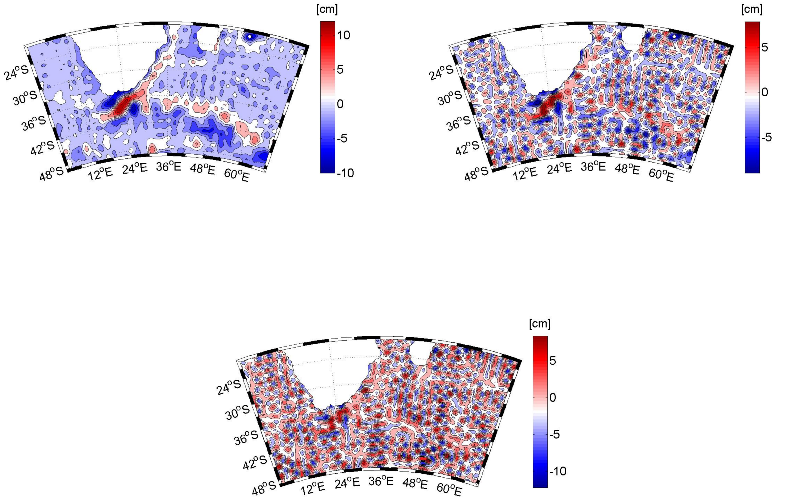

Figure 5.41: MDT-GRACE-DTU in different bandwidths in the Agulhas current area. Units are centimeters.

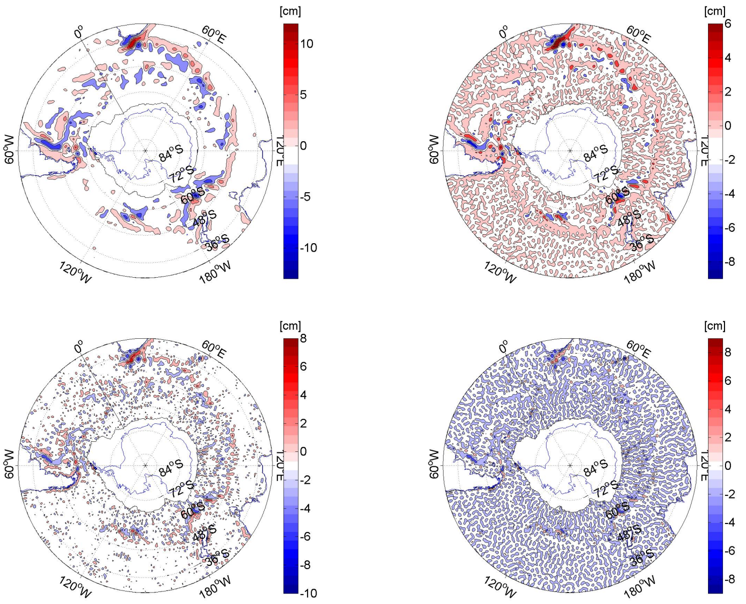

Figure 5.42: MDT-GOCE-DTU in different bandwidths in the ACC current area. Units are centimeters.

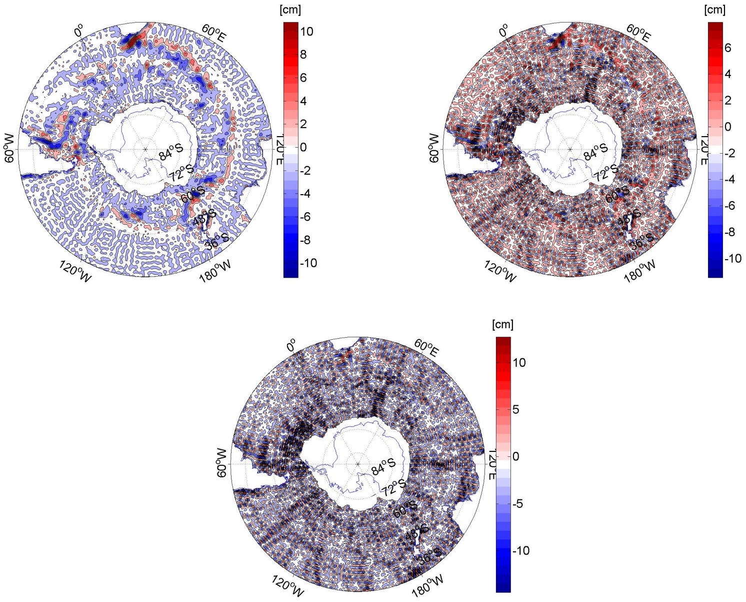

Figure 5.43: MDT-GRACE-DTU in different bandwidths in the ACC current area. Units are centimeters.

Chapter 6

Geostrophic velocities

Once a model of geodetic MDT is available it is only a small step to derive geostrophic surface velocities from it. As will be shown, the strength of the velocity field is proportional to the slope of the MDT and its direction is parallel to the contour lines of the MDT. In other words, geostrophic ocean flow follows the contour lines, in clockwise direction on the Northern hemisphere (and counter clockwise if MDT is negative) and counter clockwise on the Southern hemisphere (and clockwise if MDT is negative). The geostrophic velocities are a result of the balance between the pressure differences due to ocean topography and Coriolis force, as described in any textbook of physical oceanography. They are also the necessary boundary condition at the ocean surface for the computation of ocean velocities at depth from temperature and salinity. They replace the "old" and very inaccurate assumption of a "depth of no motion". We will show how geostrophic velocities can be represented as spherical harmonic vector field with horizontal components u and v. The fact that the velocity field is proportional to the slope of the MDT (its surface derivative) makes it especially sensitive to the highest degrees and orders of the spherical harmonic representation. In other words, the high spatial resolution of GOCE is even more important for the computation of the velocity field than for the MDT itself. Geostrophic velocities can be compared (validated) with ocean surface velocities as derived from drifter data. However, the comparison is not straightforward, for the latter are composed of the sum of the geostrophic and wind driven part. Furthermore, drifter data are sampled highly unevenly, both in space and time.

6.1 Equations of motion

According with the second law of Newton, the acceleration of a particle is proportional to the sum of the forces acting on the particle.

The forces which are acting on a fluid are the pressure gradient, Coriolis, gravity and frictional forces. In vector notation the equation of motion (as derived in Pond & Pickard (1983)), for a rotating fluid becomes:

$$\frac{dV}{dt} = -2\Omega \times V - \frac{\nabla p}{\rho} + g + F \tag{6.1}$$

where

V = total velocity with components (u, v, w)
Ω = angular velocity of the earth
g = gravity acceleration
p = pressure field
ρ = water density
F = frictional forces.

The first term of the right hand side $(-2\Omega \times V)$ is the Coriolis acceleration, the second is the pressure term $(\frac{\nabla p}{\rho})$ and the last describes the frictional forces. Eq. (6.1) can be rewritten in component form, using Cartesian coordinates in a system defined in a point $P = (\vartheta, \lambda, h)$ such that the (x, y) plane defines the local horizon, thus there is no gravitational acceleration in horizontal direction. The direction of the negative z-axis coincides with the direction of g. The x-axis is oriented in East direction and the y-axis in North direction. The origin of the coordinate frame is at the sea surface. Eq. (6.1) in local Cartesian coordinates becomes:

$$\begin{aligned} \dot{u} + 2\Omega(w \sin\vartheta - v\cos\vartheta) &= -\frac{1}{\rho}\frac{\partial p}{\partial x} + F_1 \\ \dot{v} + 2\Omega(u\cos\vartheta) &= -\frac{1}{\rho}\frac{\partial p}{\partial y} + F_2 \\ \dot{w} - 2\Omega(u\sin\vartheta) &= -\frac{1}{\rho}\frac{\partial p}{\partial z} - g + F_3 \end{aligned} \tag{6.2}$$

where

(u, v, w) velocities in the Cartesian coordinate system
$(\dot{u}, \dot{v}, \dot{w})$ accelerations, i.e. the total derivatives of the velocity components, in the Cartesian coordinate system.

These equations are called "equations of motion" for fluids. They are applicable at any depth in the ocean. At the sea surface the effects of wind at the air/sea interface are included in the F_i terms. Every solution of the Eq. (6.2) must also satisfy the equation of continuity:

$$\frac{\partial u}{\partial x} + \frac{\partial v}{\partial y} + \frac{\partial w}{\partial z} = 0 \ , \tag{6.3}$$

which is derived from the assumption of the incompressibility of water.

The equations of motion in horizontal direction can be simplified if we consider the vertical velocity w and the Coriolis term $2\Omega w \sin\vartheta$ (at a co-latitude $\vartheta = 45°$ it is in the order of 10^{-8}) in the first of the Eq. (6.2) negligible. This simplification is justified because a typical value for w is in the order of 10^{-4} m/s, while the horizontal velocities are in the order of 0.1 m/s, (Pond & Pickard, 1983). The other two Coriolis terms containing $2\Omega\cos\vartheta$ cannot be neglected. After these simplifications, (Pond & Pickard, 1983) we get:

$$\begin{aligned} \dot{u} - fv &= -\frac{1}{\rho}\frac{\partial p}{\partial x} + F_1 \\ \dot{v} + fu &= -\frac{1}{\rho}\frac{\partial p}{\partial y} + F_2 \end{aligned} \tag{6.4}$$

where $f = 2\Omega \cos\vartheta$ is the Coriolis term.

Under the assumption of a steady-state system ($\dot{u}, \dot{v}, \dot{w} = 0$), and assuming the absence of frictional forces, a multiplication of the Eq. (6.4) by ρ and differentiation with respect to z yields:

$$\begin{aligned} -f\frac{\partial \rho v}{\partial z} &= -\frac{\partial}{\partial z}\left(\frac{\partial p}{\partial x}\right) \\ f\frac{\partial \rho u}{\partial z} &= -\frac{\partial}{\partial z}\left(\frac{\partial p}{\partial y}\right) . \end{aligned} \tag{6.5}$$

Under the above assumptions and considering that the Coriolis term is much smaller than the pressure and gravity terms, the third equation of (6.2) becomes:

$$\frac{\partial p}{\partial z} = -g\rho \ . \tag{6.6}$$

Eq. (6.6) is the equation of hydrostatic balance.

Changing the order of differentiation in (6.5) and application of (6.6) we get:

$$\begin{aligned} -f\frac{\partial \rho v}{\partial z} &= -\frac{\partial}{\partial x}\frac{\partial p}{\partial z} = +\frac{\partial (g\rho)}{\partial x} = g\frac{\partial \rho}{\partial x} \\ f\frac{\partial \rho u}{\partial z} &= -\frac{\partial}{\partial y}\frac{\partial p}{\partial z} = +\frac{\partial (g\rho)}{\partial y} = g\frac{\partial \rho}{\partial y} \ . \end{aligned} \tag{6.7}$$

The "thermal wind equations" (6.7) can be integrated in vertical direction, resulting in:

$$\begin{aligned} \rho v &= -\frac{g}{f}\int_{z_0}^{z} \frac{\partial \rho}{\partial x} dz + v_0 \\ \rho u &= +\frac{g}{f}\int_{z_0}^{z} \frac{\partial \rho}{\partial y} dz + u_0 \ . \end{aligned} \tag{6.8}$$

The depth z_0 is called the reference depth and the integration constants u_0 and v_0 are the reference level velocities. The thermal wind equations show that only a relative velocity can be determined from the density field. To determine absolute values, a level of known motion has to be assumed. Apart from these integration constants, the flow is calculable from shipborne measurements providing temperature and salinity as function of depth alone. If we observe the distribution of salinity and temperature as a function of depth in the ocean, we can calculate p from the hydrostatic equation and use it to find u and v.

The total pressure at a point below the water surface is equal to the sum of the atmospheric pressure and the pressure due to the weight of the fluid above the point. In most dynamical oceanography calculations the atmospheric pressure term is neglected and only the pressure due to the weight of water (hydrostatic term) is used. Therefore we can vertically integrate the hydrostatic balance (6.6) from the mean sea level. The integration can be split up into two terms, one from the MSS to the geoid ($z = 0$) and the second from the geoid to an arbitrary depth z:

$$p = \int_{z}^{H} g\rho dz = g\rho H + \int_{z}^{0} g\rho dz \tag{6.9}$$

H is the elevation of the sea surface with respect to the geoid, that is the MDT. The first term of the right member of (6.9) depends on the sea surface, while the second is a function of depth. Differentiating with respect to x and y we get:

$$\begin{aligned} \frac{\partial p}{\partial x} &= g\rho\frac{\partial H}{\partial x} + g\int_z^0 \frac{\partial \rho}{\partial x}dz \\ \frac{\partial p}{\partial y} &= g\rho\frac{\partial H}{\partial y} + g\int_z^0 \frac{\partial \rho}{\partial y}dz \end{aligned} \tag{6.10}$$

To obtain the velocities in the local horizontal plane at the sea surface, we combine (6.10) with Eq. (6.4), neglecting $(\dot{u}, \dot{v}, F_1, F_2)$:

$$\begin{aligned} +u_s &= -\frac{g}{f}\frac{\partial H}{\partial y} \\ -v_s &= -\frac{g}{f}\frac{\partial H}{\partial x} \end{aligned} \tag{6.11}$$

The surface velocity u_s is the velocity in longitude (or east) direction, the velocity v_s is in latitude (or north) direction. The formulas of the surface water velocities in the spherical coordinates system (ϑ, λ) become, (observing that $dy = -Rd\vartheta$ and $dx = R\sin\vartheta d\lambda$):

$$\begin{aligned} u_s &= -\frac{g}{f}\frac{1}{R}\frac{\partial H}{\partial \vartheta} \\ v_s &= \frac{g}{f}\frac{1}{R\sin\vartheta}\frac{\partial H}{\partial \lambda} \end{aligned} \tag{6.12}$$

where R is the radius of a spherical earth.

Equations (6.11) and (6.12) are the geostrophic equations. They are only an approximation, because friction is neglected, but they permit us to determine the components of the geostrophic velocity of the surface currents of the ocean from the slope of the mean sea surface.

6.2 Geodetic determination of the geostrophic flow

The surface velocities can be computed from the mean dynamic topography in two ways:

1. using the spatial discrete gradient (DG), computed at grid points;
2. using the spherical harmonic (SH) expansion of the surface velocities (the derivatives are computed analytically and evaluated in the grid points).

The two methods are essentially equivalent, but the spherical harmonic representation of the geostrophic velocities allows (i) to eliminate the approximation due to the discretization of the derivatives and (ii), more importantly, the analysis of spectral bands.

Differentiating the Eq. (5.11) with respect to ϑ and λ, see Elema (1993), we have:

$$\begin{aligned} \frac{\partial H}{\partial \vartheta} &= \sum_{\ell=0}^{L} \sum_{m=0}^{\ell} \left(C_{\ell m}^{H} \cos m\lambda_P + S_{\ell m}^{H} \sin m\lambda_P \right) P'_{\ell m}(\cos\vartheta_P) \\ \frac{\partial H}{\partial \lambda} &= \sum_{\ell=0}^{L} \sum_{m=0}^{\ell} m \left(-C_{\ell m}^{H} \sin m\lambda_P + S_{\ell m}^{H} \cos m\lambda_P \right) P_{\ell m}(\cos\vartheta_P) \end{aligned} \tag{6.13}$$

Combining Eq. (6.13) with the geostrophic equations (6.12) we obtain:

$$\begin{aligned} u_s(\vartheta_P, \lambda_P) &= -\frac{g}{fR} \sum_{\ell=0}^{L} \sum_{m=0}^{\ell} \left(C_{\ell m}^{H} \cos m\lambda_P + S_{\ell m}^{H} \sin m\lambda_P \right) P'_{\ell m}(\cos\vartheta_P) \\ v_s(\vartheta_P, \lambda_P) &= \frac{g}{f} \frac{1}{R \sin\vartheta_P} \sum_{L}^{\ell=0} \sum_{m=0}^{\ell} m \left(-C_{\ell m}^{H} \sin m\lambda_P + S_{\ell m}^{H} \cos m\lambda_P \right) P_{\ell m}(\cos\vartheta_P) \end{aligned} \tag{6.14}$$

Since the step from MDT to surface velocities is comparable to taking the surface gradient, high degrees and orders of the spherical harmonic expansion are amplified. This is the same as saying, short scales features are emphasized.

Figs. 6.1 to Fig. 6.4 show the result of the calculation of the surface currents in a grid $30' \times 30'$ using the MDT-GOCE-DTU and applying Butterworth filters up d/o 120, 150, 180 and 210. As the truncation of the harmonic expansion increases, the patterns show more and more detail because the shorter scales become more pronounced. At the equator it is not possible to compute the current direction with the geostrophic equations, because the Coriolis term is zero there.

Considering selected regions the results are more clear.
The major oceanic currents are shown in the Fig. 6.5 to Fig. 6.18. The filtering (Butterworth) is taken up d/o 180. The Gulf current (Fig. 6.5) is well pronounced, not only along the Western coasts of North America, but also in the Gulf of Mexico. The Labrador current can also be identified. The directions of both currents are correct. The Agulhas Current (Fig. 6.8) is well identified by our MDT. In particular, it shows its retroflection and its flow back into the Indian Ocean. Furthermore, the Malvinas Current as well as the South Atlantic current (Fig. 6.11) are visible. The route of the Kuroshio current (Fig. 6.14) is well defined, while the Oyashio current does not appear. Finally, the ACC current (Fig. 6.17) is almost entirely visible.

Fig. 6.7, 6.10, 6.13, 6.16 and 6.19 show the comparison between the geostrophic current from GOCE and from Maximenko's MDT.

The Gulf current from GOCE (left panel of Fig. 6.7) appears stronger and better outlined than current from Maximenko (right panel of Fig. 6.7). The maximum current speed detected by GOCE is 80 cm/s and it is 60 cm/s from Maximenko. Furthermore the Labrador current is weak in both cases (cm/s) but better recognizable in the results from GOCE.

Moreover the Agulhas current from GOCE (left panel of Fig. 6.10) is better outlined. With GOCE the speed of the current reaches 75 cm/s, while with Maximenko (right panel of Fig. 6.10) the maximum is around 55 cm/s. We observe that the East Madagascar current (one of the more important sources for the Agulhas Current) is visible only with GOCE data. Furthermore some eddies appear between 48° and 60° E around the latitude of 33° S. Anyway it is difficult to correlate these eddies to a real circulation because the eddies may persist for months to years and here we are considering a MDT averaged over 17 years.

Regarding the Malvinas current, the magnitude of the velocities computed with GOCE (left panel of Fig. 6.13) is closer to the empirical values (around 50 cm/s) than the velocities computed with Maximenko (left panel of Fig. 6.13). It seems that the confluence with the Brazil current (around 40° S and 54° S) is easily determinable.

The geostrophic velocities for the Kuroshio region calculated from GOCE (left panel of Fig. 6.16) show the maximum value around 32° N and 135° E. That value is about 80 cm/s. The Kuroshio current computed from Maximenko (right panel of Fig. 6.16) is weaker (maximum around 60 cm/s) along all the path of the current.

Finally also the comparison in all the ACC area (Fig. 6.19) shows that GOCE exhibits more details.

In order to obtain a correct evaluation it is necessary to verify the intensity of all velocities through a comparison of the in-situ measurements. This will be further developed in the following section.

6.3 Drifter data

To validate the geodetic geostrophic velocities a comparison with in-situ measurements is done. The Global Drifter Program of NOAA (National Oceanic and Atmospheric Administration, US) and AOML (Atlantic Oceanographic and Meteorological Laboratory, US) collects Satellite-tracked drifting buoys ("drifter") measurements of upper ocean currents and sea surface temperatures around the world. Drifter locations are estimated from 16-20 satellite fixes per day, per drifter. These raw data are processed applying quality control procedures, and interpolated via kriging to regular six-hour intervals.

At `http://www.aoml.noaa.gov/envids/gld/` it a large set of data from February 1979 to December 2010 is available, covering almost all the sea surface: latitude from 90° to $-74°$ and longitude from $-180°$ to 180°. Two types of data are available: "metadata" contains deployment location and time, time of drogue (sea anchor) loss, date of final transmission for each drifter and "interpolated data" contains the quality-controlled, interpolated drifter observations. Following the description in Grodsky *et al.* (2011), in the Southern Ocean area we exclude all drifters "older" than three months.

In the following 4 areas are considered:

- Gulf current area: $\varphi \in [18°, 70°], \lambda \in [268°, 340°]$;
- Kuroshio current area: $\varphi \in [21°, 61°], \lambda \in [111°, 180°]$;
- Agulhas current area: $\varphi \in [-20°, -50°], \lambda \in [2°, 70°]$;
- Malvinas current area: $\varphi \in [-32°, -60°], \lambda \in [295°, 340°]$.

We consider all the drifter measurements of these areas from 1 January 1993 to 31 December 2009 (that is the same time interval applied for the computation of the DTU10). In Fig. 6.20 the geographical distribution, averaged over each cell of a grid $30' \times 30'$, of the in-situ observation is shown. There are definitely more observations for the Gulf and the Kuroshio currents, comparing with the Agulhas and Malvinas currents. In all four areas the distributions of the measurements is not uniform.

In Fig. 6.21 to Fig. 6.24 the velocities derived from the drifter observations are shown. The velocity extracted from the drifting buoy path includes also the tide currents, the Ekman currents, the inertial currents and other high-frequency a-geostrophic currents. Here we are considering their time average (over 17 years) and their space average (on the grid $30' \times 30'$).

Annual mean sea level can vary considerably from year to year in response to various meteorological and oceanographic forcings. The velocities measured by drifters must be corrected subtracting the altimetric velocity anomaly corresponding to the Mean Sea Level Anomalies (MSLA). This is the so-called synthetic method, see Rio *et al.* (2006). The anomalies are, by definition, the difference between the measurement made at a specific time and the mean value over many years at the same location. An example of the corrections concerning the MSLA is shown in Fig. 6.25. They appear not to be correlated and they affect only the short scales. Therefore we can skip this correction, remembering that our MDT involves spherical harmonics up to d/o 250 (corresponding with the resolution of the GOCE mission), that means scales longer than 80 km.

The sea surface velocity obtained with the drifter measurements contains not only a geostrophic current component but also a-geostrophic components, such as tidal, wind-driven Ekman currents and others. These a-geostrophic currents are absent in the geostrophic data obtained with altimetry observations and make the comparison difficult. Here we are considering a temporal average over 17 years, where we assume that the tidal component has been removed.

More complex is the problem of the Ekman currents. The wind blows across the ocean and moves its waters as a result of its frictional drag on the surface. Frictional effects are indeed small in the interior of the ocean, but they become important at the boundary layer. The layer in which the frictional forces becomes important is called the “Ekman layer”. That layer is at most a few-hundred meters thick, which is thin compared with the depth of the water in the deep ocean.

Because of the deflection by the Coriolis force, the Ekman transport is not in the direction of the wind, but it is 90° to the right on the Northern Hemisphere and 90° toward the left on the Southern Hemisphere. The Ekman component driven by local wind needs to be estimated using wind data. It would not be averaged out by temporal smoothing since the forcing winds include a longer time-scale variation component. An example of the estimation of the wind-driven (Ekman) currents is described in Siegismund (2013).

In this study we will not analyze the problem of the determination of the Ekman velocities.
To estimate the order of magnitude of the Ekman corrections (as in Fig. 6.26) we consider the example reported at `http://www.aoml.noaa.gov/phod/dac/drifter-climatology.html`, (Lumpkin & Garraffo, 2005). Here the Ekman currents are estimated using wind stress data and the local Coriolis parameter (Ralph & Niiler, 1999).

If the “geodetic” geostrophic velocities have not to be validated by drifter data, the problem can be posed differently. A possible way to estimate the Ekman component of the surface currents consists of the use of the geostrophic velocities computed from satellite altimetry and subtracting them from surface currents as given by drifter trajectories to estimate a-geostrophic currents, see Rio & Hernandez (2003).

6.4 Surface velocities comparison

In this section we compare the geostrophic velocities from the MDT-GOCE-DTU-180 and the estimated geostrophic velocities from the drifter measurements. We consider the four areas described in the previous section.

- **Gulf**: the correlations are very strong (> 0.7) not only in the area around the Gulf current, but also along the Labrador current. The correlations are high for both components, see Fig. 6.27.
  Looking at the differences, see Fig. 6.28 we observe that the largest differences are along the coasts of Cuba, while in open ocean they are below 10 cm/s. The RMS of the differences is equal to 12.64 cm/s.
  When we subtract the Ekman currents (as estimated in (Lumpkin & Garraffo, 2005)) the RMS drops only to 11.70 cm/s, see Table 6.1.
- **Kuroshio**: in this area the correlations are also strong, Fig. 6.29, even though the Eastward component is slightly inferior (0.6). The largest differences are along the Chinese coasts Fig. 6.30. When the Ekman corrections are applied, the statistics do not improve but they slightly deteriorate. This probably means that the Ekman corrections in this area are not sufficiently accurate.
- **Agulhas**: also in this case the correlations between the Eastward components are lower than the correlations between the Northward components, see Fig. 6.31. The area south of the African continent (this is part of ACC) shows a high correlation. The differences show, see Fig. 6.32, a discrepancy along the Eastern African and Madagascarian coasts; everywhere else the differences are considerably lower. In this area the Ekman corrections are improving the results for the Eastward component but not for the Northward one, Table 6.1.
- **Malvinas**: in this area the correlations are high everywhere except for the Northward component where they are slightly inferior, Fig. 6.33. This area shows the lowest differences Fig. 6.34, as seen also from their RMS. Also in this case the Ekman corrections seem to improve the results for the Eastward component but not the Northward one, Table 6.1.

	$\mathbf{m}(u_s - u_d)$	$\mathbf{RMS}(u_s - u_d)$	$\mathbf{m}(v_s - v_d)$	$\mathbf{RMS}(v_s - v_d)$	$\mathbf{m}(\Delta V)$	$\mathbf{RMS}(\Delta V)$
Gulf	0.80 (0.88)	8.88 (7.91)	2.03 (1.83)	9.00 (8.61)	7.82 (7.54)	12.64 (11.70)
Kuroshio	1.03 (0.98)	9.08 (8.33)	2.00 (2.29)	8.69 (8.71)	8.48 (8.17)	12.56 (12.06)
Agulhas	1.71 (1.29)	9.07 (7.06)	0.84 (-1.52)	6.00 (7.27)	9.34 (8.89)	10.87 (10.13)
Malvinas	3.77 (2.09)	6.02 (5.06)	1.30 (-3.86)	4.70 (5.86)	6.65 (6.78)	7.64 (7.74)

Table 6.1: RMS of the difference between the geostrophic velocities from the MDT-GOCE-DTU-180 and the estimated geostrophic velocities from the drifter measurements. In parenthesis the statistics when the Ekman correction is considered. Units are cm/s.

6.5 Bandwidth analysis

The spherical harmonic representation Eq. (6.14) of the geostrophic velocities allows analyzing the information contained in different spectral bands. Like in section 5.4, the bandwidth analysis target is to show which is the contribution of GOCE in the determination of the highest harmonic components of the geostrophic velocities. For the comparison the velocities computed using only GRACE data are considered.

In the following we consider:

MDT-GRACE-DTU : computed using the gravity model ITG-Grace2010

MDT-GOCE-DTU : computed using the gravity model TUMGOCEext.

As in the case of the MDT, the appropriate bandwidth analysis is obtained considering a Gauss filter. We consider the four bandwidths shown in Fig. 5.31. In Fig. 6.35 and Fig. 6.36, the bandwidths of geostrophic velocities from MDT-GOCE-DTU and MDT-GRACE-DTU are shown. In the first bandwidth (from d/o 90 to d/o 120) the signal from GRACE is noisier than the signal from GOCE. However the major currents can be clearly identified. In particular the anomalous features are visible in the South Pacific and in the Indian Ocean. The signal from GOCE is clear up d/o 180.

We consider four regional areas, corresponding to the major oceanic currents: the Gulf current (Fig. 6.37 and Fig. 6.38), the Kuroshio current (Fig. 6.39 and Fig. 6.40), the Agulhas current (Fig. 6.41 and Fig. 6.42) and the Malvinas current (Fig. 6.43 and Fig. 6.44).

Regarding the Gulf and the Agulhas currents, with GOCE a signal contribution to the current can be identified throughout all bandwidths. Such contribution is not affected by noise, and reaches 10 cm/s even in the spectral band between degree and order 180 and 210. This, however, does not happen with GRACE. Using GRACE, any significant ocean feature is only visible between degree and order 90 and 120. Regarding the Malvinas and Kuroshio currents, GOCE identifies a perceptible signal up to d/o 180. In the last bandwidth (180-210) the noise appears to prevail. In this case too, with GRACE something is identifiable only between degree and order 90 and 120.

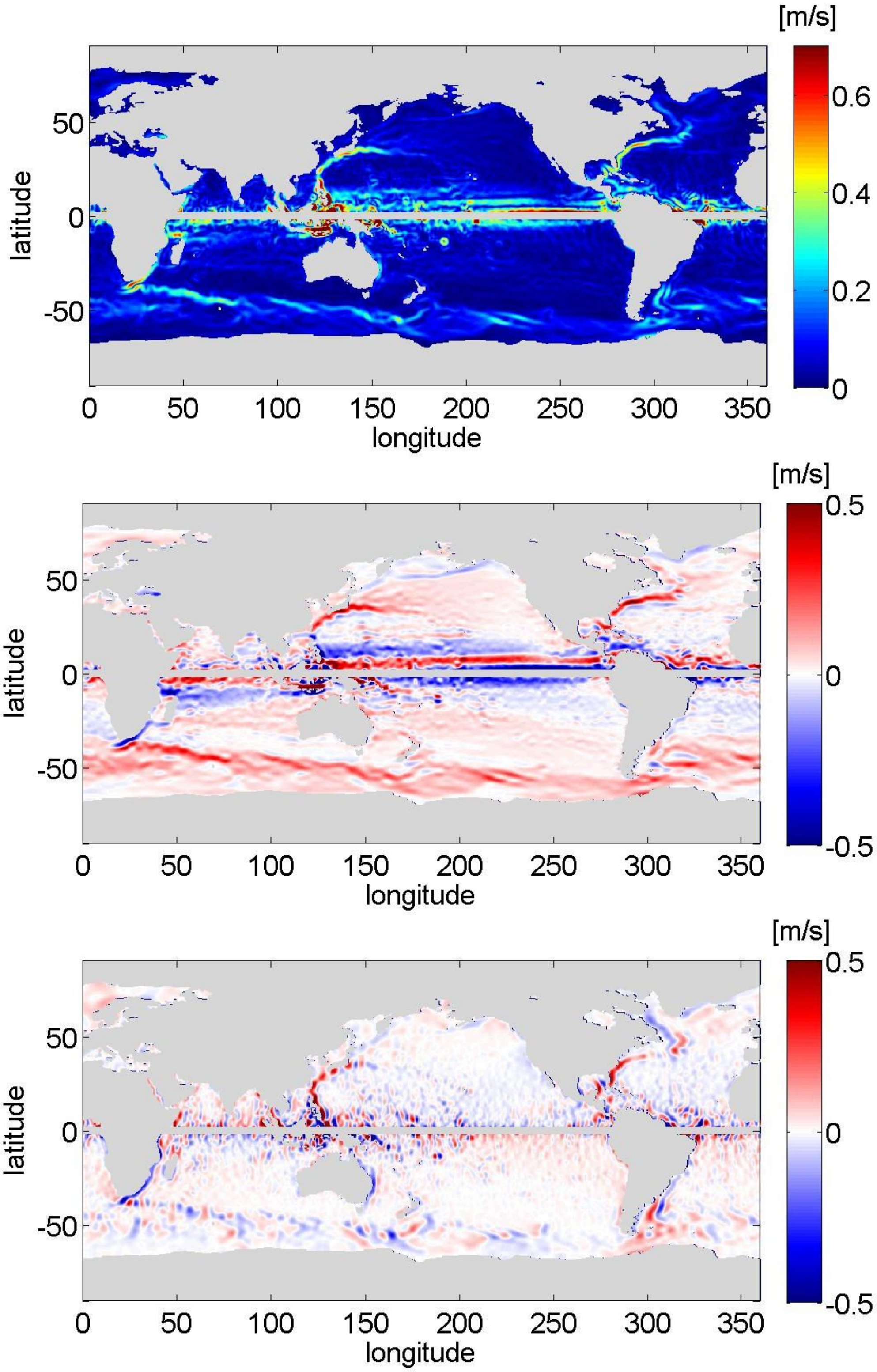

Figure 6.1: Magnitude (upper panel) of the geostrophic velocities computed by MDT-GOCE-DTU-120. The East component is shown in the middle panel and the North component in the bottom one. Units are m/s.

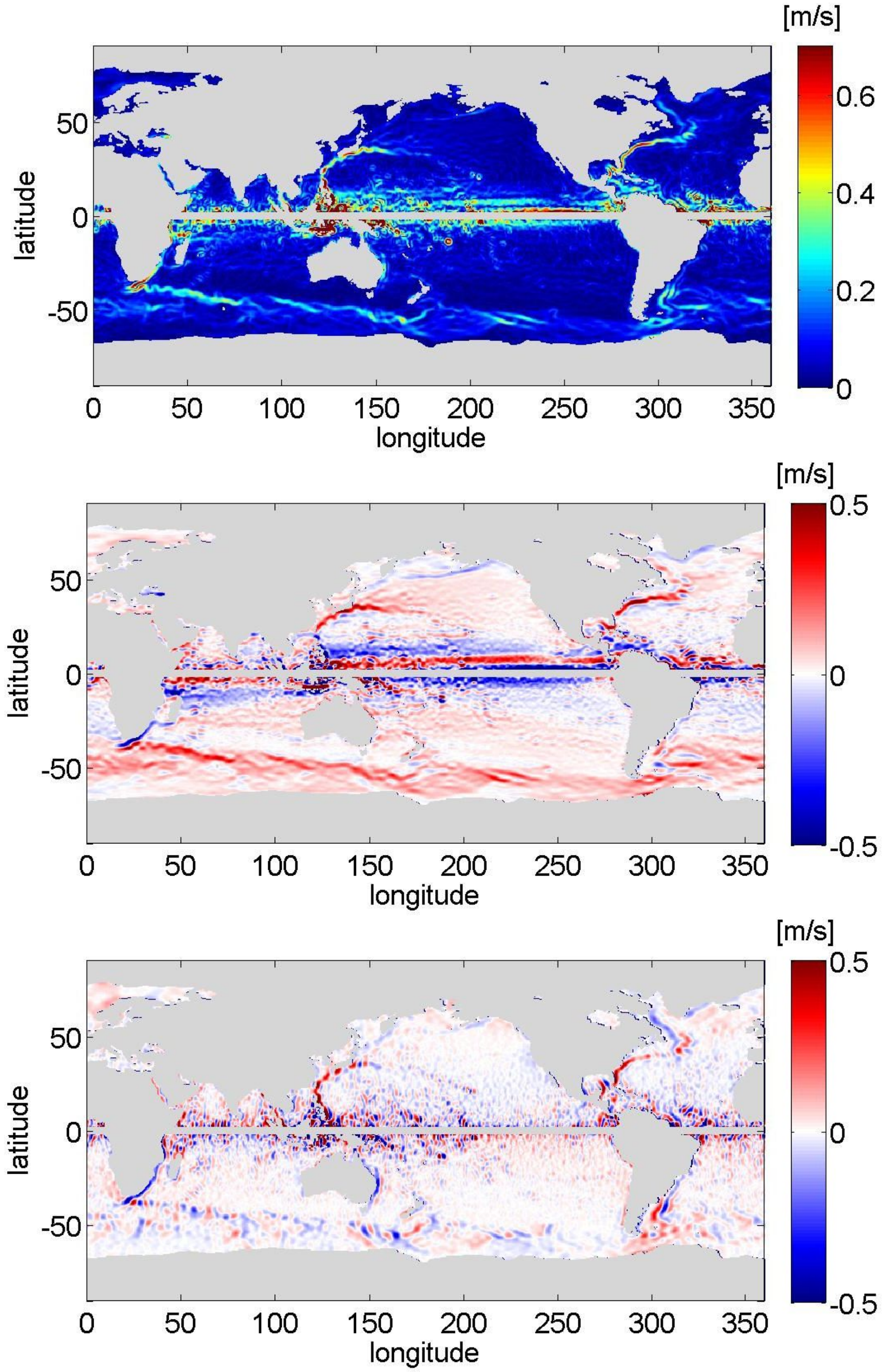

Figure 6.2: Magnitude (upper panel) of the geostrophic velocities computed by MDT-GOCE-DTU-150. The East component is shown in the middle panel and the North component in the bottom one. Units are m/s.

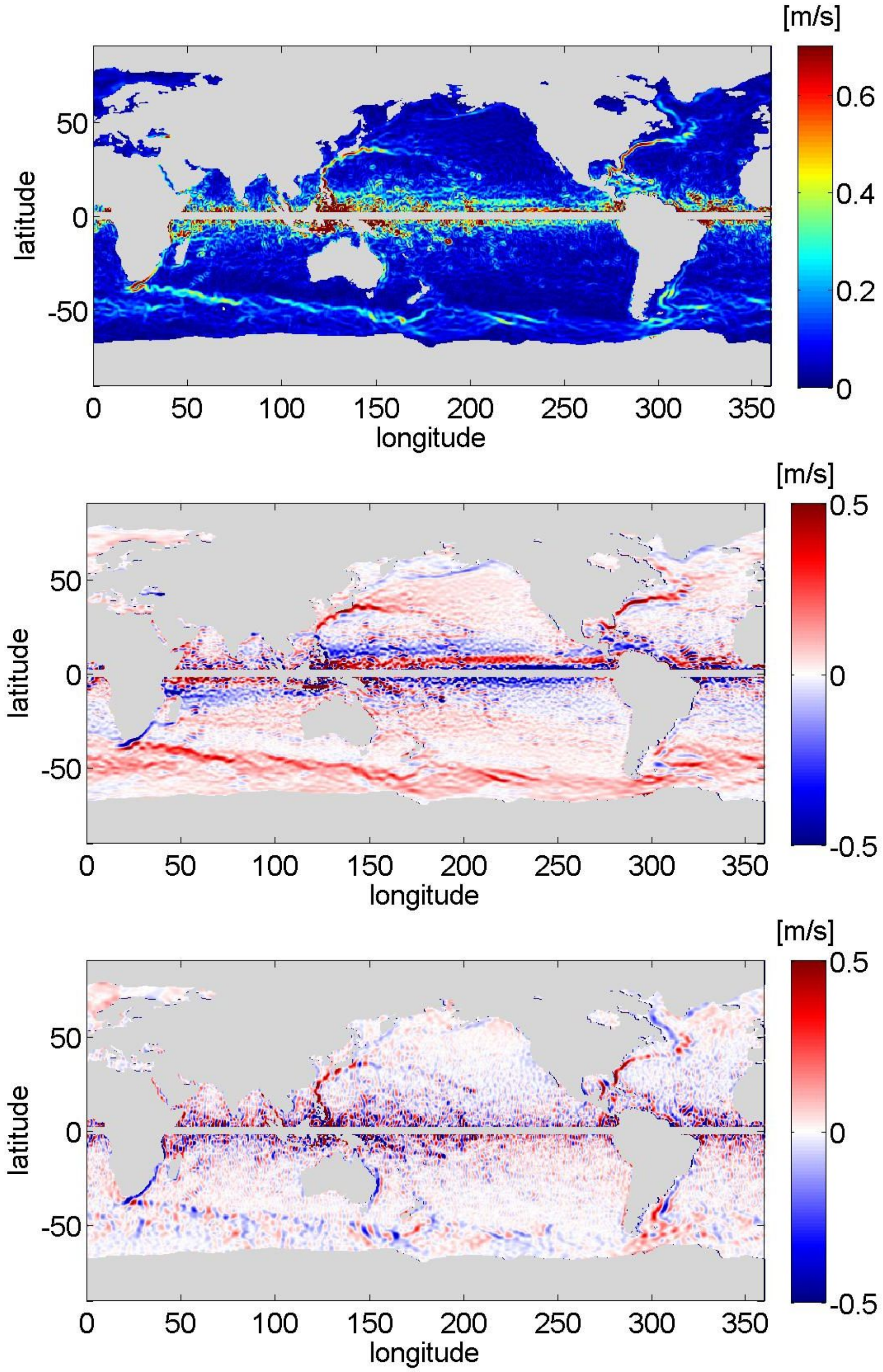

Figure 6.3: Magnitude (upper panel) of the geostrophic velocities computed by MDT-GOCE-DTU-180. The East component is shown in the middle panel and the North component in the bottom one. Units are m/s.

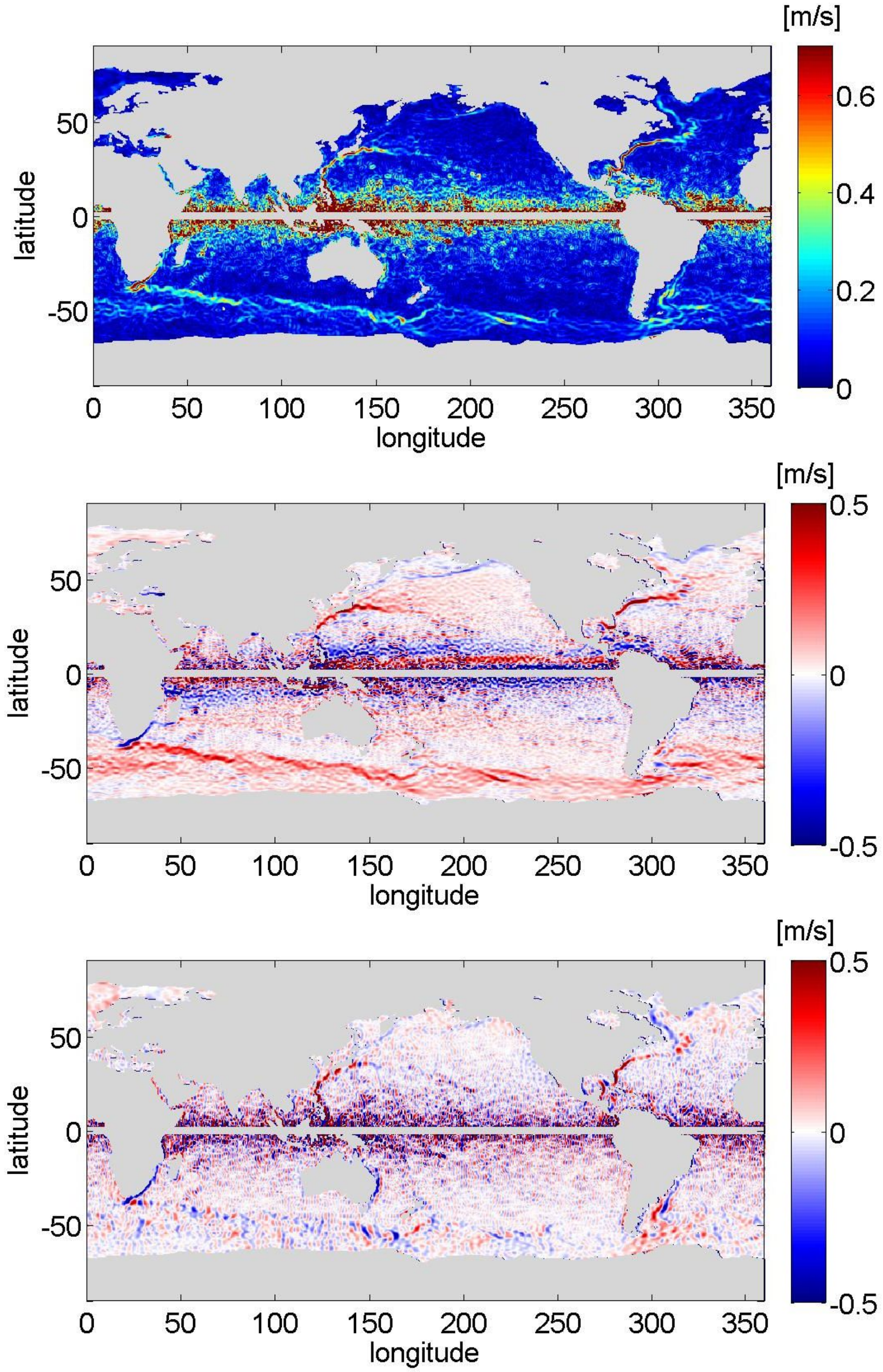

Figure 6.4: Magnitude (upper panel) of the geostrophic velocities computed by MDT-GOCE-DTU-210. The East component is shown in the middle panel and the North component in the bottom one. Units are m/s.

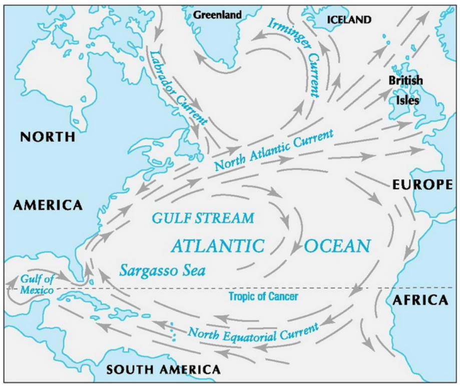

Figure 6.5: The Gulf Stream is the western boundary current of the North Atlantic subtropical gyre. It transports significant amount of warm water. The Labrador Current is the "southward" flowing component of the North Atlantic subpolar gyre. It transports cold waters into the warmer Gulf Stream ring and meander region. Figure from `http://world-geography.org/287-gulf-stream.html`.

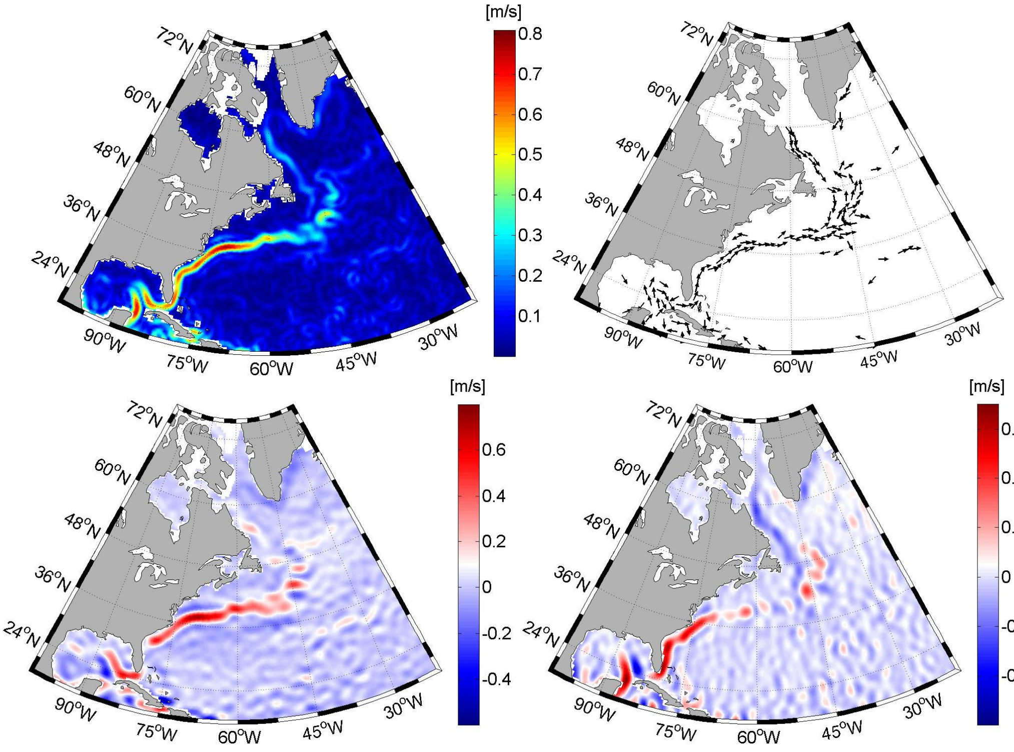

Figure 6.6: The geostrophic velocities in the area of the Gulf current computed using MDT-GOCE-DTU-180. Upper left: magnitude, upper right: directions, lower left: East component, lower right: North component. Units are m/s.

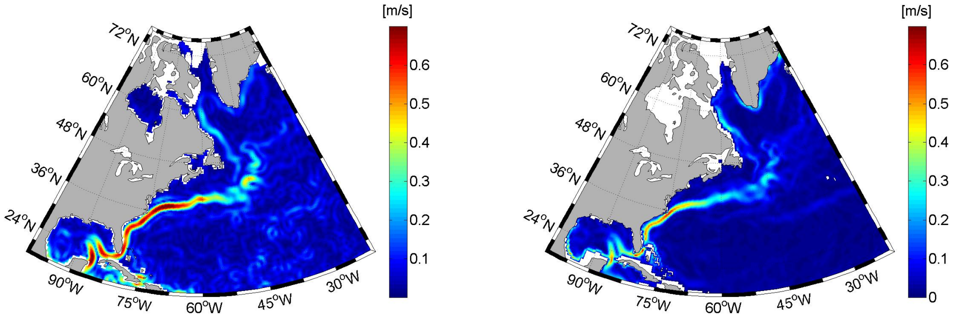

Figure 6.7: Magnitude of the geostrophic velocities from MDT of Maximenko (right panel) and from MDT-GOCE-DTU-180 (left panel) in the area of the Gulf current. Units are m/s.

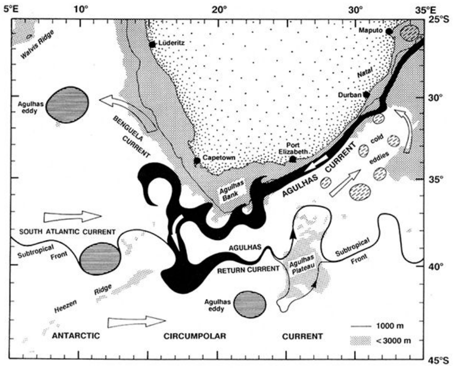

Figure 6.8: The Agulhas Current is the western boundary current of the South Indian Ocean. It flows down the east coast of Africa bringing warm water poleward. On average, the Agulhas current retroflects and returns eastward with part of the flow recirculating in the counter-clockwise flowing subtropical gyre and part of the flow feeding the Antarctic Circumpolar Current. Figure from `http://essayweb.net/geology/quicknotes/ocean_currents.shtml`.

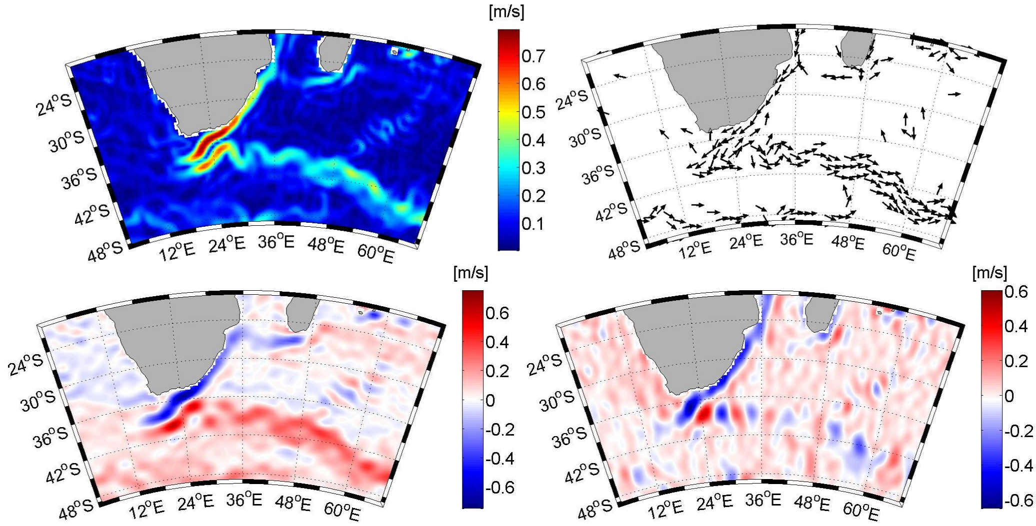

Figure 6.9: The geostrophic velocities in the area of the Agulhas current computed using MDT-GOCE-DTU-180. Upper left panel: magnitude, upper right panel: directions, lower left panel: East component, lower right panel: North component. Units are m/s.

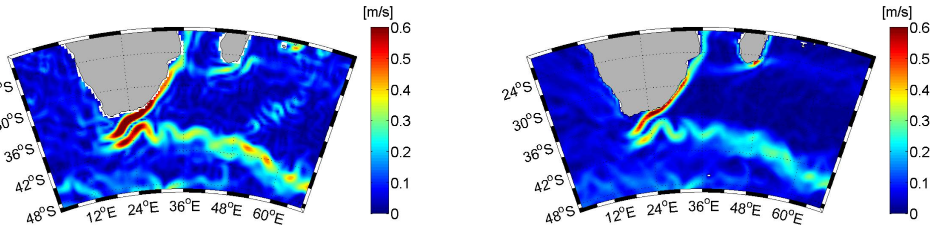

Figure 6.10: Magnitude of the geostrophic velocities from MDT of Maximenko (right panel) and from MDT-GOCE-DTU-180 (left panel) in the area of the Agulhas current. Units are m/s.

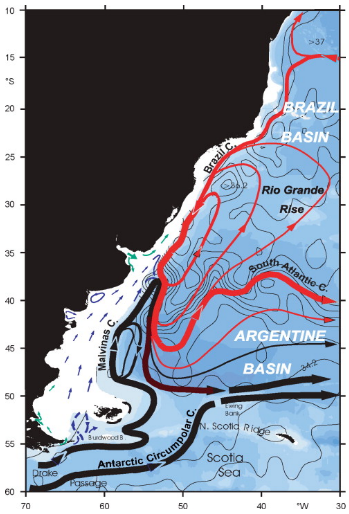

Figure 6.11: The Malvinas current is the northward flow component of the South Atlantic subpolar gyre. It transports cold water along the coast of South America and this water mixes with warmer waters of the Brazil current in a region known as the Brazil-Malvinas confluence. Figure from `http://www.sciencedirect.com/science/article/pii/B012227430X003585`.

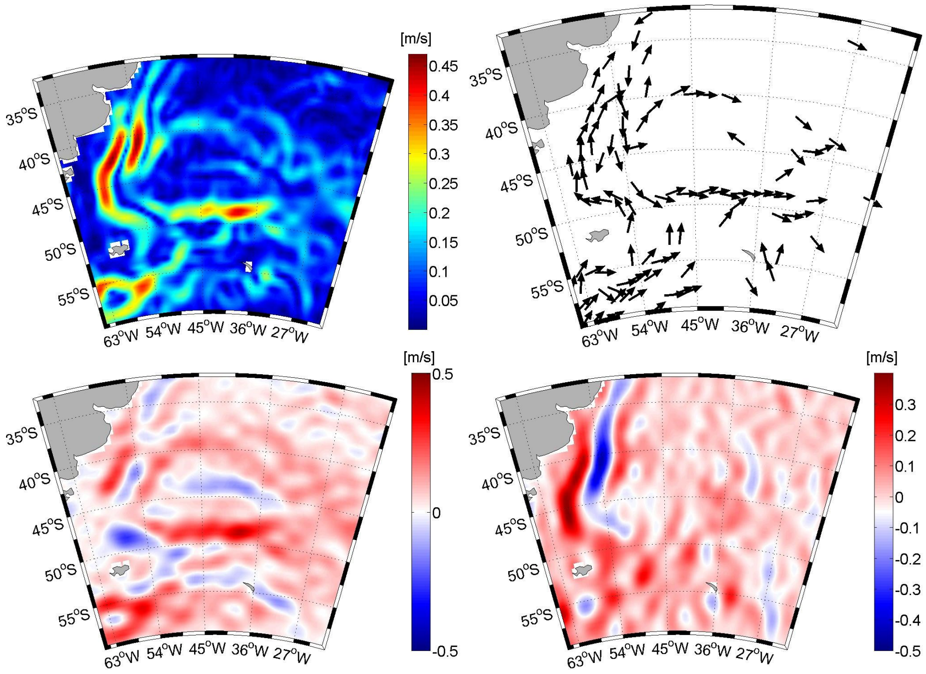

Figure 6.12: The geostrophic velocities in the area of the Malvinas current computed using MDT-GOCE-DTU-180. Upper left panel: magnitude, upper right panel: directions, lower left panel: East component, lower right panel: North component. Units are m/s.

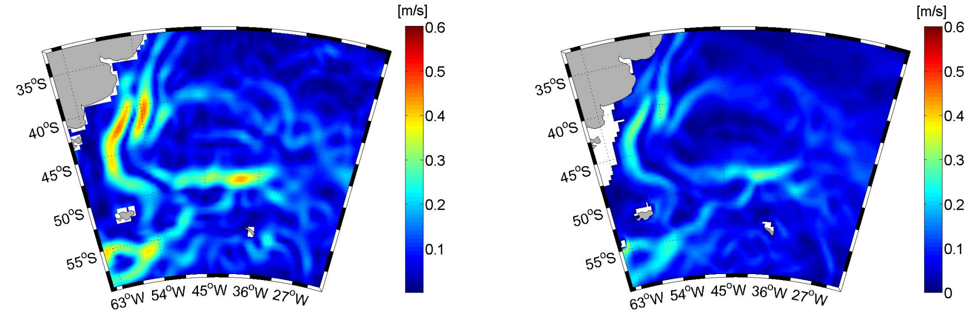

Figure 6.13: Magnitude of the geostrophic velocities from MDT of Maximenko (right panel) and from MDT-GOCE-DTU-180 (left panel) in the area of the Malvinas current. Units are m/s.

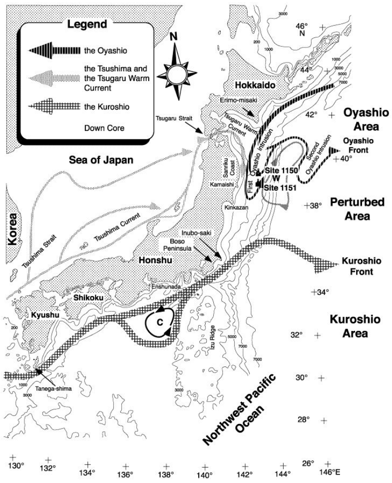

Figure 6.14: The Kuroshio is a north-flowing ocean current along the south coast of Japan on the west side of the North Pacific Ocean. Figure from `http://sitemaker.umich.edu/section2group2/the_slowing_of_ocean_currents`.

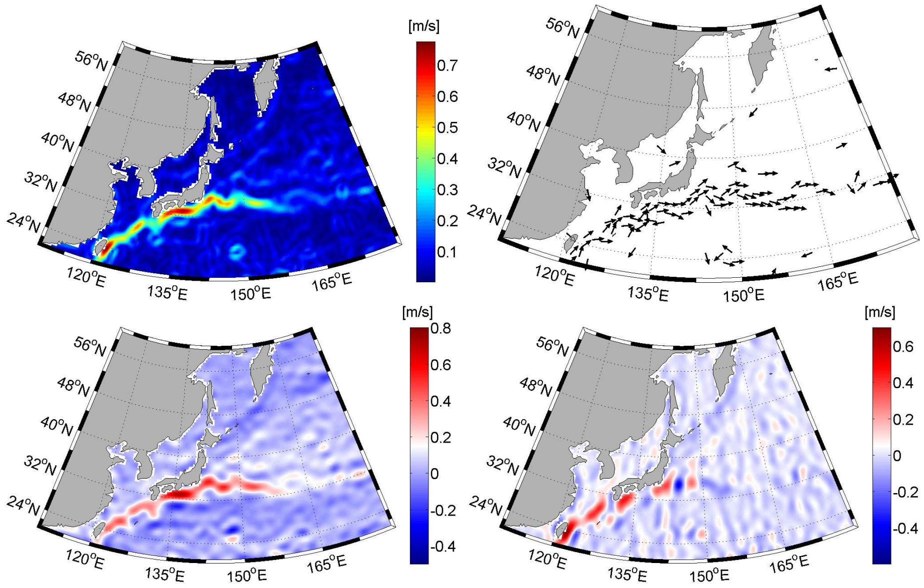

Figure 6.15: The geostrophic velocities in the area of the Kuroshio current computed using MDT-GOCE-DTU-180. Upper left panel: magnitude, upper right panel: directions, lower left panel: East component, lower right panel: North component. Units are m/s.

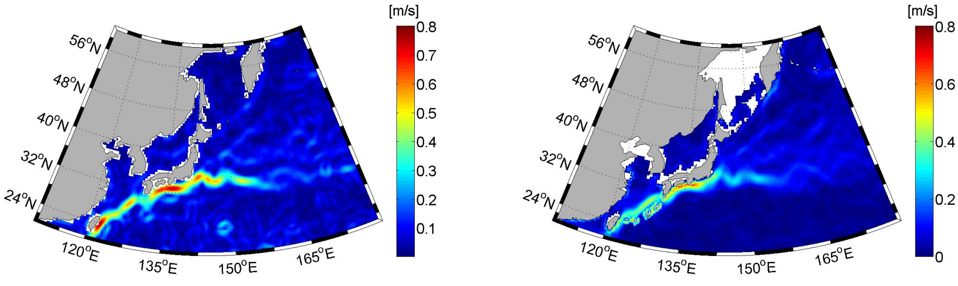

Figure 6.16: Magnitude of the geostrophic velocities from MDT of Maximenko (right panel) and from MDT-GOCE-DTU-180 (left panel) in the area of the Kuroshio current. Units are m/s.

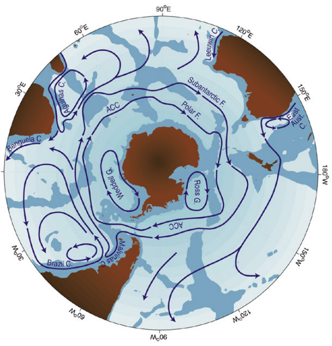

Figure 6.17: The Antarctic Circumpolar Current (ACC) is an ocean current that flows clockwise from west to east around Antarctica. It connects the Atlantic, Pacific and Indian Ocean basins, and serves as a principal pathway of exchange between these basins. Figure from `http://www.science-in-salamanca.tas.csiro.au/themes/climate/currents.htm`.

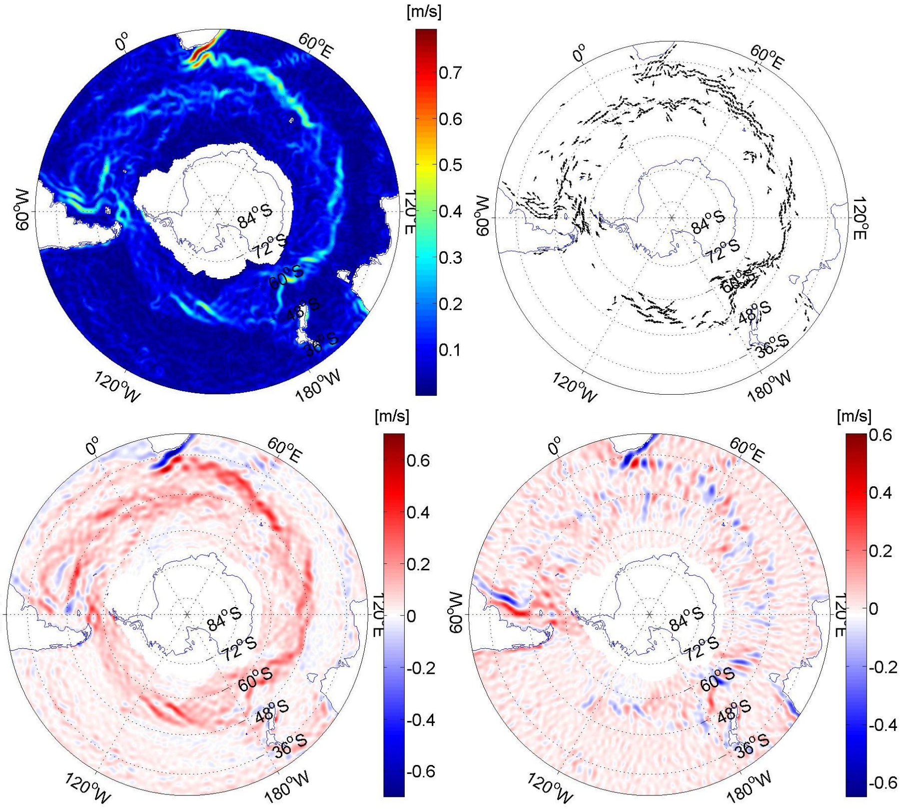

Figure 6.18: The geostrophic velocities in the area of the Antarctic Circumpolar Current computed using MDT-GOCE-DTU-180. Upper left panel: magnitude, upper right panel: directions, lower left panel: East component, lower right panel: North component. Units are m/s.

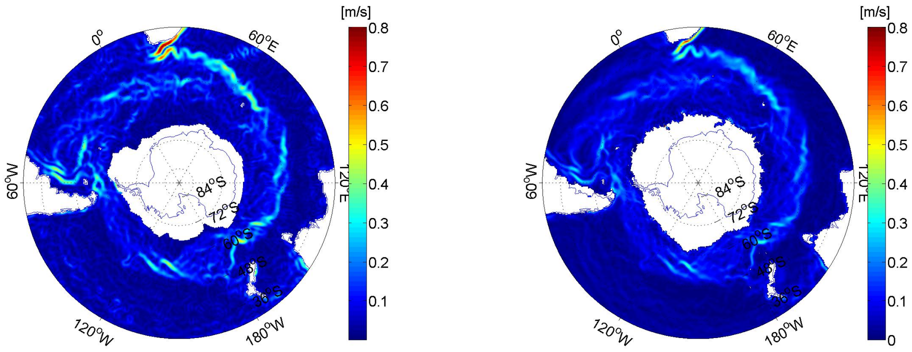

Figure 6.19: Magnitude of the geostrophic velocities from MDT of Maximenko (right panel) and from MDT-GOCE-DTU-180 (left panel) in the area of the ACC current. Units are m/s.

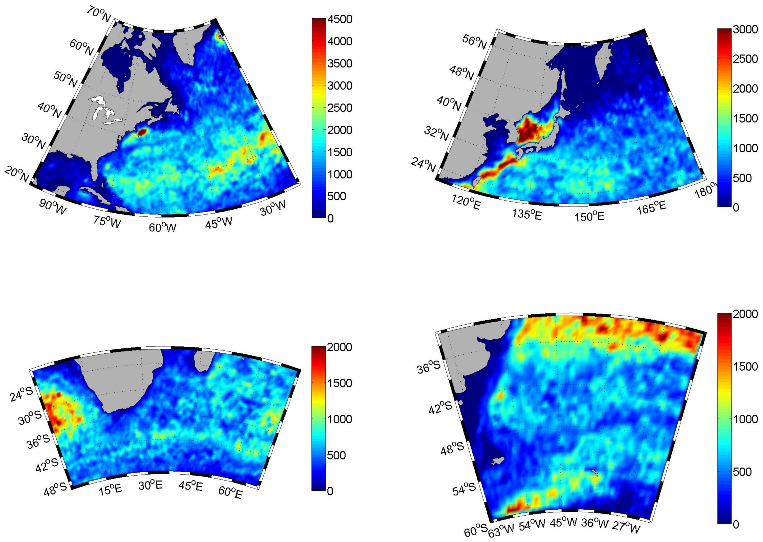

Figure 6.20: Number of drifter observations from 1.1.1993 to 31.12.2009 on a grid $30' \times 30'$. Four areas are considered: Gulf current area (upper left), Kuroshio current area (upper right), Agulhas current area (bottom left) and Malvinas current area (bottom right).

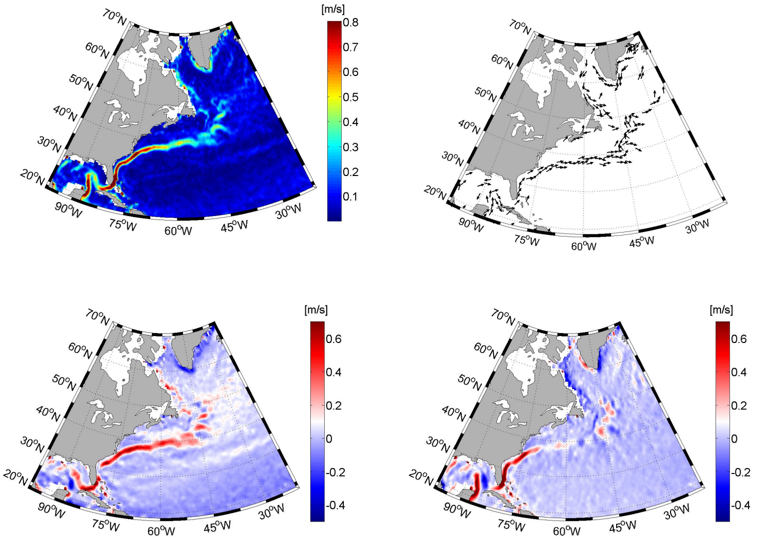

Figure 6.21: Drifter results in the Gulf current area averaged on $30' \times 30'$ grid. Upper left: magnitude, upper right: directions, lower left: East component, lower right: North component. Units are m/s.

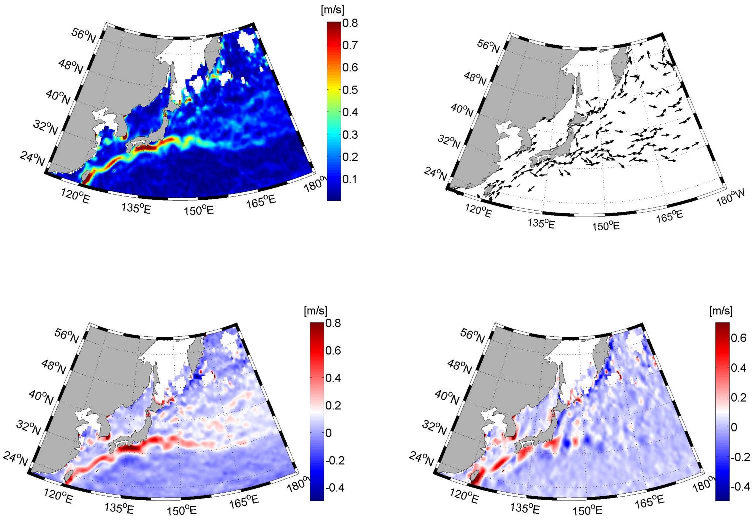

Figure 6.22: Drifter results in the Kuroshio current area averaged on $30' \times 30'$ grid. Upper left: magnitude, upper right: directions, lower left: East component, lower right: North component. Units are m/s.

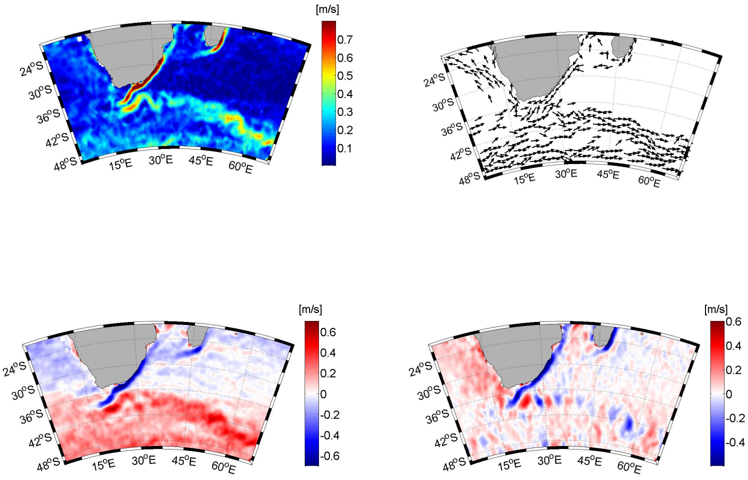

Figure 6.23: Drifter results in the Agulhas current area averaged on 30′ × 30′ grid. Upper left: magnitude, upper right: directions, lower left: East component, lower right: North component. Units are m/s.

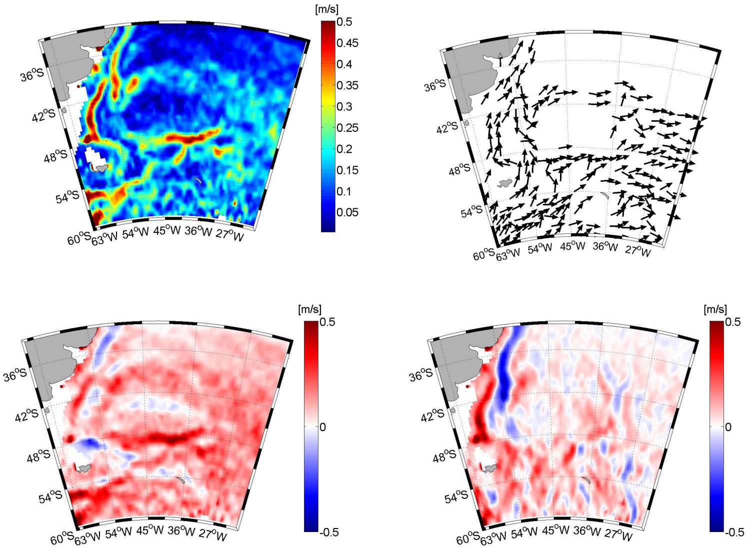

Figure 6.24: Drifter results in the Malvinas current area averaged on 30′ × 30′ grid. Upper left: magnitude, upper right: directions, lower left: East component, lower right: North component. Units are m/s.

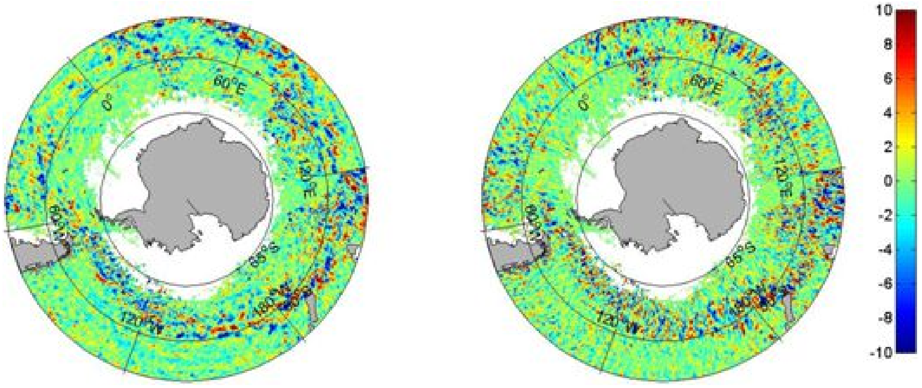

Figure 6.25: Eastward (left panel) and Northward (right panel) component of the velocities derived from the SLA in the area of the ACC current. The MSLA are interpolated on a $30' \times 30'$ grid every month from January 1993 to December 2010 (data from DGFI). For each grid the corresponding geostrophic velocities, through a simple differentiation between adjacent grid points, has been computed. Then each drifter measurement is corrected subtracting the values of the MSLA velocity of the correspondent month. The plots show the difference between the drifter measurements and the same measurements corrected as described above. Units are cm/s.

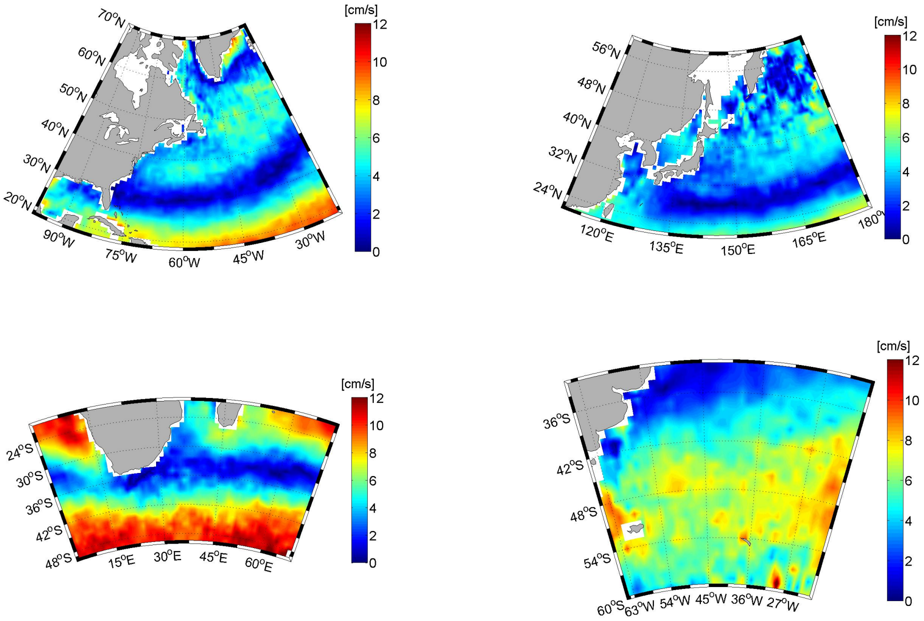

Figure 6.26: Magnitude of the mean Ekman currents in four areas: Gulf current area (upper left), Kuroshio current area (upper right), Agulhas current area (bottom left) and Malvinas current area (bottom right). Units are cm/s.

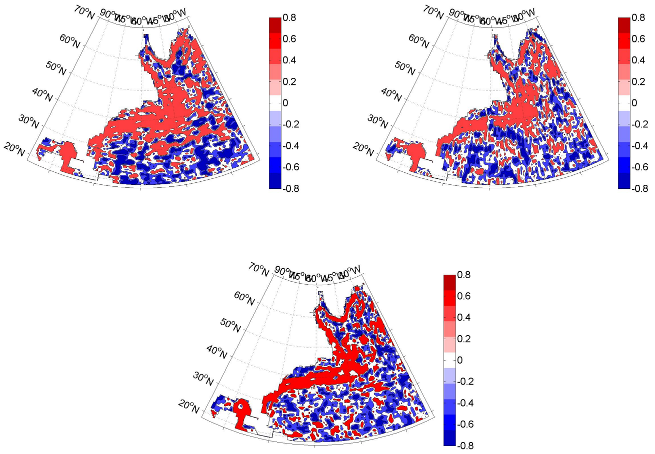

Figure 6.27: Linear correlations between geostrophic velocities from MDT-GOCE-DTU-180 and the velocities from drifter measurements in the Gulf current area. In the upper panel the Eastward (left) and the Northward (right) components are considered. In the lower panel the magnitude of the velocities is considered $V = \sqrt{u^2 + v^2}$.

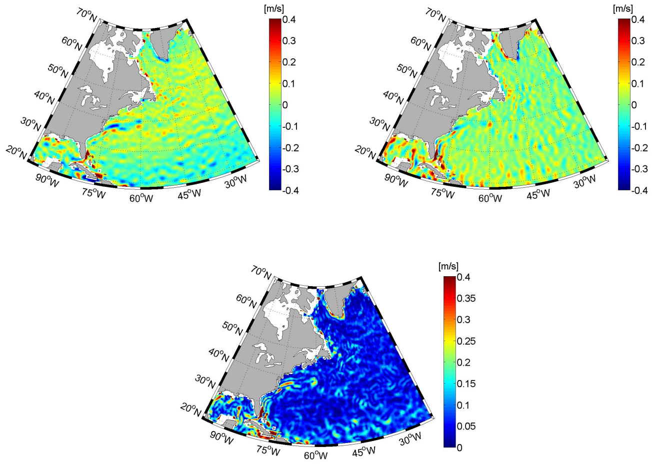

Figure 6.28: Differences between geostrophic velocities from MDT-GOCE-DTU-180 and the velocities from the drifter measurements in the Gulf current area. In the upper panel the differences between the Eastward components (left) and between the Northward (right) components are considered. In the lower panel the magnitude of the vector of the differences ($\Delta V = \sqrt{(u_s - u_d)^2 + (v_s - v_d)^2}$) is shown. Units are m/s.

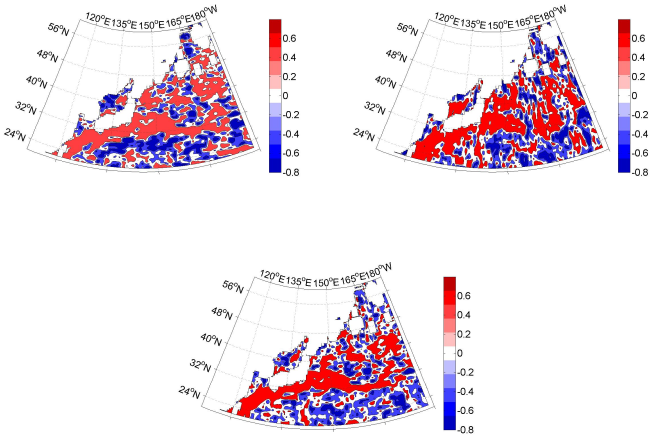

Figure 6.29: Linear correlations between geostrophic velocities from MDT-GOCE-DTU-180 and the velocities from drifter measurements in the Kuroshio current area. In the upper panel the Eastward (left) and the Northward (right) components are considered. In the lower panel the magnitude of the velocities is considered $V = \sqrt{u^2 + v^2}$.

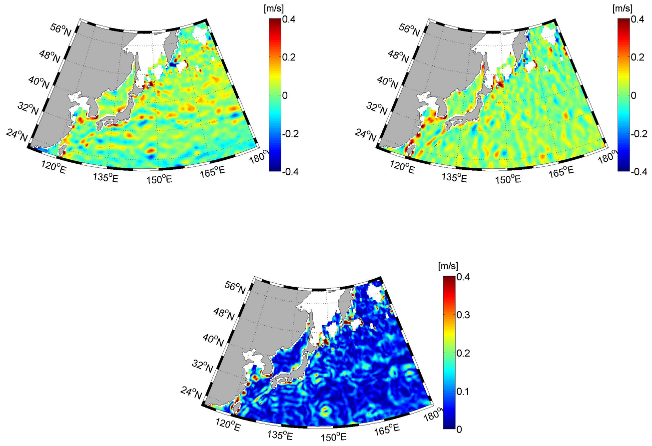

Figure 6.30: Differences between geostrophic velocities from MDT-GOCE-DTU-180 and the velocities from the drifter measurements in the Kuroshio current area. In the upper panel the differences between the Eastward components (left) and between the Northward (right) components are considered. In the lower panel the magnitude of the vector of the differences $(\Delta V = \sqrt{(u_s - u_d)^2 + (v_s - v_d)^2})$ is shown. Units are m/s.

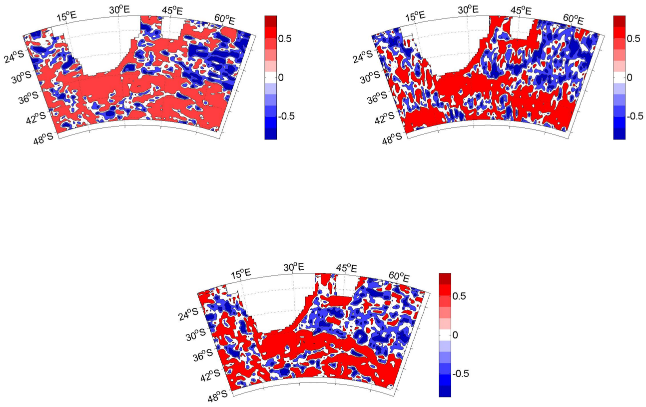

Figure 6.31: Linear correlations between geostrophic velocities from MDT-GOCE-DTU-180 and the velocities from drifter measurements in the Agulhas current area. In the upper panel the Eastward (left) and the Northward (right) components are considered. In the lower panel the magnitude of the velocities is considered $V = \sqrt{u^2 + v^2}$.

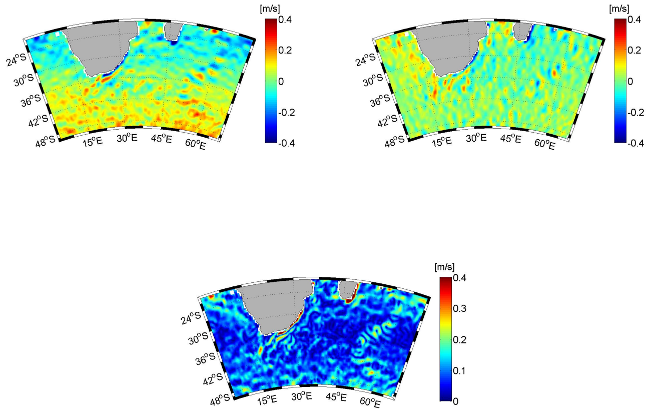

Figure 6.32: Differences between geostrophic velocities from MDT-GOCE-DTU-180 and the velocities from the drifter measurements in the Agulhas current area. In the upper panel the differences between the Eastward components (left) and between the Northward (right) components are considered. In the lower panel the magnitude of the vector of the differences $(\Delta V = \sqrt{((u_s - u_d)^2 + (v_s - v_d)^2)})$ is shown. Units are m/s.

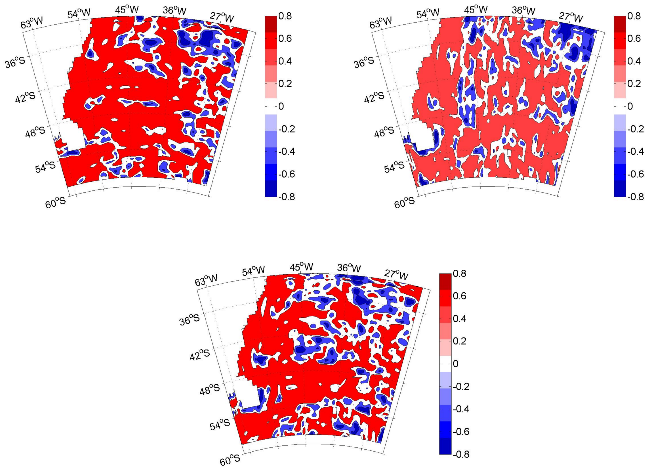

Figure 6.33: Linear correlations between geostrophic velocities from MDT-GOCE-DTU-180 and the velocities from drifter measurements in the Malvinas current area. In the upper panel the Eastward (left) and the Northward (right) components are considered. In the lower panel the magnitude of the velocities is considered $V = \sqrt{u^2 + v^2}$.

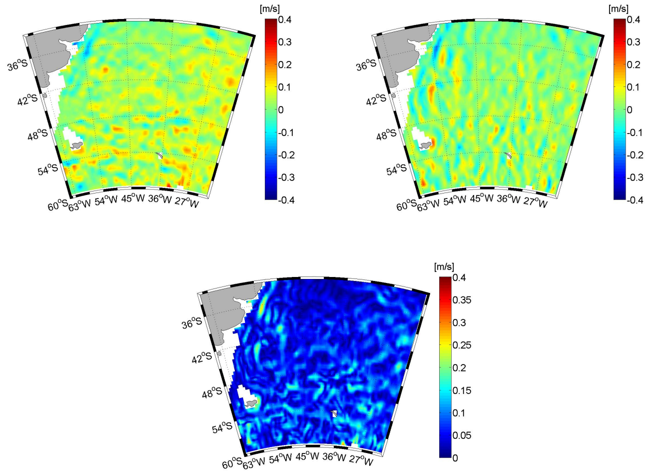

Figure 6.34: Differences between geostrophic velocities from MDT-GOCE-DTU-180 and the velocities from the drifter measurements in the Malvinas current area. In the upper panel the differences between the Eastward components (left) and between the Northward (right) components are considered. In the lower panel the magnitude of the vector of the differences $(\Delta V = \sqrt{(u_s - u_d)^2 + (v_s - v_d)^2})$ is shown. Units are m/s.

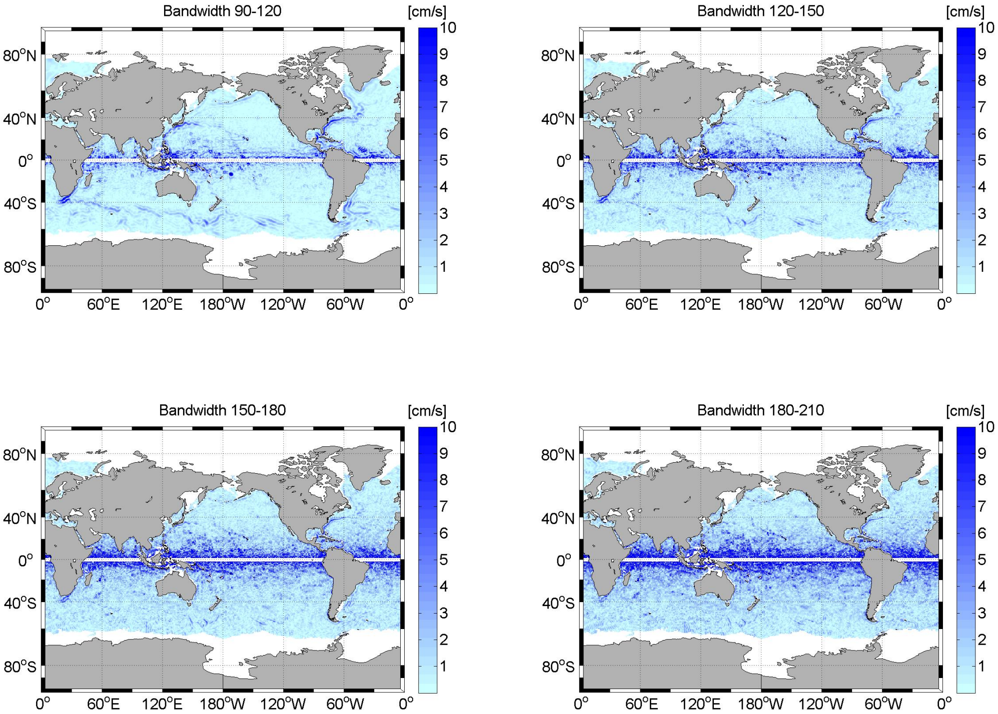

Figure 6.35: The modulus of the geostrophic velocities from MDT-GOCE-DTU in different bandwidths. Units are cm/s.

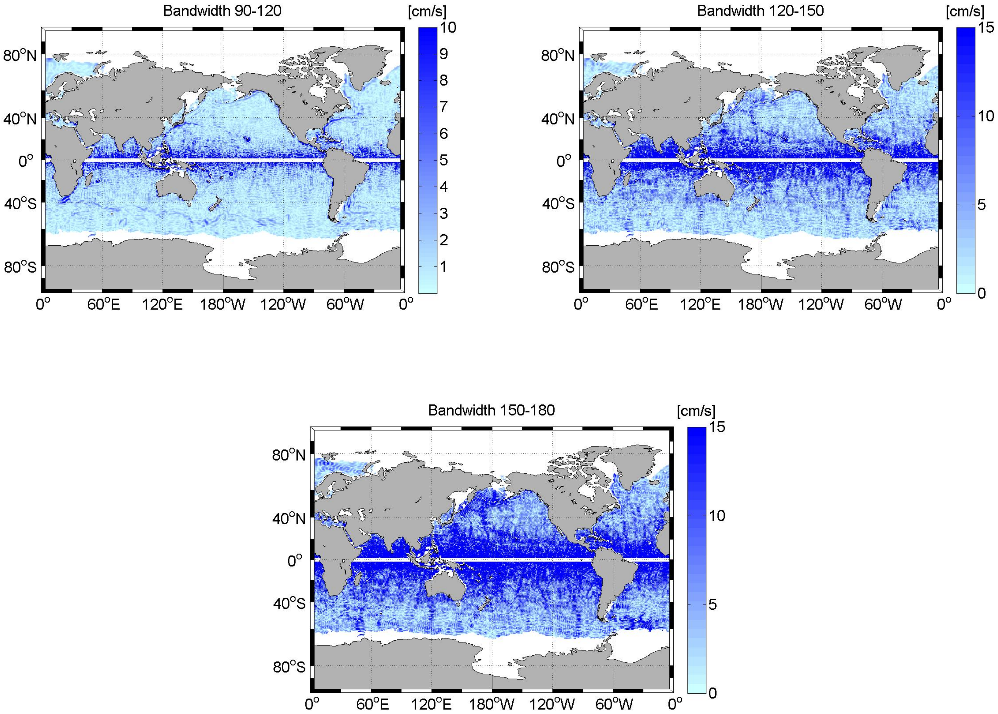

Figure 6.36: The modulus of geostrophic velocities from MDT-GRACE-DTU in different bandwidths. Units are cm/s.

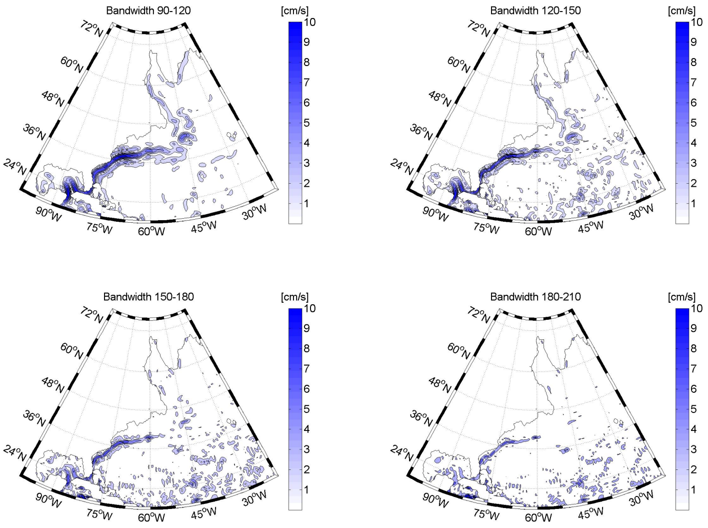

Figure 6.37: The modulus of the geostrophic velocities from MDT-GOCE-DTU in different bandwidths in the area of the Gulf current. Units are cm/s.

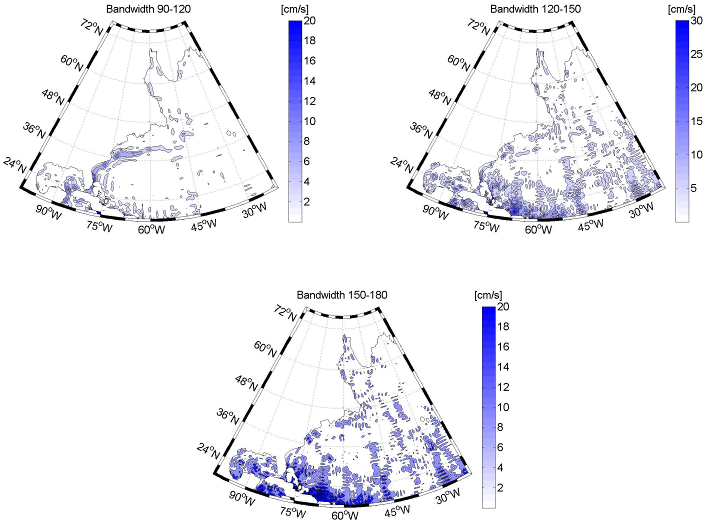

Figure 6.38: The modulus of geostrophic velocities from MDT-GRACE-DTU in different bandwidths in the area of the Gulf current. Units are cm/s.

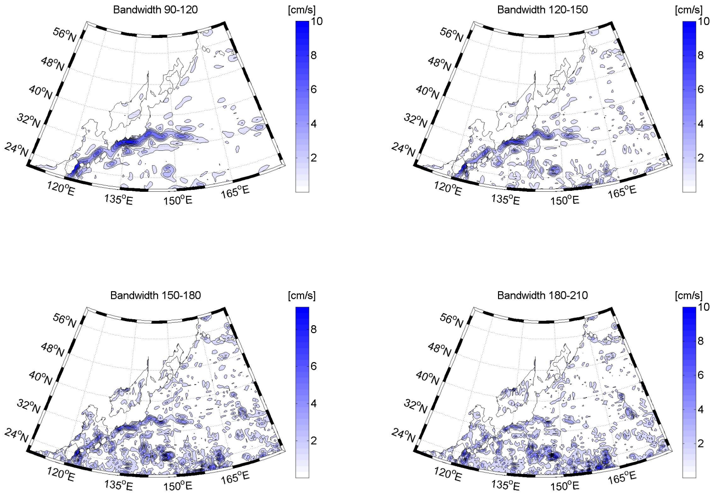

Figure 6.39: The modulus of the geostrophic velocities from MDT-GOCE-DTU in different bandwidths in the area of the Kuroshio current. Units are cm/s.

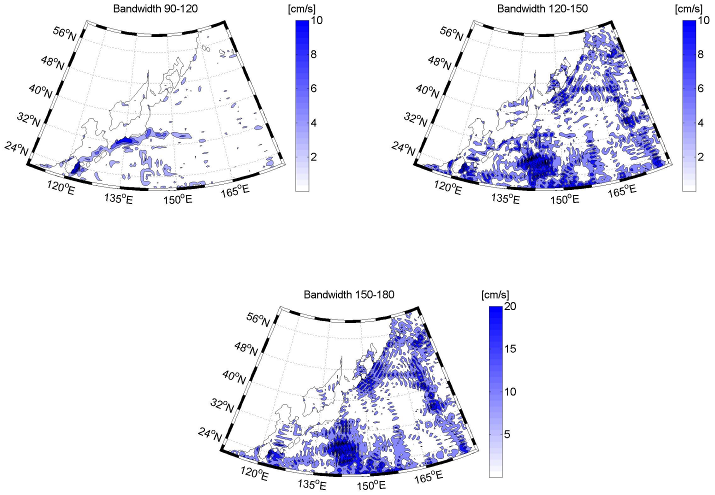

Figure 6.40: The modulus of geostrophic velocities from MDT-GRACE-DTU in different bandwidths in the area of the Kuroshio current. Units are cm/s.

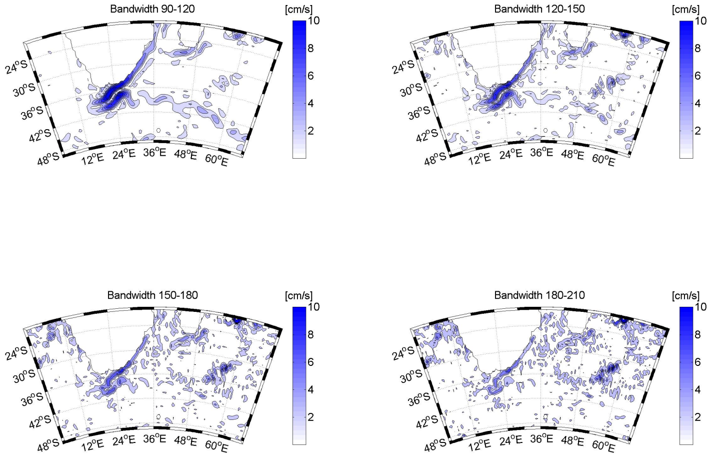

Figure 6.41: The modulus of the geostrophic velocities from MDT-GOCE-DTU in different bandwidths in the area of the Agulhas current. Units are cm/s.

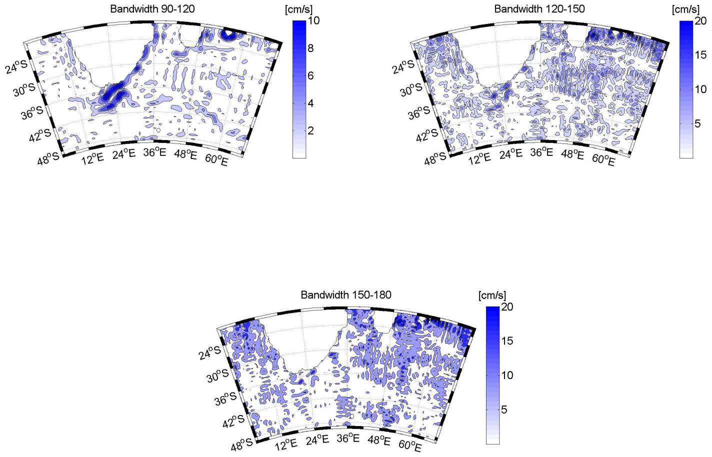

Figure 6.42: The modulus of geostrophic velocities from MDT-GRACE-DTU in different bandwidths in the area of the Agulhas current. Units are cm/s.

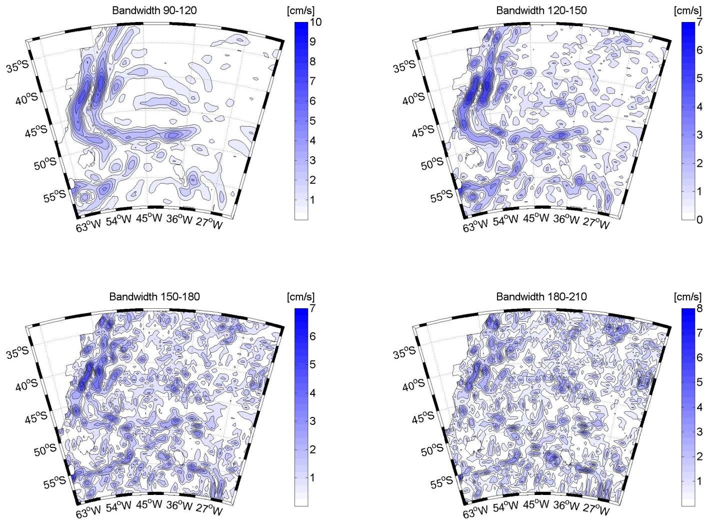

Figure 6.43: The modulus of the geostrophic velocities from MDT-GOCE-DTU in different bandwidths in the area of the Malvinas current. Units are cm/s.

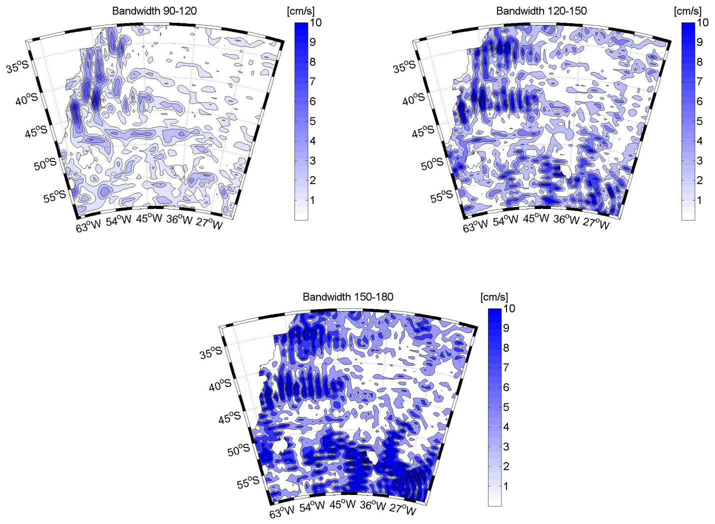

Figure 6.44: The modulus of geostrophic velocities from MDT-GRACE-DTU in different bandwidths in the area of the Malvinas current. Units are cm/s.

Chapter 7

Error propagation to MDT and velocities

The most recent gravity models, from GRACE and GOCE data, are available together with their full error variance covariance matrix, see Mayer-Gürr *et al.* (2010a), Bruinsma *et al.* (2010), Pail *et al.* (2011). This means that we are able to perform the full error propagation from the spherical harmonic coefficients to the geoid undulation, deriving not only the formal error in each point of the earth, but also all the covariances. Including the model of the error of the altimetric data, we can also compute the full variance covariance matrix of the Mean Dynamic Topography (MDT) and of the geostrophic surface velocities.

7.1 Error propagation to MDT

As it is shown in chapter 5, the MDT is given by the difference between the ellipsoidal height of the sea surface measured by altimetry and the geoid height:

$$H = h - N \ . \tag{7.1}$$

The variance-covariance matrix (VCM) of the MDT contains the error contributions of the mean sea surface and of the geoid heights. It can be written as

$$C_{HH} = C_{hh} + C_{NN} + C_{hN} \tag{7.2}$$

Thereby C_{HH} is the error-VCM of the mean dynamic topography, C_{hh} the error-VCM of the mean sea surface, C_{NN} is the error-VCM of the geoid heights and C_{hN} is the matrix containing the correlations between N and h. C_{hN} can be disregarded, because geoid and sea surface determination are completely independent processes.

Considering the spherical harmonic representation of the geoid heights, compare Eq. (2.1), we can write:

$$H = h - N = h - R\sum_{\ell=0}^{L}\sum_{m=0}^{\ell}\left(\overline{C}_{\ell m}\cos m\lambda_P + \overline{S}_{\ell m}\sin m\lambda_P\right)\bar{P}_{\ell m}\cos(\vartheta_P) \tag{7.3}$$

or in matrix form:

$$H = h - At \tag{7.4}$$

where A the propagation matrix, which gives the linear relation between the geoid heights N and the vector of spherical harmonic coefficients t.

From the linear error propagation law, Eq. (7.2) becomes:

$$C_{HH} = C_{hh} + AC_{tt}A^T \ . \tag{7.5}$$

We are considering the MSS on the nodes of a geographical grid. This means that the original measurements along the satellite tracks have been interpolated. The gridding causes correlations between sea surface heights of neighboring grid nodes. In this report we do not consider such correlations and the matrix C_{hh} is approximated by a diagonal matrix containing only the variances of the sea surface heights on the nodes of our geographical grid. As expected, the largest errors are along the coastlines and in the regions of the major oceanic currents (see Fig. 7.1). However features along the repeating satellite tracks are visible too.

The matrices C_{HH} and C_{hh} have size $k \times k$ where k is the number of considered points (for example $k = 23592$ for a complete $5^\circ \times 5^\circ$ grid). The matrix C_{tt} has size $j \times j$ where j is the number of spherical harmonic coefficients up to the fixed maximum degree L of the expansion in Eq. (7.3). The structure of the matrix depends on the chosen ordering of the coefficients. For example, as in Fig. 7.2, with the sorting “degree-order” the ordening is

$$\overline{C}_{00}, \overline{C}_{10}, \overline{C}_{11}, \overline{S}_{11}, \overline{C}_{20}, \overline{C}_{21}, \overline{S}_{21}, \overline{C}_{22}, \overline{S}_{22}, \overline{C}_{30}, \overline{C}_{31}, \overline{S}_{31}, \cdots \ .$$

With the sorting “order-degree” the sequence is

$$\overline{C}_{00}, \overline{C}_{10}, \overline{C}_{20}, \overline{C}_{30}, \cdots, \overline{C}_{11}, \overline{S}_{11}, \overline{C}_{21}, \overline{S}_{21}, \overline{C}_{31}, \overline{S}_{31}, \cdots, \overline{C}_{22}, \overline{S}_{22}, \overline{C}_{32}, \overline{S}_{32} \cdots$$

as in Gerlach & Fecher (2013).

The propagation matrix A has size $k \times j$. The number of spherical harmonic coefficients of a gravity model up to degree and order 250 is 63001 and therefore the size of the matrix C_{tt} is 63001×63001. Obviously propagation of such a large matrix is a numerically demanding and time consuming task, see Pail & Fecher (2011), Horvath & Pail (2012a), Horvath & Pail (2012b) and Pail *et al.* (2012).

In Gerlach & Fecher (2013) three different levels of approximation of the full VCM are compared. Gerlach & Fecher (2013) show that using only elements of the dominant m-block structure of the VCM we obtain almost the same result as provided by the full VCM. This level of approximation is called the m-block approach.

Following this approach, we propagated the error from the spherical harmonic coefficients of the gravity model GOCO03S, up degree and order 180, to the geoid heights of a grid $1^\circ \times 1^\circ$. In Fig. 7.3 the variances (derived from diagonal of the matrix $AC_{tt}A^T$) of the geoid heights are shown. We observe that the error pattern does not depend on the longitude and is slightly asymmetric with respect to the equator. The maximum is at the poles (5 cm), because of the non-polar inclination of the orbit of GOCE. Around the equator the error is about 3 cm and it decreases for higher latitudes (this because the density of the measurements increases with latitude).

In the MDT computation described in section 5.2.3, a Gauss filter is applied to the spherical harmonic coefficients. The result of the error propagation considering that filter is shown in Fig. 7.4. In this case the error is always below 1 cm and it is negligible compared to the altimetric error. In Table 7.1 the statistics of the propagated geoid error are shown.

	Mean	**RMS**	**max**	**min**
no filter	2.63	0.71	4.76	1.13
Gauss filter	0.55	0.15	0.92	0.22

Table 7.1: Statistics of the propagated geoid error comparing a Gauss filter applied to the VCM matrix with the results considering an un-filtered VCM matrix. Units are centimeters.

In Fig. 7.5 the total error of the MDT is shown. We observe that at medium latitudes ($-45° < \varphi < 45°$) the geoid error is dominant, while for high latitudes the altimetric error is bigger.

Fig. 7.6 and Fig. 7.7 show the covariances of the MDT, evaluated in the central point of the grid $\varphi = 0°, \lambda = 180°$. The covariances are symmetrical and almost isotropic.

In Fig. 7.8 and Fig. 7.9 the standard deviations and the correlations in the Agulhas current area ($45°S < \varphi < 75°S$, $260° < \lambda < 320°$) are shown. In this area, the propagated error to the geoid heights is everywhere below 3.5 centimeters.

Comparing the covariance functions values along the East-West (E-W) direction (Fig. 7.10 upper panel) with those along the North-South (N-S) direction (Fig. 7.10 lower panel), we observe that there are slightly different characteristics: the correlation length is $\cong 0.4°$ for the E-W direction and $\cong 0.6°$ for the N-S direction. The first zero is at 0.5° for the E-W direction and at 1.18° for the N-S direction.

7.2 Error propagation to geostrophic flow

In (Elema, 1993) the formulas of the error covariances of the ocean circulation are derived.

Applying the law of the covariance propagation to Eq. (6.12) we obtain the covariance of the surface velocity in the longitude and latitude direction and their correlations. The covariance of the surface velocity between a point P and a point Q for the longitude direction is:

$$COV(u_P, u_Q) = \frac{g}{f}\frac{1}{R} COV\left(\frac{\partial H_P}{\partial \vartheta}, \frac{\partial H_Q}{\partial \vartheta}\right) \frac{g}{f}\frac{1}{R} \tag{7.6}$$

and for the latitude direction:

$$COV(v_P, v_Q) = \frac{g}{f}\frac{1}{R\sin\vartheta_P} COV\left(\frac{\partial H_P}{\partial \lambda}, \frac{\partial H_Q}{\partial \lambda}\right) \frac{g}{f}\frac{1}{R\sin\vartheta_Q} \ . \tag{7.7}$$

The covariance between the latitude and longitude direction is:

$$COV(u_P, v_Q) = \frac{g}{f}\frac{1}{R} COV\left(\frac{\partial H_P}{\partial \vartheta}, \frac{\partial H_Q}{\partial \lambda}\right) \frac{g}{f}\frac{1}{R\sin\vartheta_Q} \tag{7.8}$$

where $f = 2\Omega\cos\vartheta$ is the Coriolis coefficient. Here Ω is the angular velocity of the earth and ϑ is the colatitude.

In section 7.1 we assumed that the VCM of the sea surface heights is diagonal (no correlations) and that there are no correlations between geoid and mean sea surface. From Fig. 7.1 we observe that the variance of h changes from place to place. Using the finite differences we compute the north and east gradient components of the variance of h, see Fig. 7.11 and Fig. 7.12. We find that the change in the map on a cell of our grid (0.5°) in the north and east directions have an order of magnitude of 10^{-5}. This effect is disregarded in the following.

Partial differentiation of Eq. (2.1) to ϑ gives:

$$\frac{\partial N_P}{\partial \vartheta} = \sum_{m=0}^{L} \left[A_m^L\right]' \cos m\lambda_P + \left[B_m^L\right]' \sin m\lambda_P \tag{7.9}$$

with coefficients:

$$\begin{pmatrix} \left[A_m^L\right]' \\ \left[B_m^L\right]' \end{pmatrix} = R \sum_{\ell=m}^{L} \bar{P}'_{\ell m} \cos(\vartheta_P) \begin{pmatrix} \bar{C}_{\ell m} \\ \bar{S}_{\ell m} \end{pmatrix} \tag{7.10}$$

where $\bar{P}'_{\ell m}$ is the first derivative of the Legendre functions with respect to ϑ.

Partial differentiation of Eq. (2.1) to λ is:

$$\frac{\partial N_P}{\partial \lambda} = \sum_{m=0}^{L} m\left(-A_m^L \sin m\lambda_P + B_m^L \cos m\lambda_P\right) \tag{7.11}$$

with coefficients:

$$\begin{pmatrix} A_m^L \\ B_m^L \end{pmatrix} = R \sum_{\ell=m}^{L} \bar{P}_{\ell m} \cos(\vartheta_P) \begin{pmatrix} \bar{C}_{\ell m} \\ \bar{S}_{\ell m} \end{pmatrix} . \tag{7.12}$$

Applying the law of covariance propagation to the partial derivatives of the geoid height (7.9) and (7.11) we obtain the covariances of the partial derivatives of the geoid height in a Fourier representation. After combining the result of this error propagation with the formulas (7.6) and (7.7) we obtain the formulas for the covariance of the ocean surface velocity.

The covariance of the ocean circulation in longitude direction is:

$$
\begin{aligned}
COV(u_P, u_Q) = \sum_{m=0}^{L}\sum_{k=0}^{L} [\quad & A_{mk}^{uu} \cos m\lambda_P \cos k\lambda_Q + \\
& B_{mk}^{uu} \sin m\lambda_P \cos k\lambda_Q + \\
& C_{mk}^{uu} \cos m\lambda_P \sin k\lambda_Q + \\
& D_{mk}^{uu} \sin m\lambda_P \sin k\lambda_Q \ ]
\end{aligned} \tag{7.13}
$$

with Fourier coefficients:

$$
A_{mk}^{uu} = \frac{g}{f_P}\frac{g}{f_Q}\sum_{n=m}^{L}\sum_{\ell=k}^{L}\overline{P}'_{nm}(\cos\vartheta_P)\overline{P}'_{\ell k}(\cos\vartheta_Q)COV(\overline{C}_{nm},\overline{C}_{\ell k})
$$

$$
B_{mk}^{uu} = \frac{g}{f_P}\frac{g}{f_Q}\sum_{n=m}^{L}\sum_{\ell=k}^{L}\overline{P}'_{nm}(\cos\vartheta_P)\overline{P}'_{\ell k}(\cos\vartheta_Q)COV(\overline{S}_{nm},\overline{C}_{\ell k})
$$

$$
C_{mk}^{uu} = \frac{g}{f_P}\frac{g}{f_Q}\sum_{n=m}^{L}\sum_{\ell=k}^{L}\overline{P}'_{nm}(\cos\vartheta_P)\overline{P}'_{\ell k}(\cos\vartheta_Q)COV(\overline{C}_{nm},\overline{S}_{\ell k})
$$

$$
D_{mk}^{uu} = \frac{g}{f_P}\frac{g}{f_Q}\sum_{n=m}^{L}\sum_{\ell=k}^{L}\overline{P}'_{nm}(\cos\vartheta_P)\overline{P}'_{\ell k}(\cos\vartheta_Q)COV(\overline{S}_{nm},\overline{S}_{\ell k})
$$

For the covariances of the ocean circulation in latitude direction, we have:

$$
\begin{aligned}
COV(v_P, v_Q) = \sum_{m=0}^{L}\sum_{k=0}^{L} [\quad & A_{mk}^{vv} \cos m\lambda_P \cos k\lambda_Q + \\
& B_{mk}^{vv} \sin m\lambda_P \cos k\lambda_Q + \\
& C_{mk}^{vv} \cos m\lambda_P \sin k\lambda_Q + \\
& D_{mk}^{vv} \sin m\lambda_P \sin k\lambda_Q \ ]
\end{aligned} \tag{7.14}
$$

with Fourier coefficients

$$
A_{mk}^{vv} = \frac{g}{f_P}\frac{1}{\sin\vartheta_P}m\frac{g}{f_Q}\frac{1}{\sin\vartheta_Q}k\sum_{n=m}^{L}\sum_{\ell=k}^{L}\overline{P}_{nm}(\cos\vartheta_P)\overline{P}_{\ell k}(\cos\vartheta_Q)COV(\overline{S}_{nm},\overline{S}_{\ell k})
$$

$$B^{vv}_{mk} = -\frac{g}{f_P}\frac{1}{\sin\vartheta_P}m\frac{g}{f_Q}\frac{1}{\sin\vartheta_Q}k\sum_{n=m}^{L}\sum_{\ell=k}^{L}\overline{P}_{nm}(\cos\vartheta_P)\overline{P}_{\ell k}(\cos\vartheta_Q)COV(\overline{C}_{nm},\overline{S}_{\ell k})$$

$$C^{vv}_{mk} = -\frac{g}{f_P}\frac{1}{\sin\vartheta_P}m\frac{g}{f_Q}\frac{1}{\sin\vartheta_Q}k\sum_{n=m}^{L}\sum_{\ell=k}^{L}\overline{P}_{nm}(\cos\vartheta_P)\overline{P}_{\ell k}(\cos\vartheta_Q)COV(\overline{S}_{nm},\overline{C}_{\ell k})$$

$$D^{vv}_{mk} = \frac{g}{f_P}\frac{1}{\sin\vartheta_P}m\frac{g}{f_Q}\frac{1}{\sin\vartheta_Q}k\sum_{n=m}^{L}\sum_{\ell=k}^{L}\overline{P}_{nm}(\cos\vartheta_P)\overline{P}_{\ell k}(\cos\vartheta_Q)COV(\overline{C}_{nm},\overline{C}_{\ell k})\ .$$

The model for the computation of the full covariance matrix case of an arbitrary geopotential model is essential for the computation of the covariance in latitude and in longitude direction.

The covariances of the ocean circulation between longitude and latitude direction, are:

$$\begin{aligned} COV(u_P,v_Q) = \sum_{m=0}^{L}\sum_{k=0}^{L}[\quad & A^{uv}_{mk}\cos m\lambda_P\cos k\lambda_Q + \\ & B^{uv}_{mk}\sin m\lambda_P\cos k\lambda_Q + \\ & C^{uv}_{mk}\cos m\lambda_P\sin k\lambda_Q + \\ & D^{uv}_{mk}\sin m\lambda_P\sin k\lambda_Q\ ] \end{aligned} \tag{7.15}$$

with Fourier coefficients

$$A^{uv}_{mk} = \frac{g}{f_P}\frac{g}{f_Q}\frac{1}{\sin\vartheta_Q}k\sum_{n=m}^{L}\sum_{\ell=k}^{L}\overline{P}'_{nm}(\cos\vartheta_P)\overline{P}_{\ell k}(\cos\vartheta_Q)COV(\overline{C}_{nm},\overline{S}_{\ell k})$$

$$B^{uv}_{mk} = \frac{g}{f_P}\frac{g}{f_Q}\frac{1}{\sin\vartheta_Q}k\sum_{n=m}^{L}\sum_{\ell=k}^{L}\overline{P}'_{nm}(\cos\vartheta_P)\overline{P}_{\ell k}(\cos\vartheta_Q)COV(\overline{S}_{nm},\overline{S}_{\ell k})$$

$$C^{uv}_{mk} = -\frac{g}{f_P}\frac{g}{f_Q}\frac{1}{\sin\vartheta_Q}k\sum_{n=m}^{L}\sum_{\ell=k}^{L}\overline{P}_{nm}(\cos\vartheta_P)\overline{P}_{\ell k}(\cos\vartheta_Q)COV(\overline{C}_{nm},\overline{C}_{\ell k})$$

$$D^{uv}_{mk} = -\frac{g}{f_P}\frac{g}{f_Q}\frac{1}{\sin\vartheta_Q}k\sum_{n=m}^{L}\sum_{\ell=k}^{L}\overline{P}_{nm}(\cos\vartheta_P)\overline{P}_{\ell k}(\cos\vartheta_Q)COV(\overline{S}_{nm},\overline{C}_{\ell k})$$

To analyze the variance and the covariance structure the area of the Agulhas current ($45°S < \varphi < 75°S$, $260° < \lambda < 320°$) has been selected. A global analysis is complicated because of the singularity along the equator. In the region close to the equator the geostrophic balance does not hold. It has been excluded from the error propagation. Fig. 7.13 shows the propagated error from the spherical harmonic coefficients to the components of the geostrophic velocities. In this area, the maximum error for the North component is 11 cm/s and for the East component it is 8 cm/s.

Fig. 7.14 shows the covariances of the components of the geostrophic velocities. The covariances of the component v are symmetric along the direction E-W, while the component u shows un-isotropic features along the N-S direction. This could be due to the dependence of the error of the gravitational field on latitude (see Fig. 7.3). A more proper index is the linear correlation, defined as:

$$R(v_P, v_Q) = \frac{COV(v_P, v_Q)}{\sqrt{VAR(v_P)VAR(v_Q)}} \quad R(u_P, u_Q) = \frac{COV(u_P, u_Q)}{\sqrt{VAR(u_P)VAR(u_Q)}} \ . \tag{7.16}$$

Fig. 7.15 shows the correlations of the two components of the geostrophic velocities. As expected in this case the correlation of the a-symmmetry of the u component along the N-S direction is much less pronounced.

Comparing the covariance function values of the v component along the E-W direction (Fig. 7.16 upper panel) with those along the N-S direction (Fig. 7.16 lower panel), we observe that there are different characteristics: the correlation length is ≅ 0.4° for the E-W direction and ≅ 0.9° for the N-S direction. The first zero is at 0.59° for the E-W direction and at 3.8° for the N-S direction. The covariance function values of the u component along the E-W direction and along the N-S direction are shown in Fig. 7.17. In this case the correlation length is ≅ 0.7° for the E-W direction and ≅ 0.4° for the N-S direction. The first zero is at 1.14° for the E-W direction and at 0.65° for the N-S direction.

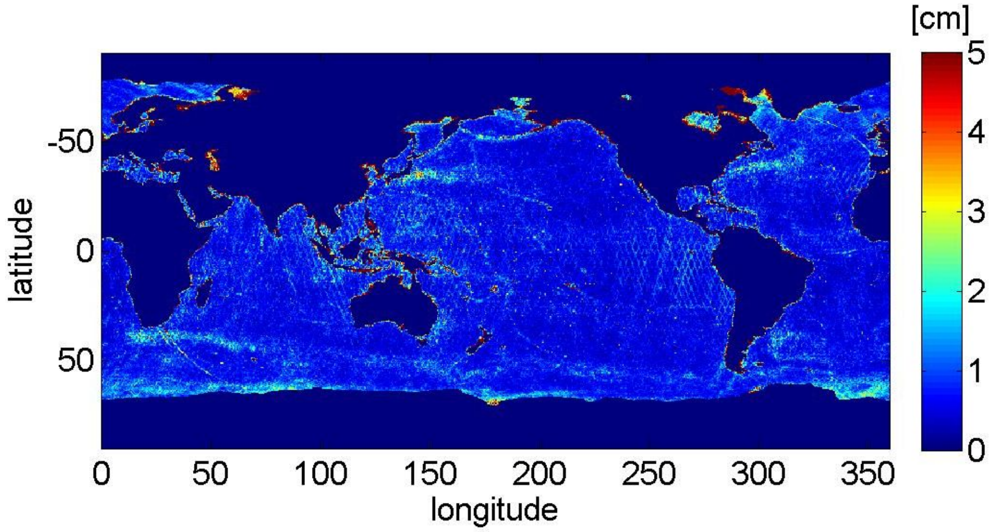

Figure 7.1: Geographical distribution of the errors of the mean sea surface DGFI10. Units are centimeters.

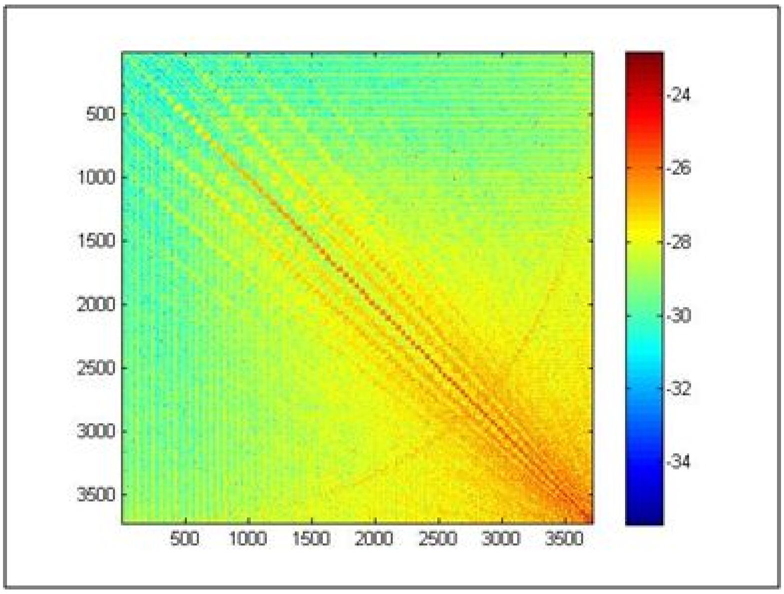

Figure 7.2: Full VCM up degree and order 60 of the gravity model GOCE TIM-3. The scale is logarithmic. The size of the matrix is 3721 × 3721.

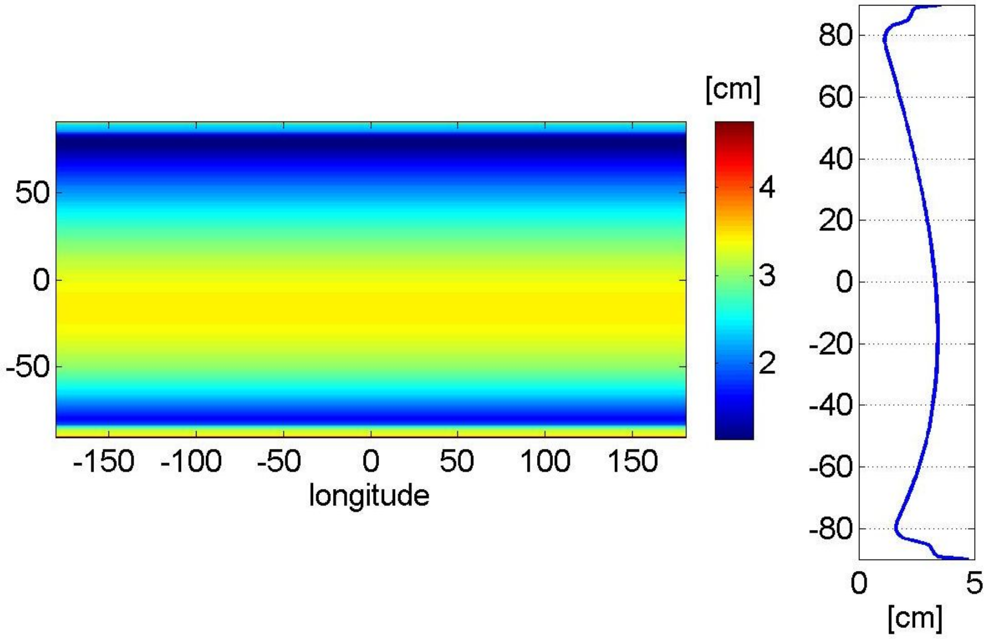

Figure 7.3: Left panel: geographical distribution of the propagated geoid errors from the spherical harmonic coefficients of the gravity model GOCO3S. Right panel: error as function of latitude.

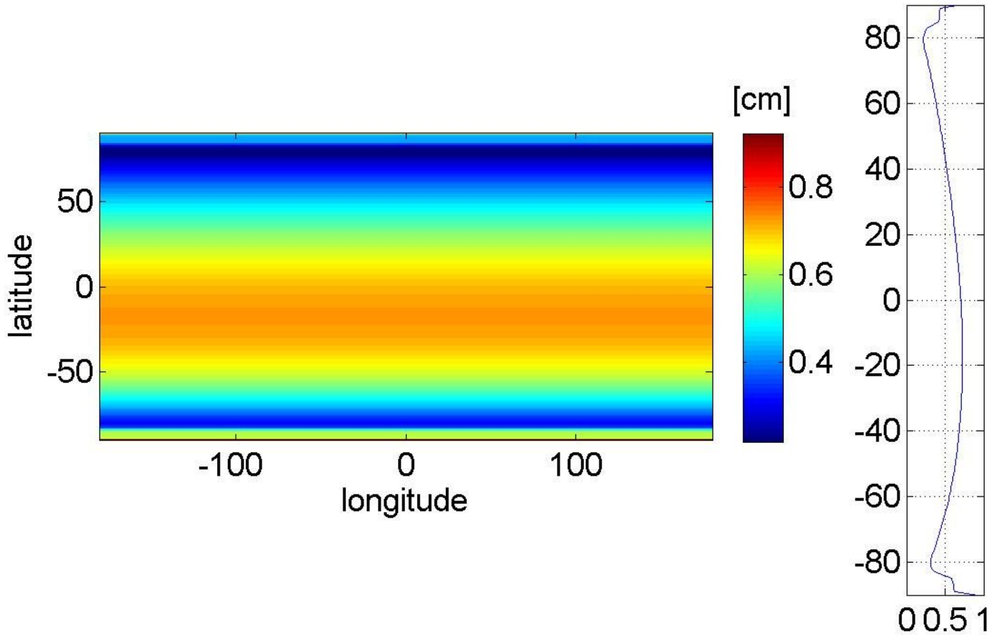

Figure 7.4: Left panel: geographical distribution of the propagated geoid errors from the spherical harmonic coefficients of the gravity model GOCO3S. Right panel: error as function of latitude. A Gauss filter up degree and order 180 is applied.

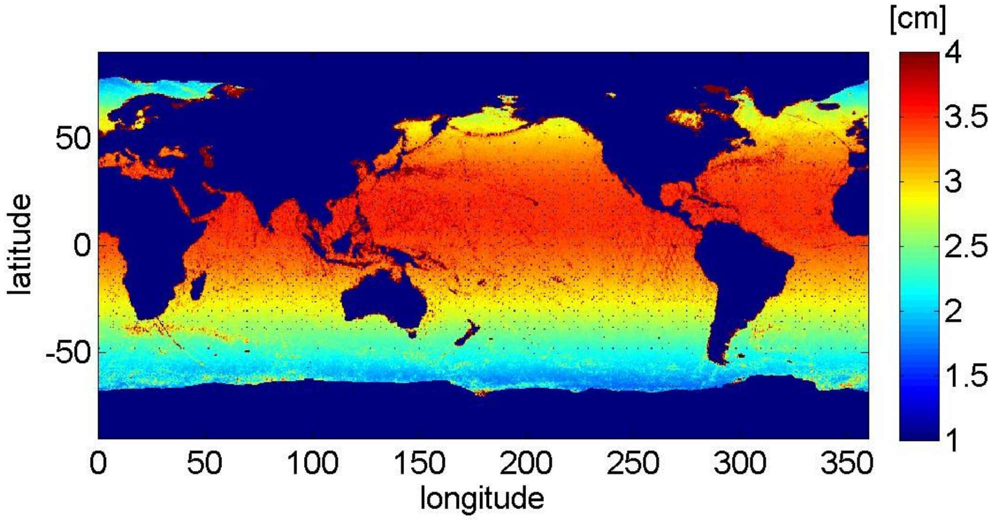

Figure 7.5: Geographical distribution of the cumulative error of the MDT, considering the errors of the geoid heights and of the altimetric MSS.

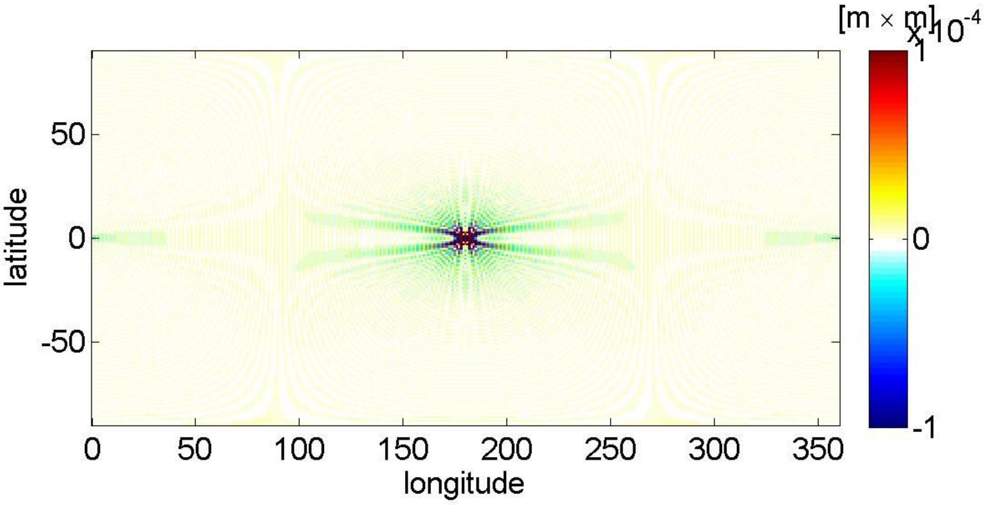

Figure 7.6: Covariance function evaluated for the point $\varphi = 0°, \lambda = 180°$.

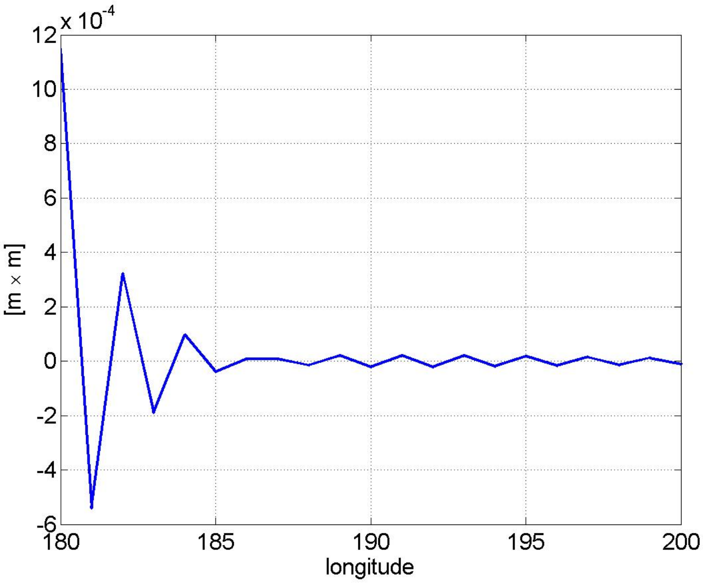

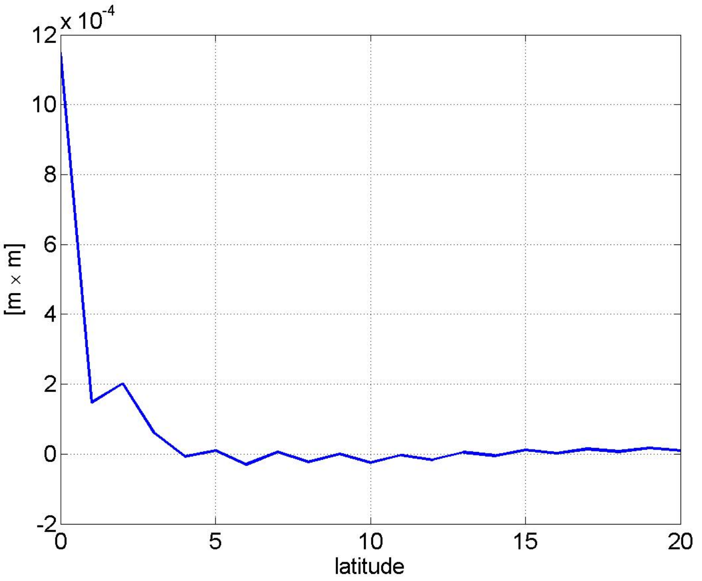

Figure 7.7: Sections of the covariance function of the MDT as function of the latitude and of the longitude, centered in the point $\varphi = 0°, \lambda = 180°$.

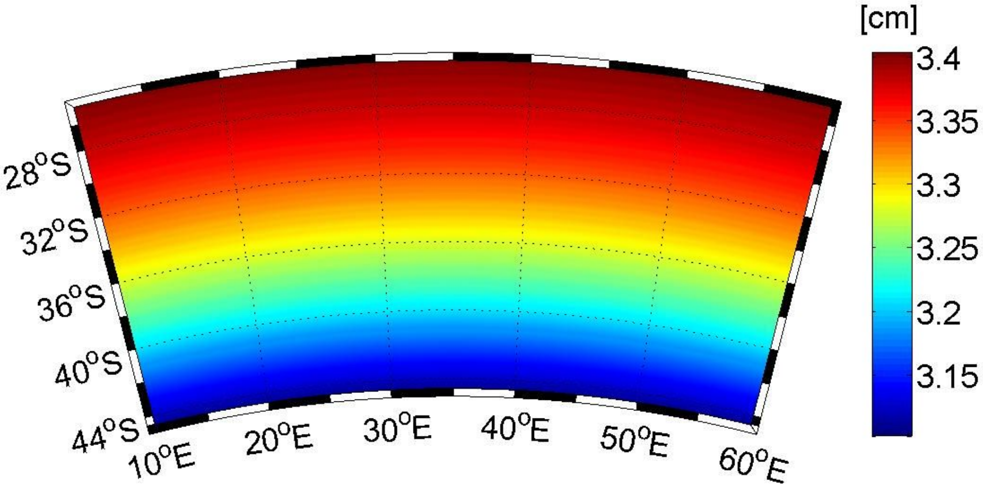

Figure 7.8: Geographical distribution of the propagated geoid errors from the spherical harmonic coefficients up d/o 180 of the gravity model GOCO3S to the geoid heights in the Agulhas current area.

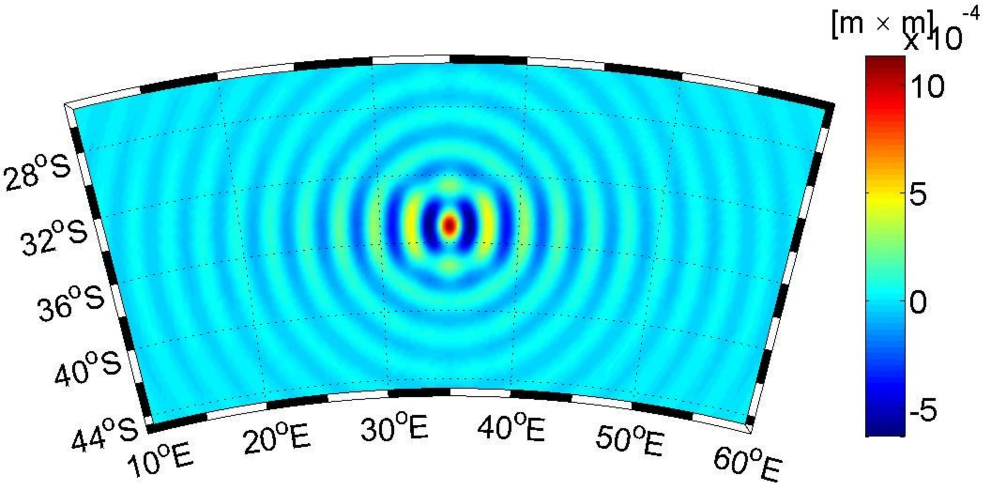

Figure 7.9: Covariance functions evaluated in $\varphi = -35°, \lambda = 35°$ (central point of the Agulhas current area).

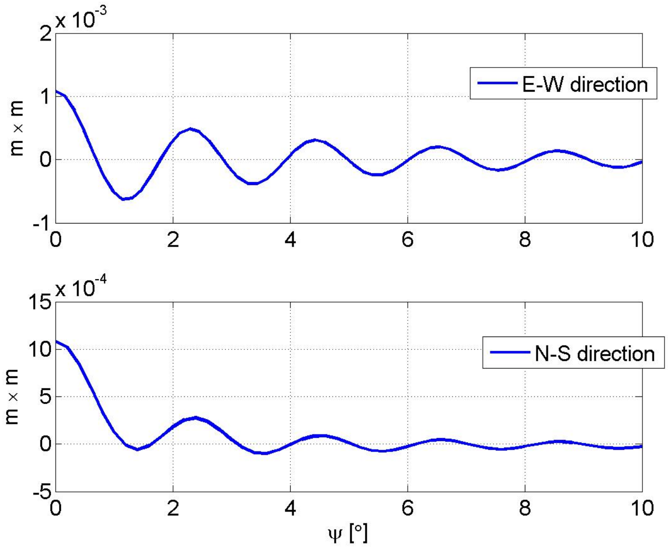

Figure 7.10: Sections of the covariance functions evaluated in $\varphi = -35°, \lambda = 35°$ in the East-West direction (upper panel) and in the North-South direction (lower panel) as function of the spherical distance ψ.

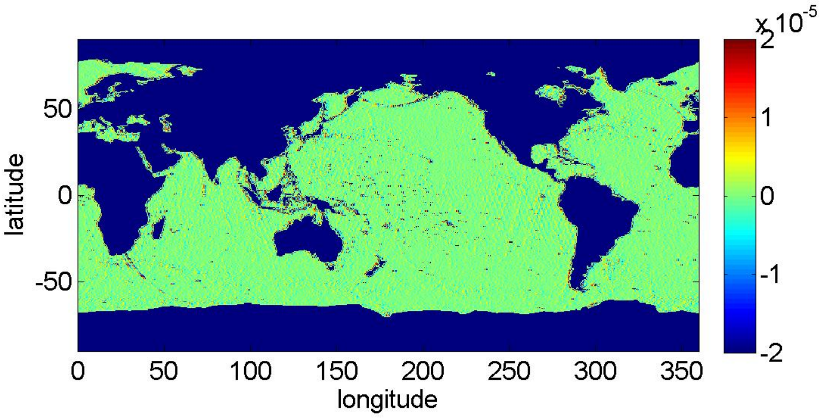

Figure 7.11: Geographical distribution of the north component of the gradient of the errors of the mean sea surface DGFI10 (Fig. 7.1). This is an approximation of the partial derivative of h in north direction.

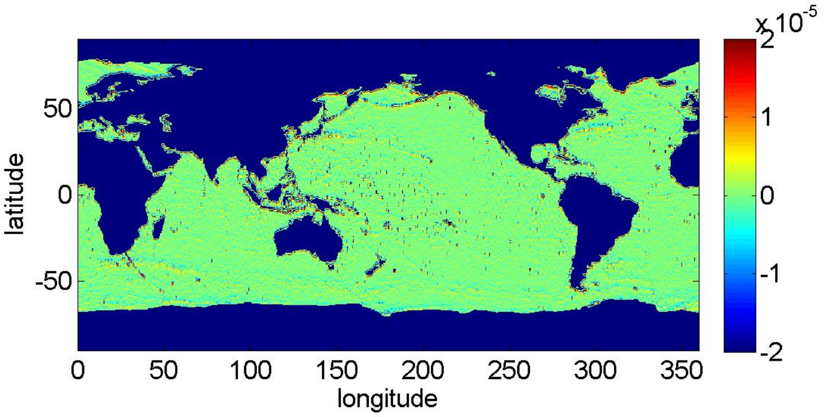

Figure 7.12: Geographical distribution of the east component of the gradient of the errors of the mean sea surface DGFI10 (Fig. 7.1). This is an approximation of the partial derivative of h in east direction.

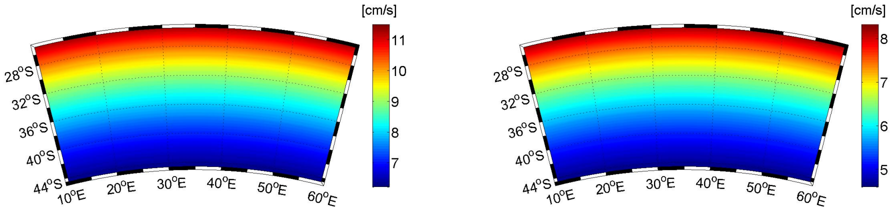

Figure 7.13: Geographical distribution in the Agulhas current area of the propagated geostrophic velocities errors (left panel: North component; right panel: East component). Only the errors of the gravity model GOCO3s are considered. Units are cm/s.

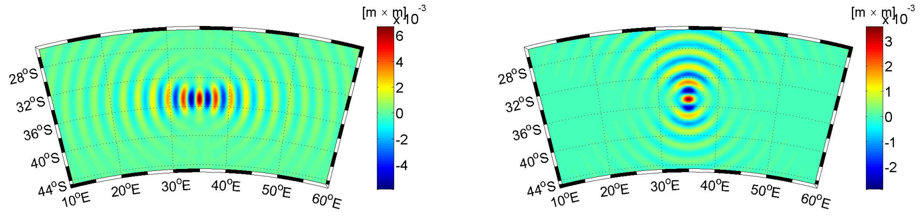

Figure 7.14: Geographical distribution of the covariances of geostrophic velocities errors (left panel: North component; right panel: East component). Only the errors of the gravity model GOCO3s are considered. Units are $m \times m$.

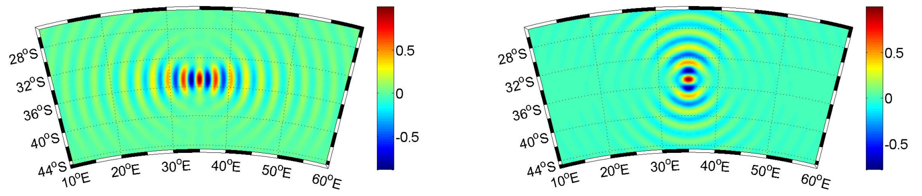

Figure 7.15: Geographical distribution of the correlations of geostrophic velocities errors (left panel: North component; right panel: East component). Only the errors of the gravity model GOCO3s are considered.

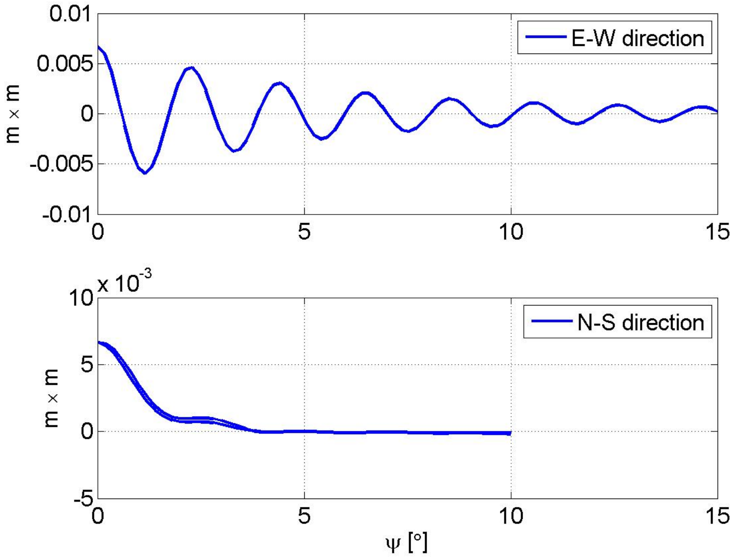

Figure 7.16: Sections of the covariance function of v evaluated in $\varphi = -35°, \lambda = 35°$ in the East-West direction (upper panel) and in the North-South direction (lower panel) as function of the spherical distance ψ. The double line in the plot corresponding to the N-S direction shows the slight an-isotropy of the covariance function in that direction.

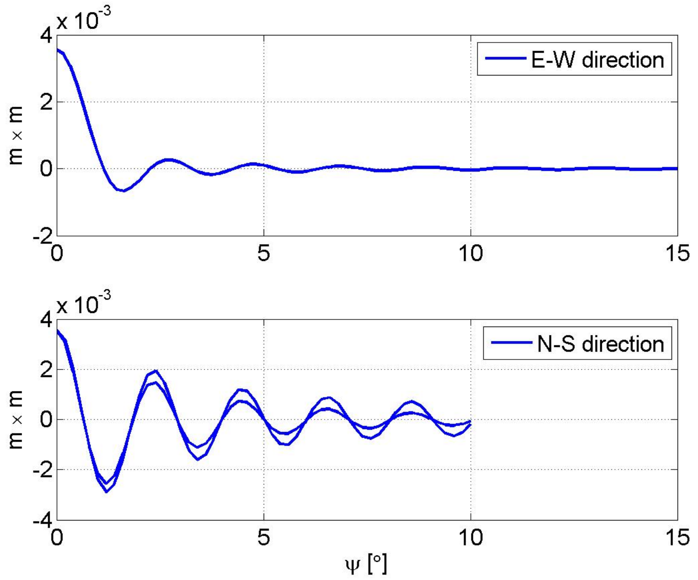

Figure 7.17: Sections of the covariance function of u evaluated in $\varphi = -35°, \lambda = 35°$ in the East-West direction (upper panel) and in the North-South direction (lower panel) as function of the spherical distance ψ. The double line in the plot corresponding to the N-S direction shows the slight an-isotropy of the covariance function in that direction.

Chapter 8

Conclusions

In the present report we presented the computation of a geodetic MDT determined from a high resolution mean sea surface and recent gravity models from the GOCE mission. All the details of the computation are described. The MDT is represented as sum of spherical functions and this allows a bandwidth analysis of the results. The MDT computed using only satellite data, from GOCE and altimetry, is of increased accuracy and resolution compared to GRACE and altimetry solution. The GOCE data are adding short wavelength geoid information, in particular above spherical harmonic degree 120, corresponding to spatial scales below 160 km.
Here, we also described a technique of minimizing adverse effects of extension of MSS over the areas not covered by altimetric measurements. However, coastal zones remain the weak spot of the filtering process when following the spectral approach described here. Unfortunately, these zones are also problematic in terms of MSS calculations and ocean tide modeling.

The proper representation of MDT is needed in order to describe the mean ocean geostrophic surface flow. From the MDT surface, velocities of comparable resolution are derived and analyzed in spectral bands similarly to MDT. In this case the strength of GOCE at shorter scales is more pronounced since the geostrophic velocities are computed from gradients of MDT, amplifying the short scales proportionally to the spherical harmonic degree. The results corresponding to the major oceanic currents (Gulf, Malvinas, Agulhas, Kuroshio and Antarctic Circumpolar Current) are compared with in situ observations from drifters. The agreement of the geostrophic velocities as derived from the geodetic MDT with those based on drifter data is acceptable, but it can be improved. The procedure for isolating the geostrophic part of drifter velocities (including realistic error estimates) can be refined.

The spectral representation of MDT allows us to provide also estimates of uncertainty of the new MDT as well as of the geostrophic velocities. The values of which have strongly decreased from for GRACE only models to GOCE results. The improvement on the shorter scales involves a reduction of 75 per cent of the total error.

Further progress is expected from up-coming gravity models which will utilize all the GOCE measurements and will be combined with GRACE information.

Bibliography

Albertella, A., & Rummel, R. 2009. On the spectral consistency of the altimetric ocean and geoid surface: a one-dimensional example. *Journal of Geodesy*, **83**(9), 805–815.

Albertella, A., Savcenko, R., Janjić, T., Rummel, R., Bosch, W., & Schröter, J. 2012. High resolution dynamic ocean topography in the Southern Ocean from GOCE. *Geophysical Journal International*, **190**(2), 922–930.

Andersen, O. B. 2010. The DTU10 Gravity field and Mean sea surface. Second international symposium of the gravity field of the Earth (IGFS2), Fairbanks, Alaska.

Becker, S., Freiwald, G., Losch, M., & Schuh, W.-D. 2012. Rigorous fusion of gravity field, altimetry and stationary ocean models. *Journal of Geodynamics*, **59Ũ60**(0), 99 – 110.

Bingham, R. J. 2010. Nonlinear anisotropic diffusive filtering applied to the ocean's mean dynamic topography. *Remote Sensing Letters*, **1:4**, 205–212.

Bingham, R. J., Haines, K., & Hughes, C. W. 2008. Calculating the ocean's mean dynamic topography from a mean sea surface and a geoid. *Journal of Atmospheric and Ocean Technology*, **25**, 1808–1822.

Bosch, W., & Savcenko, R. 2010. On estimating the dynamic ocean topography - a profile approach. *Pages 263–269 of:* Mertikas, S.P. (ed), *Gravity, Geoid and Earth Observation.* International Association of Geodesy Symposia, vol. 135. Springer Berlin Heidelberg.

Bosch, W., & Savcenko, R. 2012. *Comparison of mean sea surface DGFI.* Internal Report 89. Deutsches Geodätisches Forschungsinstitut, Munich, Germany.

Bruinsma, S.L., Marty, J.C., Balmino, G., Biancale, R., Förste, C., Abrikosov, O., & Neumayer, H. 2010. GOCE Gravity Field Recovery by Means of the Direct Numerical Method. *Proceedings of the ESA Living Planet Symposium, ESA Publication SP-686, ESA/ESTEC, ISBN (Online).*

Chambers, D. P., A., Hayes S., C., Ries J., & J., Urban T. 2003. New TOPEX sea state bias models and their effect on global mean sea level. *Journal Geophysical Research*, **108(C10)**, 3305.

Dettmering, D., & Bosch, W. 2010a. Envisat radar altimeter calibration by multi-mission crossover analysis. *Proceedings of the ESA Living Planet Symposium, Bergen, Norway*, **ESA Publication SP-686**.

Dettmering, D., & Bosch, W. 2010b. Global Calibration of Jason-2 by Multi-Mission Crossover Analysis. *Marine Geodesy*, **33**(sup1), 150–161. `http://www.tandfonline.com/doi/abs/10.1080/01490419.2010.487779`.

DEVARAJU, B., & SNEEUW, N. 2012. Performance Analysis of Isotropic Spherical Harmonic Spectral Windows. *Pages 105–110 of:* SNEEUW, NICO, NOVÁK, PAVEL, CRESPI, MATTIA, & SANSÓ, FERNANDO (eds), *VII Hotine-Marussi Symposium on Mathematical Geodesy*. International Association of Geodesy Symposia, vol. 137. Springer Berlin Heidelberg.

ELEMA, I. A. 1993. *Influence of geoid model uncertainty on the determination of the ocean circulation with satellite altimetry.* Diploma thesis, Technische Universiteit Delft, faculteit der geodesie.

EUROPEAN SPACE AGENCY. 1999. *Gravity Field and Steady-State Ocean Circulation Mission. Report for mission selection of the four candidate Earth Explorer missions.* Tech. rept. European Space Agency, SP-1233(1), Noordwijk.

FECHER, T. 2008 (10). *Methodische Grundlagen von kombinierten Schwerefeldmodellen.* IAPG/FESG-Schriftenreihe 26. Institut für Astronomische und Physikalische Geodäsie, Forschungseinrichtung Satellitengeodäsie.

GERLACH, CH., & FECHER, TH. 2013. Approximations of the GOCE error variance-covariance matrix for least-squares estimation of height datum offsets. *Journal of Geodetic Science*, **2**(4), 247–256.

GOIGINGER, H., RIESER, D., MAYER-GÜRR, T., PAIL, R., FECHER, T., GRUBER, T., ALBERTELLA, A., BROCKMANN, J.M., SCHUH, W.D., KUSCHE, J., *et al.* 2011. The combined satellite-only global gravity field model GOCO02S. *EGU General Assembly*, **13**.

GRODSKY, S. A., LUMPKIN, R., & CARTON, J. A. 2011. Spurious trends in global surface drifter currents. *Geophysical Research Letters*, **38**(L10606).

HEISKANEN, W. A., & MORITZ, H. 1967. *Physical Geodesy.* Freeman, San Francisco.

HERNANDEZ, F., & SCHAEFFER, P. 2000. *Altimetric Mean Sea Surfaces and Gravity Anomaly maps inter-comparisons.* Tech. rept. CLS, AVI-NT-011-5242-CLS.

HORVATH, A., & PAIL, R. 2012a. Error budget analysis of a mean dynamic topography. Proceedings of the 20 years of Progress in Radar Altimetry Symposium, ESA Publication SP-710, ESA/ESTEC.

HORVATH, A., & PAIL, R. 2012b. Mean dynamic topography - Error contributions from the gravity field and the mean sea surface. International Symposium on Gravity, Geoid and Height Systems GGHS 2012, Venice, Italy.

HUGHES, C. W., & BINGHAM, J. R. 2008. An Oceanographer's Guide to GOCE and the Geoid. *Ocean Science Discussions*, **4**, 15–29.

IIJIMA, B. A., HARRIS, I. L., HO, C. M., LINDQWISTER, U. J., MANNUCCI, A. J., PI, X., REYES, J., SPARKS, L. C., & WILSON, B. D. 1999. Automated daily process for global ionospheric total electron content maps and satellite ocean ionospheric calibration based on Global Positioning System. *Journal of Atmospheric and Solar-Terrestrial Physics*, **61**, 1205–1218.

JANJIĆ, T., ALBERTELLA, A., SCHROETER, J., SAVCENKO, R., RUMMEL, R., & BOSCH, W. 2012. Assimilation of geodetic dynamic ocean topography with an ensemble based Kalman filter. *EGU General Assembly*, **Vienna, April 22 Ũ-27**.

Jekeli, C. 1981. *Alternative methods to smooth the earth's gravity field.* Tech. rept. 327. Department of Civil and Environmental Engineering and Geodetic Science, Ohio State University, Columbus, Ohio.

Losch, M., & Seufer, V. 2003. *How to Compute Geoid Undulations (Geoid Height Relative to a Given Reference Ellipsoid) from Spherical Harmonic Coefficients for Satellite Altimetry Applications.* http://mitgcm.org/ mlosch/geoidcookbook/geoidcookbook.html.

Losch, M., Sloyan, B.M., Schröter, J., & Sneeuw, N. 2002. Box inverse models, altimetry and the geoid: Problems with the omission error. *Journal of Geophysical Research - Oceans*, **107**(C7), 15–1 – 15–13.

Lumpkin, R., & Garraffo, Z. 2005. Evaluating the Decomposition of Tropical Atlantic Drifter Observations. *Journal of Atmospheric and Oceanic Technology*, **I 22**(3078), 1403–1415.

Maximenko, N., Niiler, P., Rio, M.-H., Melnichenko, O., Centurioni, L., Chambers, D., Zlotnicki, V., & Galperin, B. 2009. Mean dynamic topography of the ocean derived from satellite and drifting buoy data using three different techniques journal. *Journal of Atmospheric and Oceanic Technology*, **29**(9), 1910Ũ–1919.

Mayer-Gürr, T., Eicker, A., Kurtenbach, E., & Ilk, K.Heinz. 2010a. ITG-GRACE: Global Static and Temporal Gravity Field Models from GRACE Data. *Pages 159–168 of:* Flechtner, Frank M., Gruber, Thomas, Güntner, Andreas, Mandea, M., Rothacher, Markus, Schöne, Tilo, Wickert, Jens, Stroink, L., Mosbrugger, V., & Wefer, G. (eds), *System Earth via Geodetic-Geophysical Space Techniques.* Advanced Technologies in Earth Sciences. Springer Berlin Heidelberg.

Mayer-Gürr, T., Eicker, A., & Kurtenbach, E. 2010b. *ITG-Grace2010 Gravity Field Model.* Tech. rept. Institut für Geodäsie und Geoinformation, Univ. Bonn.

Mayer-Gürr, T., Savcenko, R., Bosch, W., Daras, I., Flechtner, F., & Dahle, Ch. 2011. Ocean tides from satellite altimetry and GRACE. *Journal of Geodynamics.*

Mayer-Gürr, T., Rieser, D., Höck, E., Brockmann, J.M., Schuh, W.-D., Krasbutter, I., Kusche, J., Maier, A., Krauss, S., Hausleitner, W., Baur, O., Jäggi, A., Meyer, U., Prange, L., Pail, R., Fecher, T., & Gruber, T. 2012. The new combined satellite only model GOCO03s. *GGHS*, **Venice, October 2012**.

Monahan, David. 2008. Mapping the floor of the entire world ocean: the General Bathymetric Chart of the Oceans. *Journal of Ocean Technology*, **3**, 108.

Orsi, A. H., Whitworth III, T., & Nowlin Jr., W. D. 1995. On the meridional extent and fronts of the Antarctic Circumpolar Current. *Deep-Sea Research*, **42**, 641–673.

Pail, R., & Fecher, T. 2011. *Covariance analysis of global gravity field model and propagation to geostrophic velocities for the Drake Passage.* Internal Report. Institute of Astronomical and Physical Geodesy, Technische Universität München, Germany.

Pail, R., Goiginger, H., Schuh, W.-D., Höck, E., Brockmann, J. M., Fecher, T., Gruber, T., Mayer-Gürr, T., Kusche, J., Jäggi, A., & Rieser, D. 2010. Combined satellite gravity field model GOCO01S derived from GOCE and GRACE. *Geophysical Research Letters*, **37**(10).

Pail, R., Bruinsma, S., Migliaccio, F., Förste, C., Goiginger, H., Schuh, W.-D., Höck, E., Reguzzoni, M., Brockmann, J. M., Abrikosov, O., Veicherts, M., Fecher, T., Mayrhofer, R., Krasbutter, I., Sansó, F., & Tscherning, C. C. 2011. First GOCE gravity field models derived by three different approaches. *Journal of Geodesy*, **85**(11), 819–843. Special issue: "GOCE - The Gravity and Steady-state Ocean Circulation Explorer".

Pail, R., Albertella, A., Fecher, T., Horvath, A., & Savcenko, R. 2012. Rigorous covariance propagation of geoid errors to geodetic MDT estimates. European Geosciences Union General Assembly 2012, Wien.

Pavlis, N.K., Holmes, S. A., Kenyon, S. C., & Factor, J. K. 2012. The development and evaluation of the Earth Gravitational Model 2008 (EGM2008). *Journal Geophysical Research*, **117**(B4), B04406.

Pond, S., & Pickard, G. L. 1983. *Introductory Dynamic Oceanography.* Pergamon Press.

Ralph, E. A., & Niiler, P. P. 1999. Wind-driven currents in the Tropical Pacific. *Journal of Physical Oceanography*, **29**, 2121–2129.

Rio, M.-H., & Hernandez, F. 2003. High-frequency response of wind-driven currents measured by drifting buoys and altimetry over the world ocean. *Journal of Geophysical Research*, **108, C8**(3823), 1–19.

Rio, M.-H., Schaeffer, P., Hernandez, F., & Lemoine, J.-M. 2006. From the altimetric sea level measurement to the ocean absolute dynamic topography: Mean Sea Surface, Geoid, Mean Dynamic Topography, a three-component challenge. *Proceedings of the "15 Years of Progress in Radar Altimetry" Symposium, ESA Special Publication SP-614.*

Rummel, R., & Gruber, T. 2010. Gravity and Steady-State Ocean Circulation Explorer GOCE. *Pages 203–212 of:* Flechtner, Frank M., Gruber, Thomas, Güntner, Andreas, Mandea, M., Rothacher, Markus, Schöne, Tilo, Wickert, Jens, Stroink, L., Mosbrugger, V., & Wefer, G. (eds), *System Earth via Geodetic-Geophysical Space Techniques.* Advanced Technologies in Earth Sciences. Springer Berlin Heidelberg.

Rummel, R., Yi, W., & Stummer, C. 2011. GOCE gravitational gradiometry. *Journal of Geodesy*, **85**, 777–790. 10.1007/s00190-011-0500-0.

Scharroo, R., & Smith, W. H. F. 2010. A global positioning system-based climatology for the total electron content in the ionosphere. *Journal of Geophysical Research*, **115**(A10318).

Scharroo, R., & Visser, P. 1998. Precise orbit determination and gravity field improvement for the ERS satellites. *Journal of Geophysical Research*, **103**(C4), 8113–8127.

Schrama, E., Scharroo, R., & Naeije, M. 2000. *Radar Altimeter Database System (RADS): Towards a generic multi-satellite altimeter database system.* Tech. rept. USP-2 report 00-11. BCRS/SRON, Delft, TheNetherlands.

Siegismund, F. 2013. Assessment of optimally filtered recent geodetic mean dynamic topographies. *J. Geophys. Res. Oceans*, **118**, 108–117.

Stummer, C., Siemes, C., Pail, R., Frommknecht, B., & Floberghagen, R. 2012. Upgrade of the GOCE Level 1b gradiometer processor. *Advances in Space Research*, **49**(4), 739–752.

Wade, Graham. 1994. *Signal Coding and Processing.* Cambridge University Press.

WAHR, J., M., MOLENAAR, & F., BRYAN. 1998. Time variability of the Earth's gravity field: Hydrological and oceanic effects and their possible detection using GRACE. *Journal of Geophysical Research*, **103**, 30205 30229.

YI, W. 2012. An alternative computation of a gravity field model from GOCE. *Advances in Space Research.* http://dx.doi.org/10.1016/j.asr.2012.04.018.

ZENNER, L. 2006. *Zeitliche Schwerefeldvariationen aus GRACE und Hydrologiemodellen.* Diploma thesis, Institut für Astronomische und Physikalische Geodäsie, Forschungseinrichtung Satellitengeodäsie.

Reports in the *CGE Reports* series (ISSN 2195-7126)
Veröffentlichungen in der Schriftenreihe „CGE Reports“ (ISSN 2195-7126)

No. 1: Pail R., Hugentobler U., Rummel R., Seitz F., Bosch W., Angermann D., Steigenberger P., Gruber T., Bouman J., Schmidt M., Völksen C., Neidhardt A., Schreiber U., Horwath M. (2012): Research and Development Programme 2011–2015, Forschungs- und Entwicklungsprogramm 2011–2015, ISBN 978-3-934205-32-1.

No. 2: Yi, Weijong (2012): The Earth's gravity field from GOCE, ISBN 978-3-934205-34-5.

No. 3: Schlie, J. (2012): Die GETRIS Mission – Konzeptstudie einer zukünftigen Schwerefeldmission zur Beobachtung von Massentransportprozessen im System Erde, ISBN 978-3-934205-33-8.

No. 4: Ettl, M. (2013): Hochgenaue numerische Lösung von Bewegungsproblemen mit frei wählbarer Stellengenauigkeit, ISBN 978-3-934205-35-2.

No. 5: Schneider, M. (2014): Zur Lösung der Navier-Stokes-Gleichungen, ISBN 978-3-934205-36-9.

No. 6: Albertella, A., Rummel, R. (2014): GOCE geoid, mean dynamic ocean topography and geostropic velocities, ISBN 978-3-934205-37-6

ISSN 2195-7126
ISBN 978-3-934205-37-6